*Graduate School Form*
*30 Updated 12/26/2015*

**PURDUE UNIVERSITY**
**GRADUATE SCHOOL**
**Thesis/Dissertation Acceptance**

This is to certify that the thesis/dissertation prepared

By Dan Shen

Entitled

Hybrid Wind-Solar-Storage Energy Harvesting Systems

For the degree of Master of Science in Electrical and Computer Engineering

Is approved by the final examining committee:

Maher Rizkalla
Co-chair

Afshin Izadian
Co-chair

Lingxi Li

To the best of my knowledge and as understood by the student in the Thesis/Dissertation Agreement, Publication Delay, and Certification Disclaimer (Graduate School Form 32), this thesis/dissertation adheres to the provisions of Purdue University's "Policy of Integrity in Research" and the use of copyright material.

Approved by Major Professor(s): Maher Rizkalla, Afshin Izadian

Approved by: Brian King 4/11/2016

Head of the Departmental Graduate Program Date

# HYBRID WIND-SOLAR-STORAGE ENERGY HARVESTING SYSTEMS

A Thesis

Submitted to the Faculty

of

Purdue University

by

Dan Shen

In Partial Fulfillment of the

Requirements for the Degree

of

Master of Science in Electrical and Computer Engineering

May 2016

Purdue University

Indianapolis, Indiana

First and foremost, I would like to give wholehearted thanks to my parents for their understanding and selfless dedication. Thank you both for giving me great support and encouragement mentally and materially during my hard work. Without your concern and guidance, I cannot accomplish studies.

I would like to thank to my wife Cynthia, my life partner and friend, for being my source of motivation and comfort. We shared the joys and sorrows, and will move forward together forever.

Also thank to my friends, without your help and understanding, I cannot have such wonderful experience in the foreign land.

# ACKNOWLEDGMENTS

The research work of this thesis is finished by following the guidance and assistance of Dr. Afshin Izadian. During my study for master's degree, Dr. Izadian generously shared with me his research experience and directed me towards perfection in every details. I greatly thank Dr. Izadian for his profound theoretical knowledge and noble ethics, for which I will keep in my heart forever and make me lifelong benefit.

I would like to thank Dr. Maher Rizkalla, for his constant support throughout my course work and Dr. Linxi Li, for taking time out of his busy schedule to be a part of my supervisor committee. Thank them both for writing the recommendation letters for me during the PhD applications.

I would like to thank to the Departments of Electrical & Computer Engineering and Engineering & Technology for allowing the collaboration between the two departments for study and research. I would like to thank Ms. Sherrie Tucker for assistance throughout the Graduate's program.

TABLE OF CONTENTS

Page

Page

# LIST OF TABLES

# LIST OF FIGURES

Figure Page

Figure Page

Figure Page

Figure Page

Figure Page

# ABSTRACT

Shen, Dan. M.S.E.C.E., Purdue University, May 2016. Hybrid Wind-Solar-Storage Energy Harvesting Systems. Major Professors: Maher Rizkalla and Afshin Izadian.

With the increasing demand of economy and environmental pollutions, more and more renewable energy systems with clean sources appear and have attracted attention of systems involving solar power, wind power and hybrid new energy powers[1]. However, there are some difficulties associated with combined utilization of solar and wind, such as their intermittent behavior and their peak hours mismatch in generation and consumption[1]. For this purpose, advanced network of a variety of renewable energy systems along with controllable load and storage units have been introduced[1]-[3].

This thesis proposes some configurations of hybrid energy harvesting systems, including wind-wind-storage DC power system with BOOST converters, solar-solar-storage DC power system with cascade BOOST converters, wind-solar-storage DC power system with BOOST converter and cascade BOOST converter, and wind-solar DC power system with SEPIC converter and BOOST converter. The models of all kinds of systems are built in Matlab/Simulink and the mathematical state-space models of combined renewable energy systems are also established. Several MPPT control strategies are introduced and designed to maximize the simultaneous power capturing from wind and solar, such as Perturb & Observe (P&O) algorithm for solar and wind, Tip Speed Ratio (TSR) control and Power Signal Feedback (PSF) control for wind, and Sliding Mode Extremum Seeking Control (SMESC) for wind and solar

systems[4]. The control effects of some of these MPPT methods are also compared and analyzed. The supervisory control strategies corresponding to each configurations are also discussed and implemented to maximize the simultaneous energy harvesting from both renewable sources and balance the energy between the sources, battery and the load[2]. Different contingencies are considered and categorized according to the power generation available at each renewable source and the state of charge in the battery[2].

Applying the system architectures and control methods in the proposed hybrid new energy systems is a novel and significant attempt, which can be more general in the practical applications. Simulation results demonstrate accurate operation of the supervisory controller and functionality of the maximum power point tracking algorithm in each operating condition both for solar and for wind power[3].

# 1. INTRODUCTION

## 1.1 Problem Statement

Because of increasing demand of economy, the world energy consumption is increasing year by year with depletion of fossil fuel resources. There also has been concerns on accompanying global climate change and its related harmful effects, such as environmental pollution, global warming and extreme climate. These severe impacts endanger not only the balance of the ecosystem but also the stability of human society. In order to mitigate these challenges, renewable energy is developing rapidly. This blend includes wind, solar, hydro-power, bio-energy, geothermal and nuclear energy. Both developing and developed countries have put forward and implemented some successful policies to promote and encourage the smart grids with utilization of renewable energy generation. Among them, the United States and several major countries in the European Union (EU) have announced significant changes regarding their short-and long-term energy-generation targets and investments. China, Brazil, Canada, and India have also increased the investments in their alternative energy technologies [5]. Based on the research of Bloomberg New Energy Finance, Figure 1.1 shows the worldwide power generation capacity additions (GW), which indicates the world is now adding more capacity for renewable energy every year than fossil fuels, such as coal, natural gas, and oil since 2013.This shift will continue to accelerate, and by 2030 more than four times as much renewable capacity will be added. The key feature of the figure is the rapid expansion of renewables in developing countries. Developed countries had a slight increase of 3%, to $138.9 billion, but investments in developing economies noted an increase of 36%, to $131.3 billion. Therefore, growing concerns over increase in greenhouse gas emissions, global environmental deteriora-

tions and sustainable development, has increasingly shifted interest of energy experts towards integration of renewable energy sources in the power systems.

Compared with other renewables, wind and solar have been established as proven future sources of energy, because of their environment-friendly, safe, wide range of the world and cost-effective characteristics[1]. Nevertheless, the great dependence on sun radiation level of solar energy and wind speed of wind energy, such uncertain natural environments may cause the instability of the single power system. Harnessing these two energies for electric power generation is the area of aiming at quality and reliability in the electricity delivery [6], [7], [8]. Nowadays, the most attractive way, with present technology, is to propose the advanced network of multiple renewable energies with storage units to ensure a reliable supply of power[1]. Thus the simultaneous intermittency of wind and solar can be compensated by their energy complementary on the time and geographical distribution and the use of energy storage devices[3].

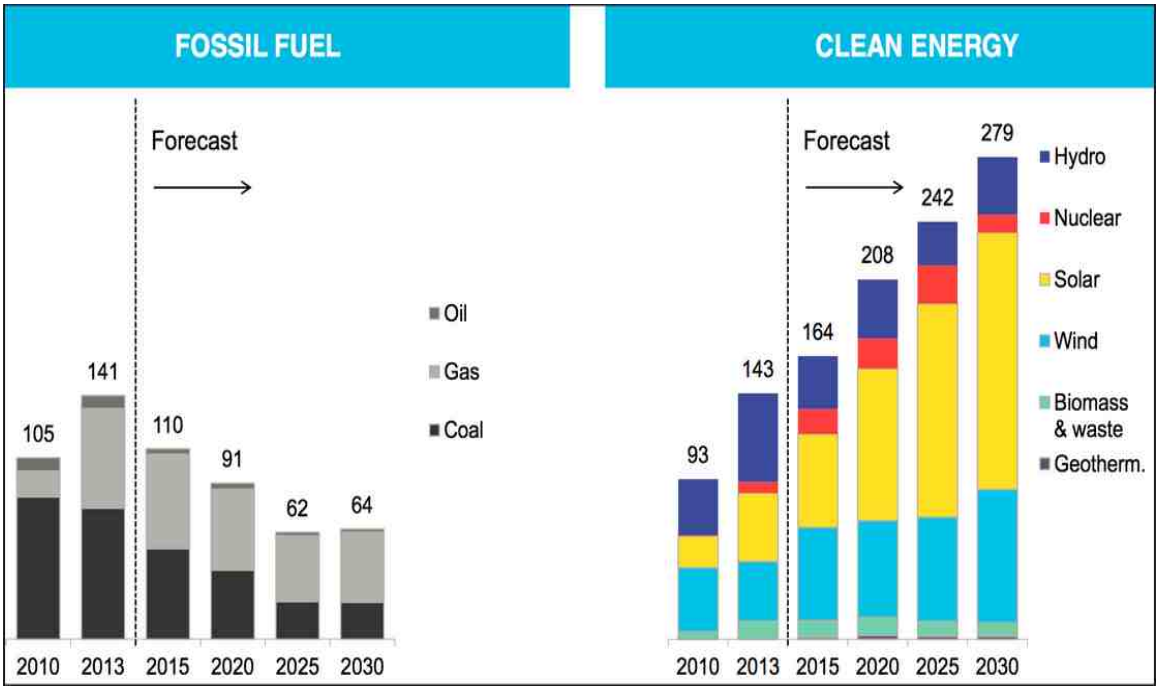


Fig. 1.1. Worldwide power generation capacity additions (GW)

In addition, the optimization of system configuration is the other extremely important solution. Because there are still some difficulties associated with combined utilization of solar, wind[1], loads and storage elements, e.g. intermittency and low energy density of wind or solar, [9] and mismatch between power generation and load demands[1]. The optimization of system configuration for the hybrid wind-solar-storage power system can be viewed as a multi-objective optimization issue, where the two main issues are maximizing power supply efficiency and minimizing the cost of power supply. For this purpose, more attentions should be paid on the maximum power point tracking (MPPT) control methods and the supervisory control strategies of the combined new energy system. For MPPT method, high initial investment makes it necessary for the customers to capture the maximum power generated from the renewables. According to the nonlinear characteristics of both wind and PV array, the output power of solar depends greatly on the solar radiations and temperature, and the output of wind turbine relies on the wind speed, pitch angle and some other parameters. Under one certain weather condition, the two renewables can operate at different voltage or current levels, but there is only one particular condition that can assure the energy system delivers the maximum power, which means the maximum power point (MPP). Therefore, the algorithms of finding and extracting the MPP is called MPPT, which design to maximize the power output efficiency and MPPT speed. Supervisory control strategies determine the source type according to the availability and rating of the power[2] and the state of charge (SOC) of battery. As the DC bus voltage floats within a range, the battery can be charged or discharged. A designated voltage source (either wind or solar) will be controlled to charge the battery at the desired rate. When both sources are controlled to inject current, the bus voltage is determined by the battery terminals. Thus, the strategy of the supervisory controller is to satisfy the power required by the load and manage the battry's state of charge [3].

## 1.2 Background and Previous Work

Small-scale combination of solar-wind-storage has been found effective in some independent power supply systems at remote areas[1]. To begin with, several designs have used a power converter interface in the battery connection to control the charge-discharge process of the battery. However, a battery can be directly connected to the DC bus and be controlled by limited variation of DC bus voltage. The power converters interfacing the wind and solar can inject the power as a current source or voltage source[3].

Moreover, many combined energy power systems by using various power electronic converters or control strategies have been put forward[1]. Among them, reference [10] presents a neural network based control system to coordinate between the components of a PV-Wind hybrid system[1]. Reference [11] proposed a power control mechanism that can manage a combined photovoltaic (PV)/wind/fuel cell (FC) generation system including an ultra-capacitor bank[1]. Reference [12] introduced a novel strategy for the control of power conditioning units to minimize the disturbance on the output power from the hybrid system which integrated with PV and wind turbine[1]. Reference [13] introduced a holistic modeling method of a combined PV and wind power system[1]. The goal of the work was to accomplish an optimized digital control followed by the rapid prototyping into a single Field Programmable Gate Array (FPGA) with BUCK and BOOST converter[1]. Reference [14] presents a new three-input DC-DC BOOST converter which is interesting for hybridizing alternative energy sources including PV source, fuel cell and battery. The control structure utilizes only four power switches that can accomplish tracking of the maximum power of PV and FC power, controlling the battery power and refining the output voltage with four different duty cycles. Reference [15] recommended a novel adaptive strategy for power flow in standalone hybrid power system contains PV, battery and proton exchange membrane fuel cell. The method included a neural network controller in the first layer, a fuzzy logic controller in the second layer and local controllers which are

used to regulate the set points in the third layer[1]. Reference [16] proposed a new active/reactive power closed-loop control system for a hybrid sustainable energy system used for a single-phase commercial applications[1]. However, all of the mentioned methods which used conventional approaches or some advanced control techniques for controlling the combined generation system have proven to be unstable and have shown low reliability to some extents during the fast and nonlinear changes in weather conditions[1]. Hence, simultaneous maximum power extraction from wind and solar and supervisory controllers have become the challenging research topics in the hybrid power systems[1].

In addition, accordingly, photovoltaic (PV) arrays, wind turbines and batteries are used to feed a DC or AC bus connected to the load and battery, as well as the utility grid, constituting the so-called microgrid [17], [18]. Microgrids operate in both standalone and grid connected modes, which also categorized as DC microgrid and AC microgrid. Depicted in Figure 1.2 [16] is the hybrid renewable energy generation system with both AC microgrid and DC microgrid. Recent advances in DC distribution systems have shown several advantages with respect to AC systems[2]. First, DC system provides higher power quality with low harmonic content [19], [20]. Second, the switch mode power converters and their current limiting features can provide an excellent uninterrupted power handling [21], and various sources of power can be combined into a standalone microgrid [22], [23]. Overall end-to-end energy conversion efficiency in a DC microgrid can reach 77%-85% whereas a less than 60% in AC counterparts. Most of this efficiency improvement is because of the elimination of AC loads and their associated power inverters [24]. In the previous designs, many systems have employed a DC/DC power converter to interface the battery to enable the charge–discharge process. While, a battery can be directly connected to the DC bus and be regulated by limited variation of DC bus voltage[3]. Therefore, both the wind power and solar power can operate as a voltage source to inject power to the load and battery. The presented hybrid power system in this thesis is a DC microgrid with a battery and load directly connected to the DC bus.

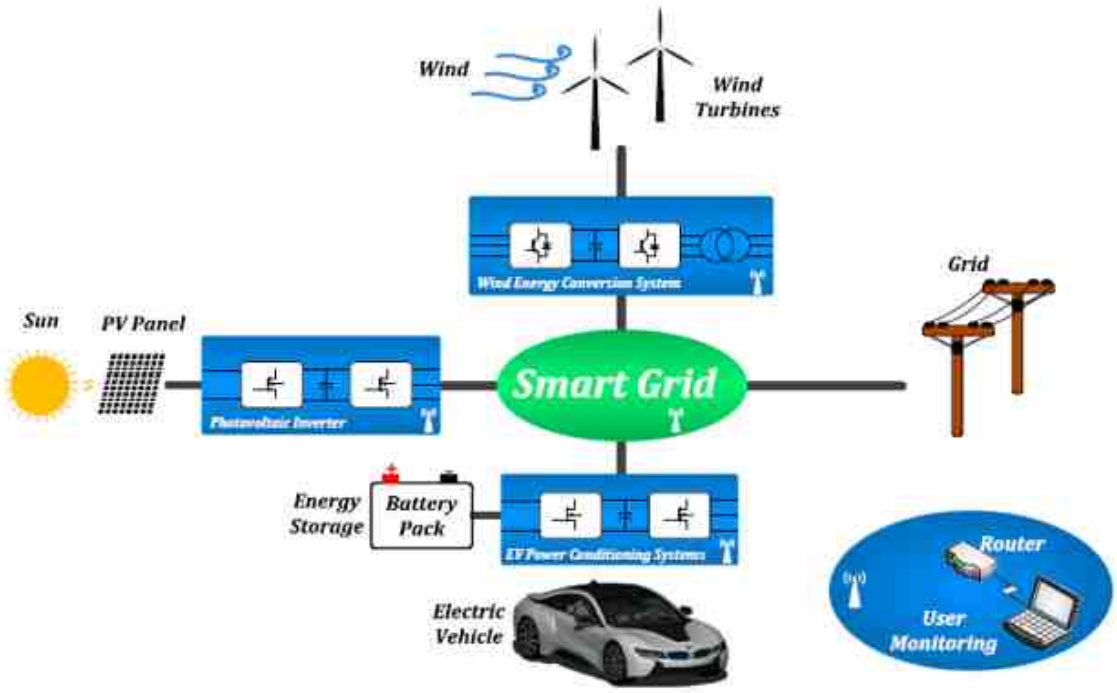


Fig. 1.2. Hybrid renewable energy generation system with both AC microgrid and DC microgrid.

## 1.3 Main Contributions

This thesis introduces the control for hybrid wind-solar-storage energy harvesting systems. Four different configurations of the combined new energy systems are proposed. Traditional and novel MPPT strategies are also analyzed and compared under the changing of DC constant power load and the SOC of battery.

Compared with the previous work related to the hybrid renewable systems. There are mainly two contributions in the thesis. The first one is the configurations of the proposed systems. Four hybrid wind-solar systems with different structures and MPPT methods are established and analyzed, which is more productive and meaningful than the other articles with respect to the configurations aspect. The other one is the sliding mode extremum seeking control (SM-ESC) MPPT technique for both wind power system and solar power system[4].

For wind MPPT, generally, there are three traditional types of the wind MPPT techniques: 1) power signal feedback (PSF) control, 2) tip speed ratio (TSR) control, and 3) perturb and observe (P&O) control[1],[4]. The control of these MPPT methods depends on the maximum power characteristics curve resulting from simulation or field tests[1],[4], requirement of wind information and perturbation of rotor speed respectively, which are limited by the complexity of the sensors and the big oscillations [4],[25]-[29]. Relay Extremum Seeking Control (ESC) has been one commonly MPPT algorithm for both solar and wind systems in recent years. But relay ESC force the wind system to track the maximum power point by increasing or decreasing one suitable control signal depends on the sign of the gradient of output power vs. rotor speed, which can amplify the noise and lead to the instability issues at high frequency[4]. In order to eliminate the gradient sensors in relay ESC method, sliding mode theory in extremum seeking control has been introduced from the references [4],[30]-[32]. Although the similar techniques have been used in both solar MPPT and wind MPPT, there are two main differences between the developed methods and proposed strategy: 1) the controlled objective is not DC-DC converter but AC-DC inverter [4],[32]-[33]. 2) The load-side in the proposed wind system is not just a resistor [4],[34]-[35] but the dynamic load which includes battery and the DC constant power load. For solar MPPT, there are some widely applied MPPT methods, such as perturb and observe (P&O) methods [36-37], incremental conductance (INC) methods [38], ripple correlation control (RCC) methods [39] and open or short circuit methods [40]. The shortages of these methods are the convergence speed and the oscillation magnitude, complicated computation and low accuracy. Furthermore, installation of one converter per solar panel may have difficulties for achieving the desired DC bus voltage level of DC microgrid when the climate changes[2]. Thus, SM-ESC apply with cascade BOOST converters will be available to realize the maximum power point and output voltage control at the same time. Therefore, applying the SM-ESC in the proposed wind system will be a novel and significant attempt, which can be more general in the practical applications[4].

## 1.4 About This Thesis

This thesis can be organized as follows: Chapter 2 is the introduction and operation of the hybrid wind-solar-storage DC power system. In this section, wind DC micro-gird with BOOST converters and SM-ESC MPPT method, solar DC micro-grid with cascade BOOST converters and SM-ESC MPPT control method, hybrid wind-solar-storage DC microgrid with BOOST converter for wind, cascade BOOST converter for solar and SM-ESC MPPT method and hybrid wind-solar DC microgrid without battery but with BOOST converter and P&O method are discussed regarding the configurations and operations. Chapter 3 introduces the modeling of the proposed combined DC power system, including the wind turbine, PV panel, DC-DC converter, DC constant power load, battery and the state-space model of all the four DC microgrids. Chapter 4 is the control methods for the energy system. The TSR, PSF, P&O and SM-ESC MPPT methods are introduced and designed for wind system. The P&O and SM-ESC MPPT methods are also analyzed and designed for solar system. In the last of this section, the supervisory control strategies are also established base on the configurations of the hybrid new energy systems. Chapter 5 is the simulation results of the proposed systems and control methods, such as different MPPT techniques, comparisons of traditional MPPT methods and the presented MPPT methods, and the supervisory control effects of the entire DC microgrid with the variations of weather conditions and the changing of DC constant power load.

# 2. HYBRID DC POWER SYSTEM

## 2.1 Introduction and Hybrid Power System Operation

The Chapter 2 introduces and analyzes the hybrid wind-solar-storage DC power system from perspective of system configurations and descriptions. Recently, hybrid wind-solar-storage systems have become attractive solution due to their complementary blend of power and their reliability. Combining both wind and solar can also let the hybrid system run economically since the shortage of one system can be compensated by the advantage of the other system or the storage units. By integrating the two renewables into an optimum assembly, hybrid wind-solar energy systems can be separated into two types: grid connected and stand-alone. Many researchers have shown numerous configurations and proposed various possible control and optimization methods on both stand-alone and grid-connected systems [41]. For the purpose of this thesis, the stand-alone hybrid DC systems will be the main research objective.

Regarding the combination of solar and wind energy system into the grid is available to reduce the total cost and enhance the efficiency of power delivery. Because the grid can absorb the generated energy from wind and solar sources and take the surplus power to satisfy the load requirements[1]. Figure 2.1 and Figure 2.2 illustrate the common DC bus and common AC bus grid-connected hybrid system with solar and wind respectively [41]. As can be seen in the two figures, there are mainly two topologies for the grid-connected hybrid system.

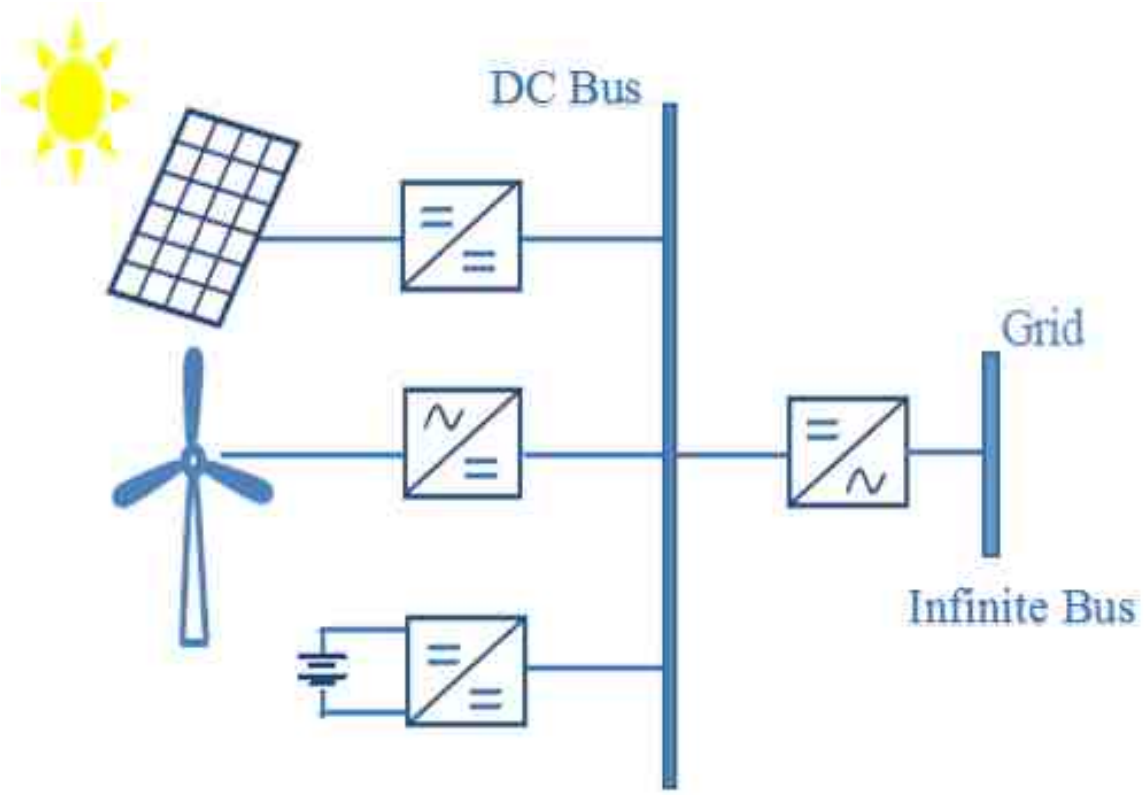


Fig. 2.1. Grid-connected hybrid system with DC bus.

Figure 2.1 indicates that two DC/DC converters and one AC/DC converter are used to connect to DC bus from solar panel, wind turbine and battery, and then the common DC bus integrates to the grid with an individual DC/AC inverter, which works as an interface between the power supply and the grid to deliver the standard power with any combinations of three sources by regulating the DC bus voltage. On the other hand, Figure. 2.2 demonstrates that the two renewables and energy storage unit can inject power to the grid directly through individual DC/AC inverter from solar panel, AC/DC-DC/AC inverter from wind turbine and DC/AC inverter from storage device [41].

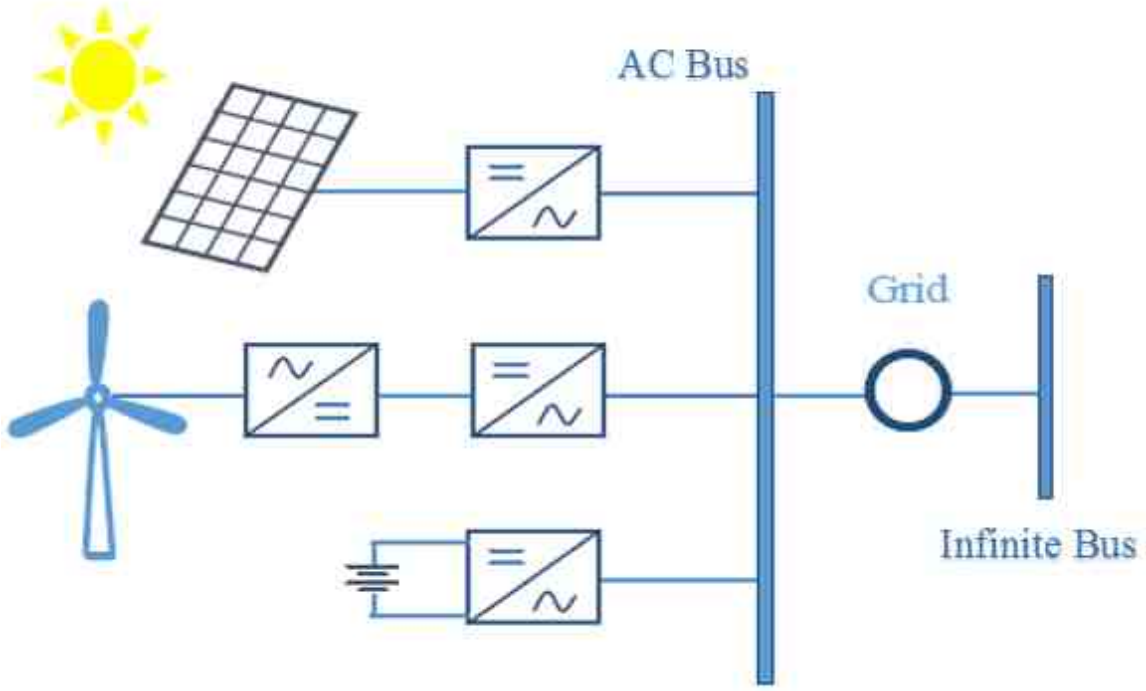


Fig. 2.2. Grid-connected hybrid system with AC bus.

The stand-alone or called autonomous energy systems are more beneficial for remote areas and residential buildings. Because without the grid and AC loads, the systems can be more convenient to install or integrate some DC loads. In addition, this DC system can generate a higher quality power with lower harmonics[2], because the output power can be completely uninterrupted by controlling switched-mode power converters [2],[20],[41], allowing the final aggregation of standalone energy sources to the main DC grid [2], [23]. The same as grid-connected hybrid systems, stand-alone combined systems also have two main topologies: common DC bus and common AC bus. Figure 2.3 shows the stand-alone hybrid system with common DC bus. The three sources of solar panel, wind turbine and battery are connected in parallel with DC/DC converter, AC/DC converter and DC/DC converter respectively. The DC bus voltage from all sources is set to be regulated by charging or discharging the battery and the output currents generated from each power supply are regulated independently based on the load demands.

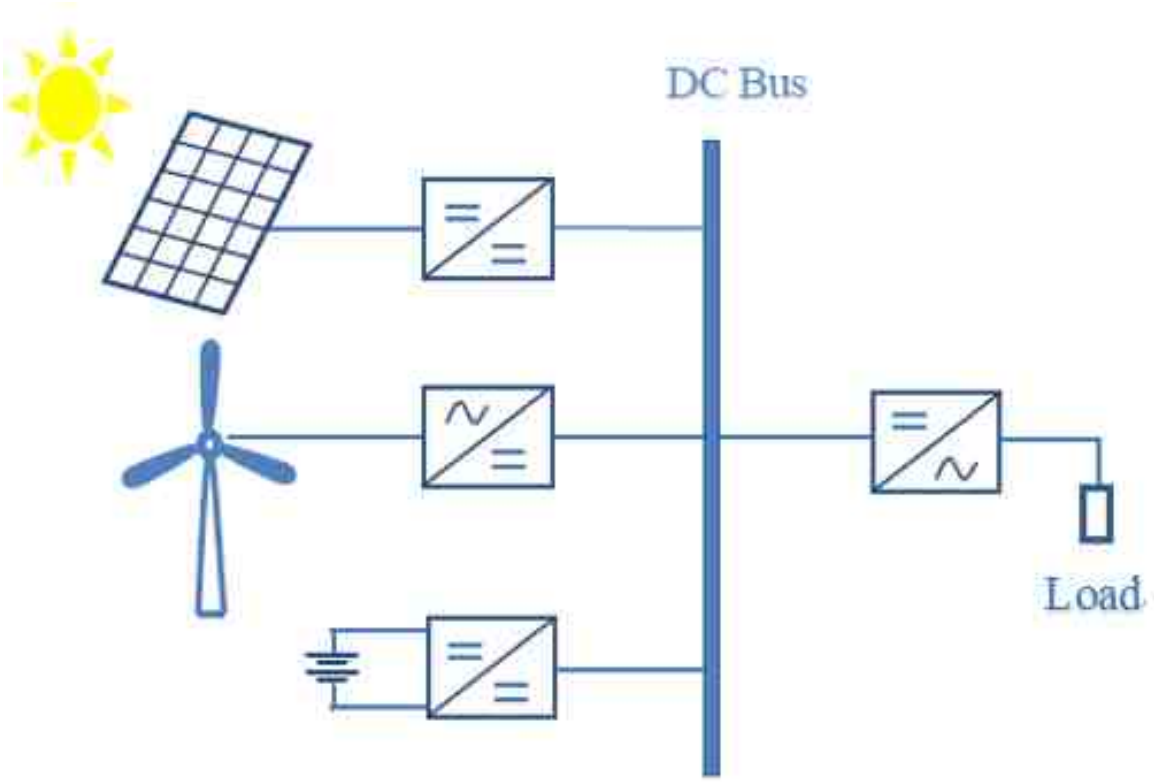


Fig. 2.3. Stand-alone hybrid system with DC bus.

The DC/AC inverter operates as an interface between the energy sources and the AC loads by controlling the AC output voltage. Figure 2.4 depicts the stand-alone hybrid energy system with common AC bus. The output AC voltages from solar panel, wind turbine and battery are controlled through two individual DC/AC inverters and AC/DC-DC/AC inverter, and then are feeding the AC loads directly. Two renewables can behave as current sources and the battery acts as a voltage source to manage the AC bus voltage by injecting or extracting the current. Droop control are also usually utilized to generators for voltage or frequency control with load sharing of multiple generators. Compared with these two types of stand-alone hybrid systems, the one with common DC bus has main strength for coupling varying power sources operating at constant frequency. The one with common AC bus is also widely applied because of its low cost, easy extension and simple installation [2],[41]. Figure 2.5 also shows a hybrid wind-solar-storage system integrated to an AC microgrid,

which can operate at both grid-connected mode and stand-alone mode. However, proposed in this thesis is the hybrid wind-solar-storage system integrated to a DC microgrid, which always work in a stand-alone mode with variations of DC constant power load (CPL).

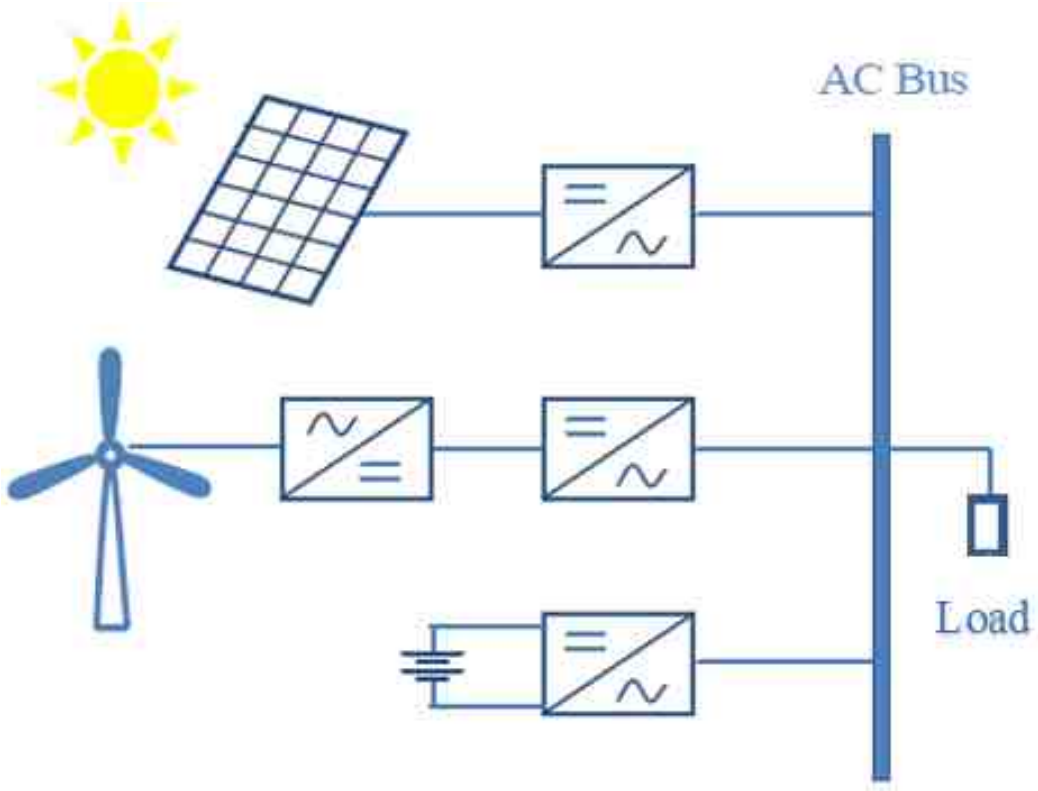


Fig. 2.4. Stand-alone hybrid system with AC bus.

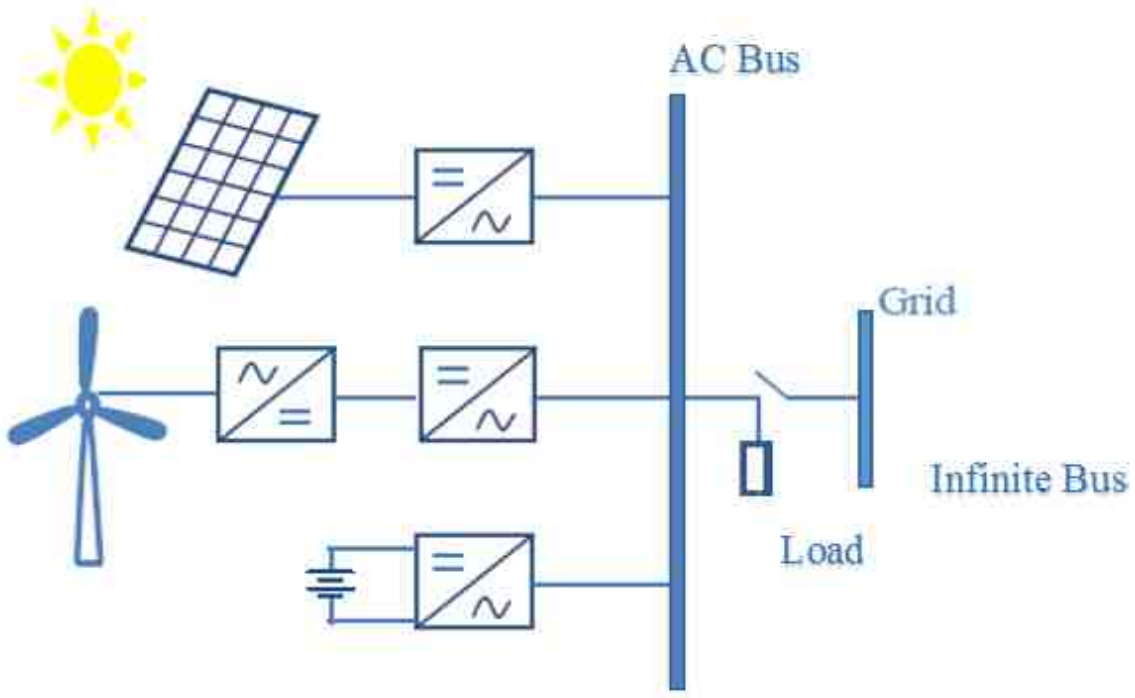


Fig. 2.5. Hybrid system with AC microgrid.

## 2.2 Main Configurations of Hybrid Power System

This section will describes the four configurations of the hybrid power system and the operations of each components with different circuits, combination of renewable sources and control methods. The main components of the system are solar panel, wind turbine, permanent magnet synchronous machine (PMSG), AC/DC rectifier, DC/DC converter, battery, DC constant power load, MPPT controllers and supervisory controllers. The specific diagrams of the four topologies are also introduced.

### 2.2.1 Wind-Wind-Storage DC Power System

The first configuration of the hybrid system is wind-wind-storage DC power system, which can also be called wind DC microgrid[4]. As depicted in Figure 2.6, the wind distributed energy generation system has two branches with the parallel connec-

tion of two wind turbines to the common DC bus, and each branch consists of wind turbine, uncontrolled universal bridge, Permanent Magnet Synchronous Generator (PMSG), DC/DC BOOST converter interfaces a battery and a DC constant power load which composes a DC motor and a local proportion and integration (PI) power controller[4]. Thus the AC power is converted to DC power and delivered to the BOOST converter, which can be regulated by MPPT controllers based on the sliding mode and extremum seeking control theory[2],[4]. The controller receives the mechanical output power from the wind turbine and operates a maximum-power-point tracking (MPPT) algorithm to send and adjust the pulse width modulation (PWM) signal for the booster circuit regarding the level of power coefficient $C_p$ [1],[2],[4]. The supervisory controller decides the next control mode according to the wind turbine output power, DC load power demand and the state of charge of battery[4].

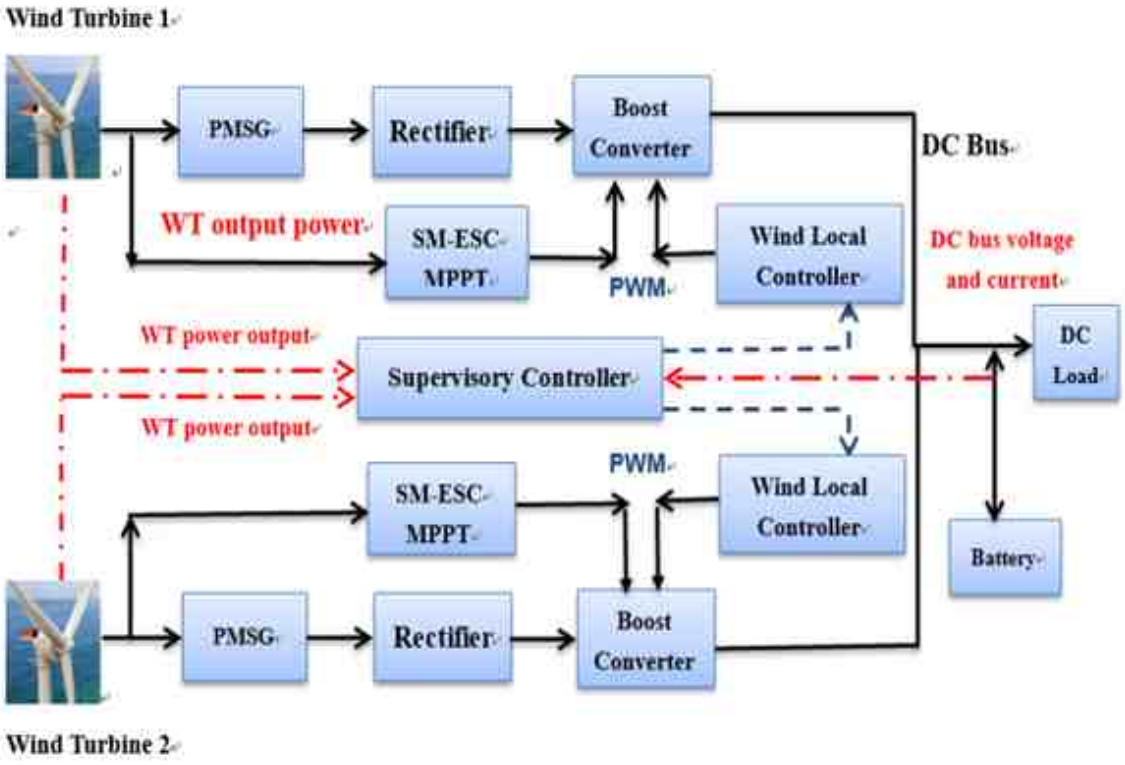


Fig. 2.6. Proposed wind DC microgrid.

### 2.2.2 Solar-Solar-Storage DC Power System

The second topology of the hybrid system is solar-solar-storage DC power system, which can also be named as solar DC microgrid[2]. Figure 2.7 demonstrates the proposed configuration of the combined power sources consisting of two solar panels, battery with cascaded BOOST DC/DC converters interfaces a DC constant power load[2]. The two first stage converters are controlled by MPPT controllers based on sliding mode control and extremum seeking control (SM-SMC) theories. Each of them receives the PV voltage and current from solar and runs a MPPT algorithm to adjust the sliding surface with the conductance $g_1$[2]. The second-stage sliding mode control of BOOST

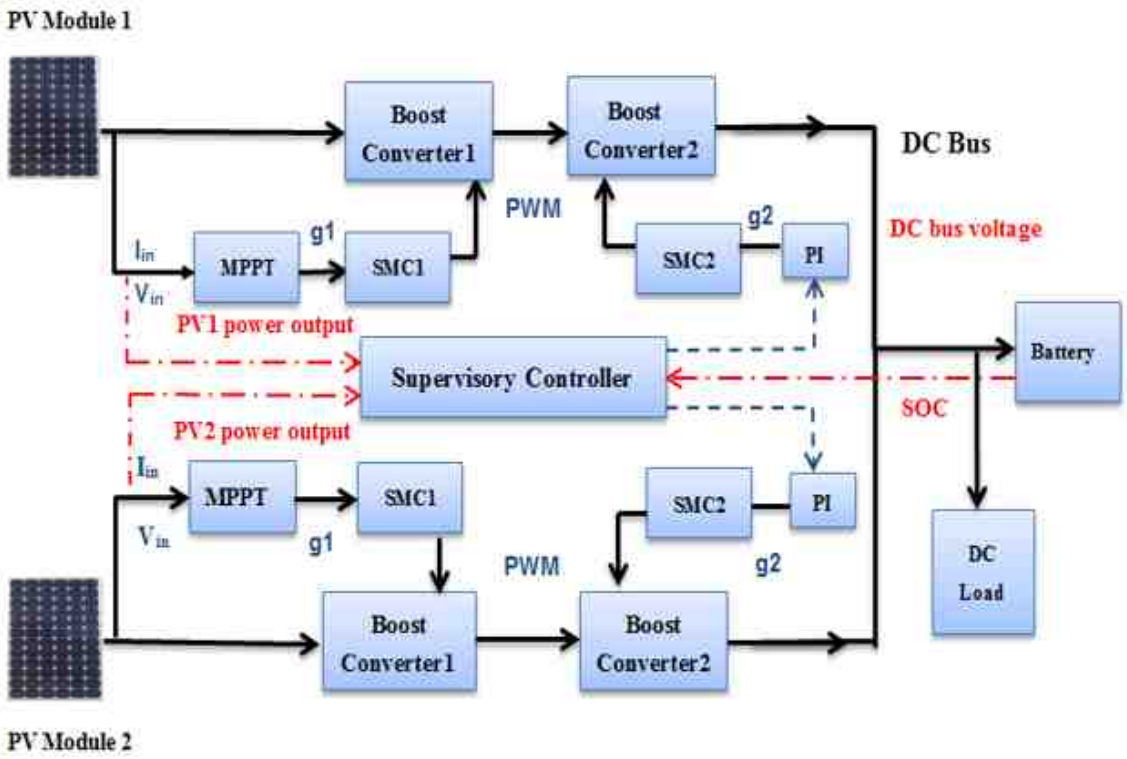


Fig. 2.7. Proposed solar DC microgrid.

converter will be regulated by a local PI controller to operate as a constant voltage sources (CVS) with a constant value $g_2$[2]. The supervisory controller receives signals

of the state of charge from battery and output power from each PV systems, and determines the next appropriate control mode under different scenarios[2]. The two energy sources are connected in parallel to a common DC bus through their individual DC/DC converters [2],[42].

### 2.2.3 Wind-Solar-Storage DC Power System

The third configuration of the hybrid system is solar-solar-storage DC power system, which can also be nominated as wind-solar-storage DC microgrid. Figure 2.8 illustrates the proposed topology of a combined power generation unit consisting of solar, wind and battery with DC/DC power converters to connect a constant power DC machine as CPL[3]. It can be observed that there are two main branches in the system[3], thus solar and wind power can compensate each other to a certain degree. The wind power branch includes a wind turbine, a permanent magnet synchronous

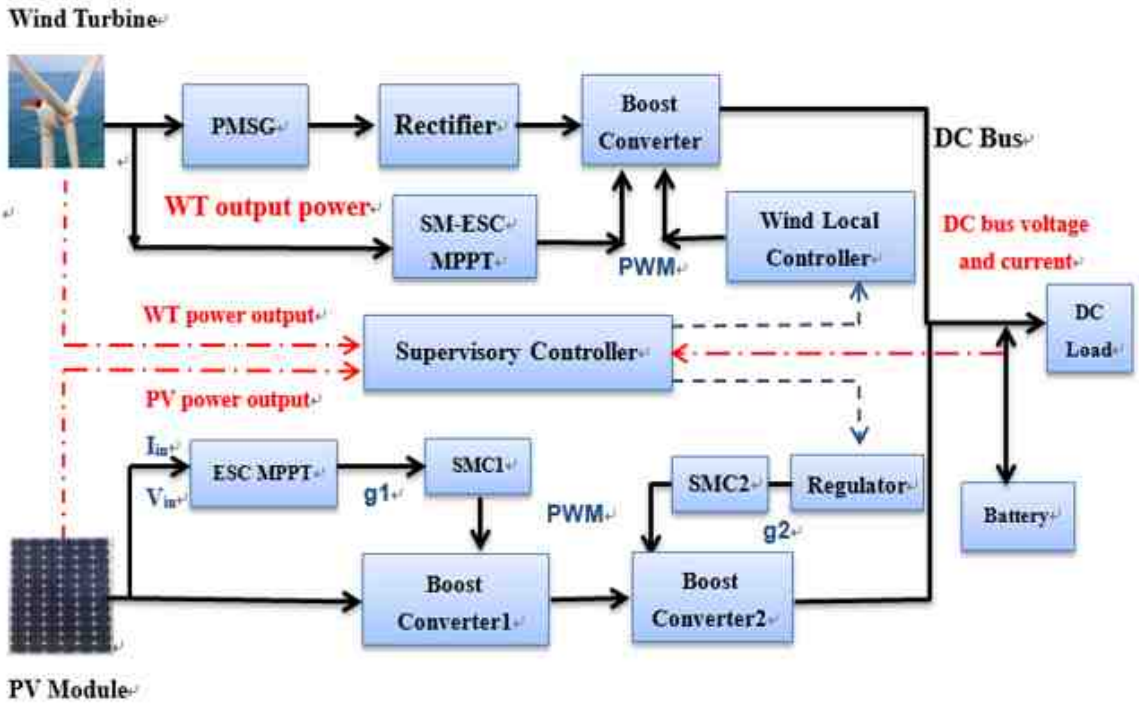


Fig. 2.8. Proposed wind-solar-storage DC microgrid.

generator (PMSG), an uncontrolled universal bridge, a BOOST converter, wind SM-ESC MPPT controller, and a wind local controller which can close the wind system when the wind speed is too high[4]. The PV power branch is composed by the cascaded BOOST converters[1], one MPPT controller based on extremum seeking controller and the sliding mode controller one at the first stage, and a local regulator whose input is solar irradiance based on another sliding mode controller at the second stage. Each source runs a maximum power point tracking (MPPT) algorithm and optimizes the efficiency of power transfer[4].

### 2.2.4 Wind-Solar DC Power System

Considering that some applications use the DC load without battery. The fourth configuration of the hybrid system is wind-solar DC power system, which can also be viewed as wind-solar DC microgrid. The two main differences between the fourth one and the previous three topologies are the existence of battery and the supervisory control strategy. Presented in Figure 2.9, the combined power system contains the wind power, the PV panel and the resistive load[1]. There are two main branches in the system, thus two new energy sources can compensate each other to some extent under climate changes[3]. The wind power system branch contains wind turbine, permanent magnet synchronous machine (PMSM), a universal bridge, single ended primary inductor converter (SEPIC) converter, wind MPPT controller and a local PI current controller[1]. The PV power system branch is composed by PV panel, BOOST converter, solar MPPT controller and the local PI current controller[1]. The P&O MPPT algorithm is used in both PV system and wind system. Each source has its individual PI current controller and a supervisory controller to coordinate and supervise the power flows among different power sources[1]. When the power generation system can satisfy the load with surplus energy, one source can be selected to operate in MPPT mode and the other source is set in power tracking mode by means of a PI current controller [1],[43].

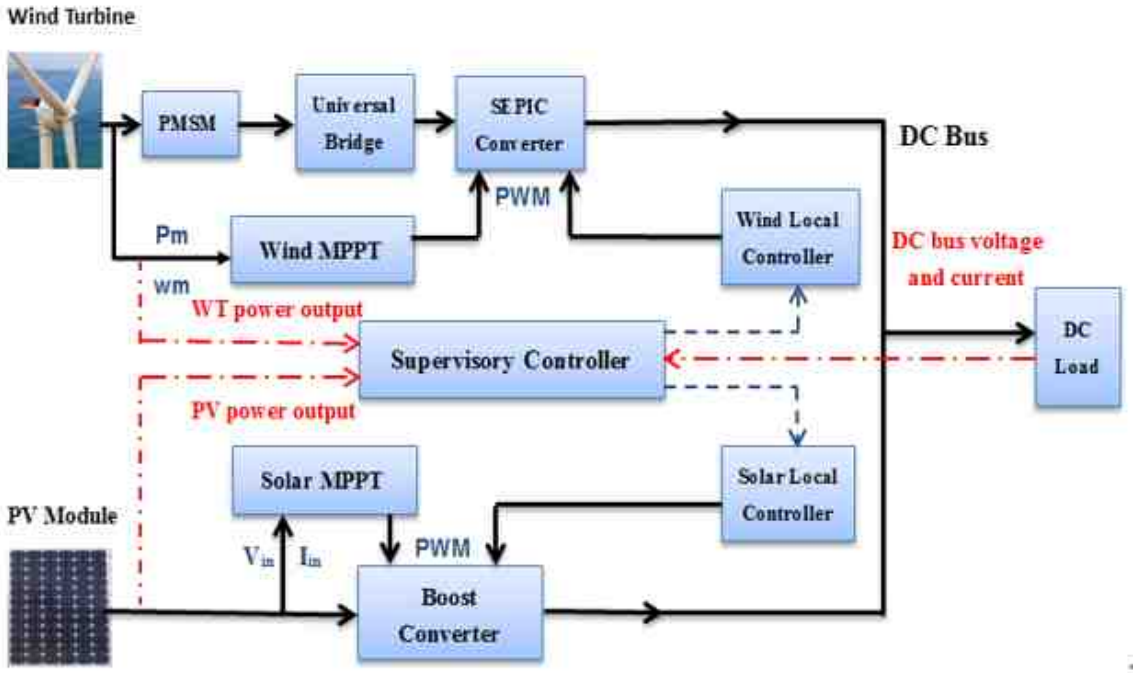


Fig. 2.9. Proposed wind-solar DC microgrid.

# 3. HYBRID DC POWER SYSTEM MODELING

Chapter 3 introduces every components of the hybrid wind-solar-storage DC power system expect for the controllers, such as wind power system, solar power system, constant power load, DC/DC converter, battery and the state-space models of the above four configurations of the combined new energy systems in the Chapter 2. All the models are built in Matlab/Simulink.

## 3.1 Introduction

As part of the combined energy generation system, wind energy system is a device that can convert wind energy into electric energy[1]. A typical wind generation system is composed of wind turbine and generator, the wind turbine converts wind energy into mechanical energy and then the generator converts the mechanical energy into electric energy[1]. Figure. 3.1 illuminates the energy conversion chart of wind generation system[1]. $P_w$ is the wind turbine input power; $C_p$ is wind power utilization coefficient, the theoretical maximum value of $C_p$ is 0.593 based on the Betz Theory[1]. $\omega_m$ is rotor speed of the wind turbine, $\eta_m$ is the transmission efficiency which is over 95%, $\omega_t$ is rotor speed of generator, $\eta_g$ is the efficiency of generator which is over 80%, $P_m$ is the wind turbine mechanical output power, $P_t$ is transmission power, $P_e$ is output power of wind generator[1].


Fig. 3.1. Energy Conversion Chart of wind generation system.

### 3.2 Modeling of Wind Power System

The fundamental equation of the relationship between wind turbine output power and wind speed is given by[1]:

$$P = \frac{1}{2}\rho A V^3 C_p \tag{3.1}$$

Where $\rho$ is air density ($kg/m^3$), $\rho$ is $1.025kg/m^3$ in this paper[1],[4]. $A$ is the area swept by rotor blades, $V$ is velocity of air ($m/sec$), $C_p$ is power coefficient of the wind turbine[1]. The ratio of tip speed $\lambda$ and $C_p$ can be expressed as follows[1],[4]:

$$\lambda = \frac{\omega R}{V} = \frac{2\pi R n}{V} \tag{3.2}$$

$$C_p(\lambda, \beta) = c_1(\frac{c_2}{\lambda_i} - c_3\beta - c_4)e^{-\frac{c_5}{\lambda_i}} + c_6\lambda \tag{3.3}$$

$$\frac{1}{\lambda_i} = \frac{1}{\lambda + 0.08\beta} - \frac{0.035}{\beta^3 + 1} \tag{3.4}$$

In the above formula, $\omega$ is the rotor speed of wind turbine ($rad/s$), $n$ is the rotational speed of wind turbine ($r/s$), $R$ is the radius of wind turbine ($R$=2.5m in this thesis), from the help information in Matlab [3-4],[44-48], $C_1$=0.5176,$C_2$=116, $C_3$=0.4,$C_4$=5,$C_5$=21,$C_6$=0.0068. The simulink model of wind turbine is shown in Figure 3.2.

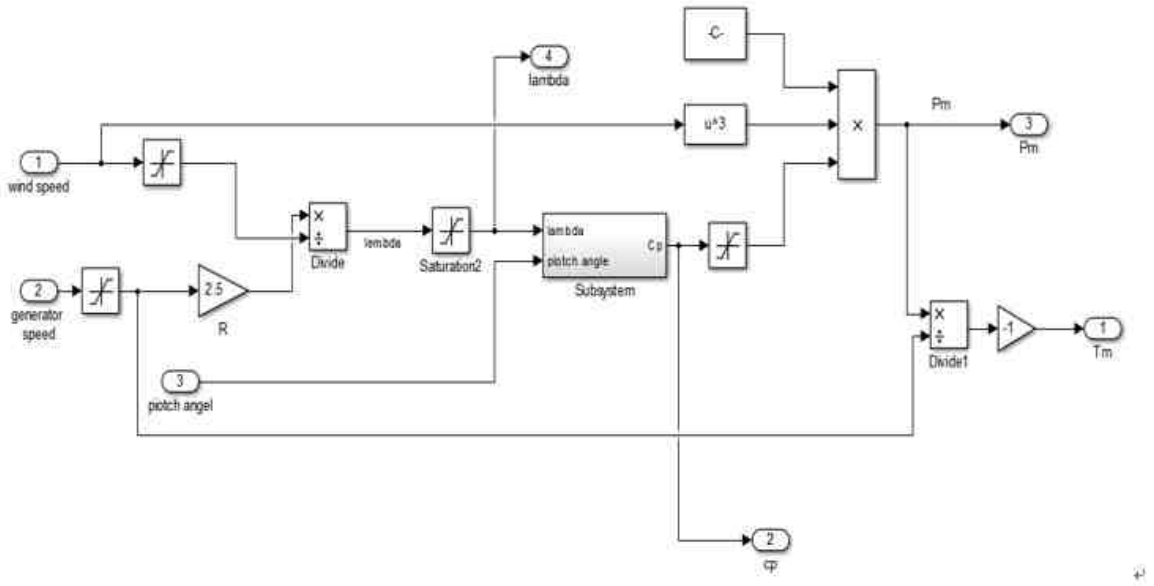


Fig. 3.2. Simulink model of wind turbine.

Figure 3.3 illustrates the wind energy utilization coefficient $C_p$ under different pitch angle. From the figure, it can be clearly found that $C_p$ reaches the maximum value 0.48 when pitch angle is 0 degree, and $C_p$ value decreasing with the increasing of pitch angle.

The proposed wind power system in this thesis consists of a fixed pitch angle and variable speed wind turbine, a permanent magnet synchronous generator (PMSG) and a diode bridge rectifier[1]. The wind turbine and PMSG connect directly without gearbox so the wind turbine torque and rotor speed are equal to the generator torque and rotor speed[1]. Figure. 3.4 and Figure. 3.5 show the characteristics of the wind turbine output power and torque vs. rotor speed when wind speed is 4m/s, 6m/s, 8m/s, 10m/s and 12m/s[1].

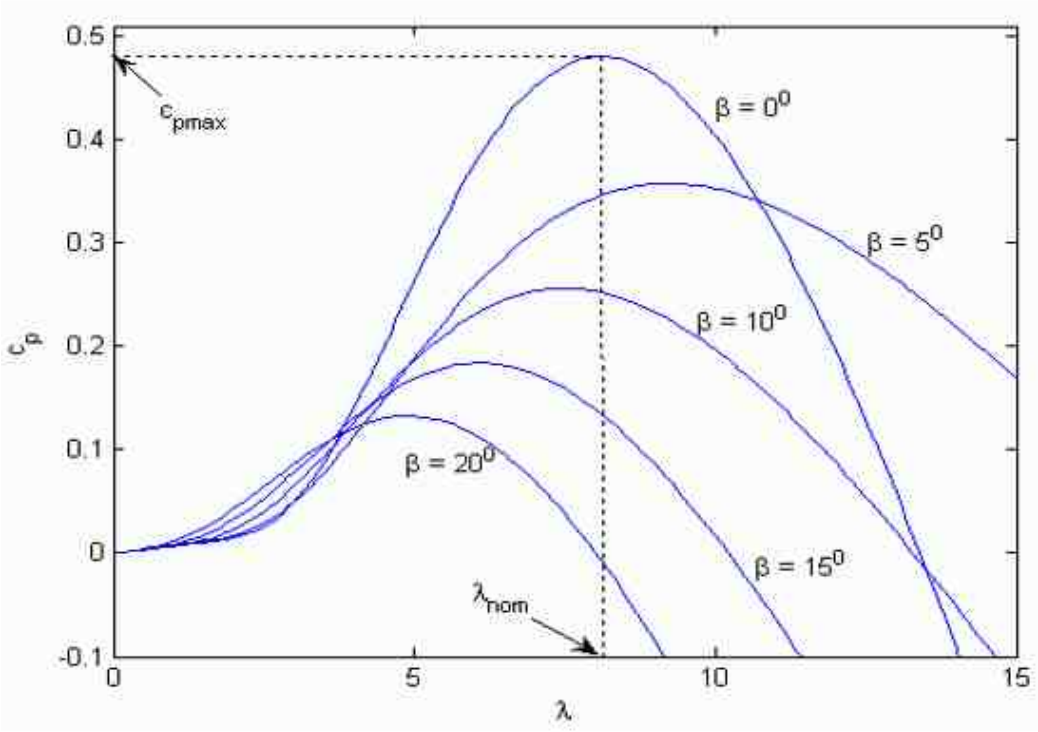


Fig. 3.3. $C_p$ value under different pitch angle.

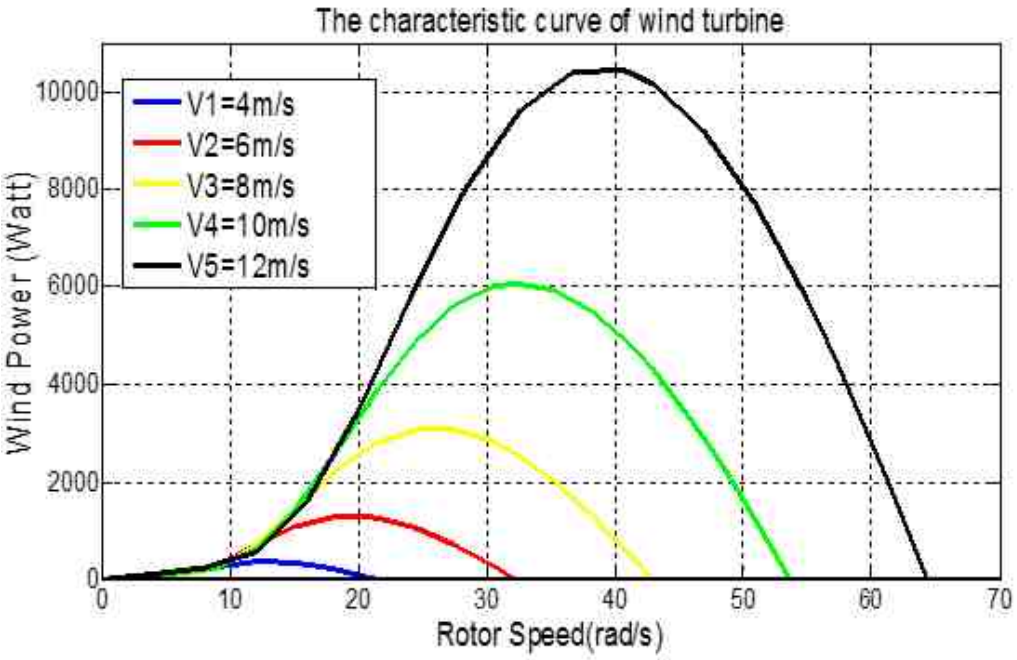


Fig. 3.4. Wind turbine output power vs. rotor speed.

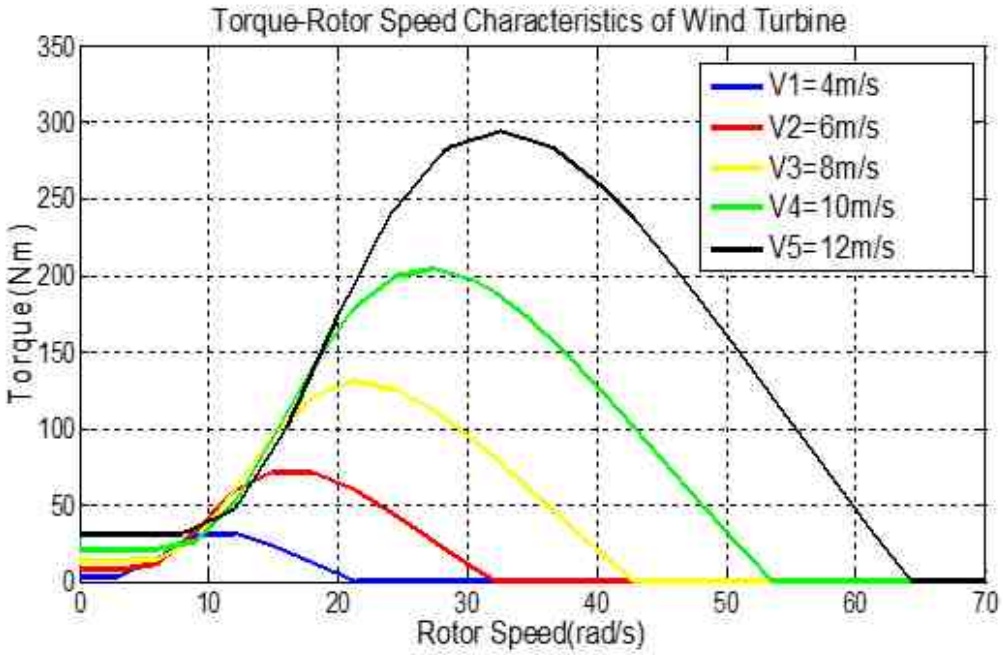


Fig. 3.5. Wind turbine torque vs. rotor speed.

From (3.1) and (3.2), the wind turbine output power is[1],

$$P = \frac{1}{2}\rho A C_p \frac{\omega^3 R^3}{\lambda^3} = K\omega^3 \tag{3.5}$$

$$T = K\omega^2 \tag{3.6}$$

where $T$ is wind turbine torque, $K$ is optimal coefficient which equals to $\frac{1}{2}\rho A C_p \frac{R^3}{\lambda^3}$. The $C_p$–$\lambda$ characteristics when the pitch angle is 0 degree is depicted in Figure 3.6, so the maximum value of $C_pmax$ is 0.48 and the optimal $\lambda_opt$ is 8.1 [1],[4],[46].

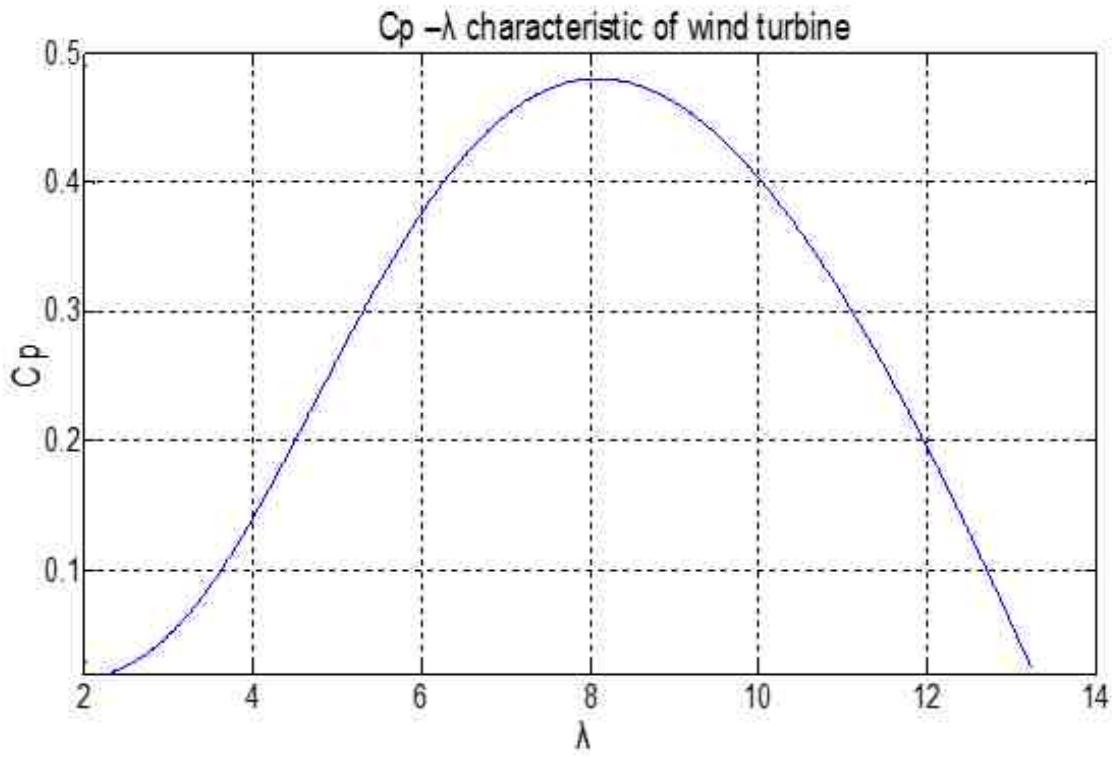


Fig. 3.6. $C_p$–$\lambda$ characteristic of wind turbine ($\beta$=0).

The simulink model of wind generation system is demonstrated in Figure 3.7, where the load side of the wind power system is a resistive load. Figure 3.8 illustrates the AC link voltage after the PMSG and the Figure 3.9 depicts the DC output voltage of wind generation system after rectifier.

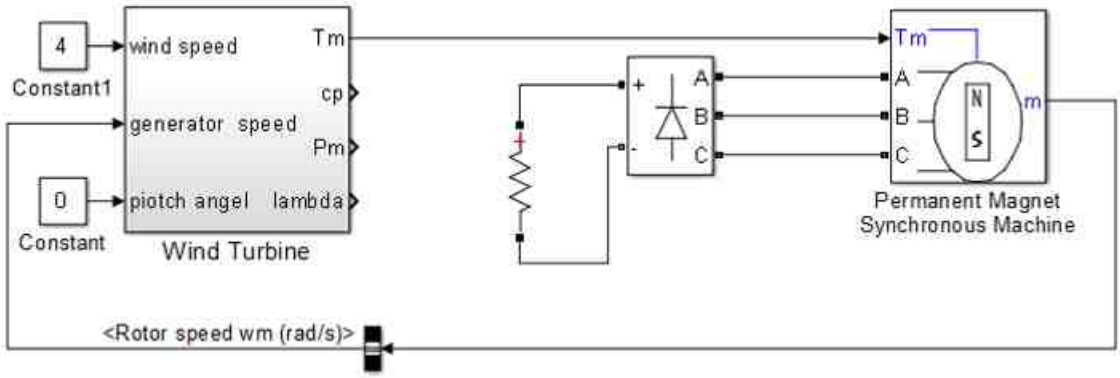


Fig. 3.7. Simulink model of wind power system.

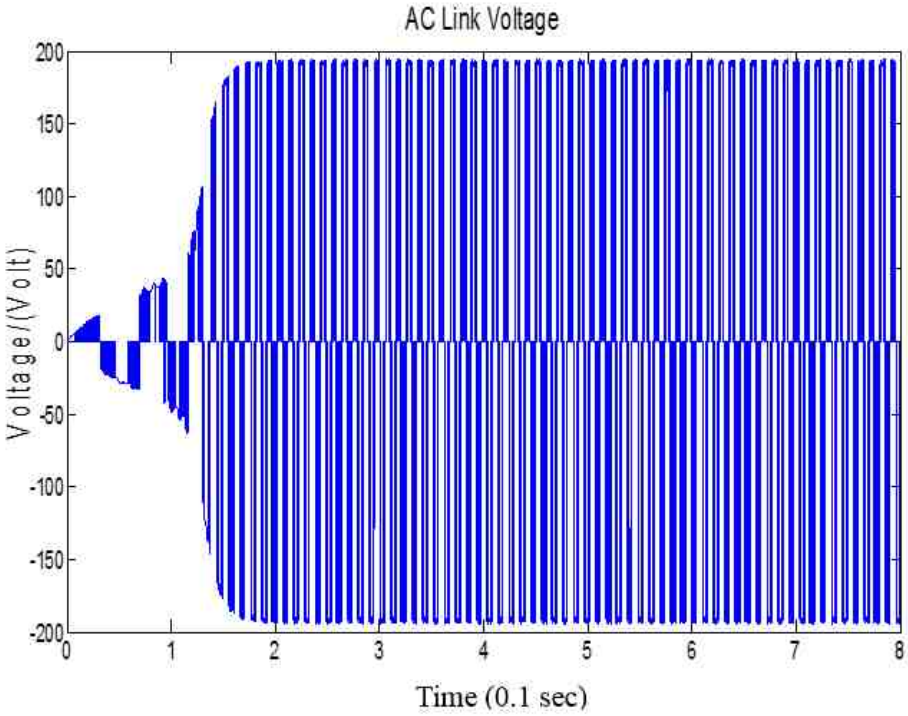


Fig. 3.8. AC link voltage after PMSG.

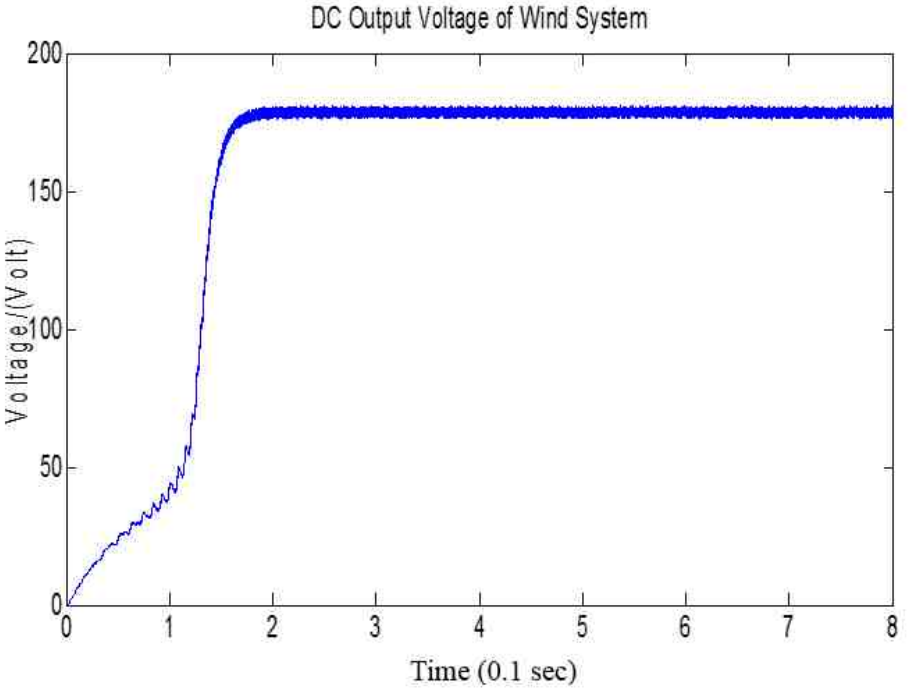


Fig. 3.9. DC output voltage of wind power system.

### 3.3 Modeling of Solar Power System

The PV module is also modeled in Matlab/Simulink based on the equivalent circuit of PV panel in Figure 3.10. The mathematical modeling of solar panel is expressed as below, and all the parameters can be obtained from engineering applications.

$$T_c = T_a + t_c R \tag{3.7}$$

Where,

R — Solar irradiation on the PV panel

$t_c$ — Coefficient of panel temperature

$T_a$ — Environment temperature

$T_c$ — Temperature of solar panel

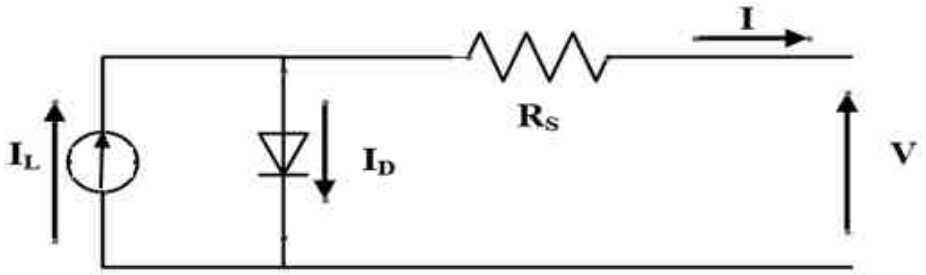


Fig. 3.10. Equivalent circuit of PV panel.

The I-V characteristics of solar panel can be represented by

$$I = I_{sc}(1 - C_1(e^{-\frac{V}{C_2 V_{oc}}} - 1)) \tag{3.8}$$

$$C_1 = (1 - \frac{I_m}{I_{sc}})e^{-\frac{V_m}{C_2 V_{oc}}} \tag{3.9}$$

$$C_2 = \frac{(\frac{V_m}{V_{oc}})}{ln(1 - \frac{I_m}{I_{sc}})} \tag{3.10}$$

Where,

$I_{sc}$ — Short circuit current

$V_{oc}$ — Open circuit voltage

$I_m$ — Current value at maximum power point

$V_m$ — Voltage value at maximum power point

When the effects of variations of solar irradiation and temperature are considered, the I-V characteristics of PV cell can be written as [49]:

$$I = I_{sc}(1 - C_1(e^{\frac{V-DV}{C_2 V_{oc}}} - 1)) + DI \tag{3.11}$$

$$DI = \frac{\alpha R}{R_{ref} DT} + (\frac{R}{R_{ref}} - 1) I_{sc} \tag{3.12}$$

$$DV = -\beta DT - R_s DI \tag{3.13}$$

$$DT = T_c - T_{ref} \tag{3.14}$$

Where,

$R_{ref}$ — Standard value of solar radiation ($1000 W/m^2$)

$T_{ref}$ — Reference value of temperature ($25°C$)

$\alpha$ — Variations of current over temperature at reference radiation ($Amps/°C$)

$\beta$ — Variations of voltage over temperature at reference radiation ($Volt/°C$)

$R_s$ — Equivalent series resistance ($\Omega$)

The representation of $R_s$ is presented as below [49]:

$$R_s = \frac{N}{N_p} R_{s,ref} = \frac{N}{N_p} (A_{ref} \frac{ln(1 - \frac{I_{m,ref}}{I_{sc,ref}} - V_{m,ref} + V_{oc,ref})}{I_{m,ref}} \tag{3.15}$$

$$A_{ref} = \frac{T_{c,ref} \mu V_{oc,ref} + \epsilon N_s}{\frac{\mu I_{sc} T_{c,ref}}{I_{L,ref}} - 3} \tag{3.16}$$

Where,

$\epsilon$ — Material band energy (1.12eV for silicon)

$I_{m,ref}$ — Maximum current of PV cell at reference weather condition

$V_{m,ref}$ — Maximum voltage of PV cell at reference weather condition

$I_{sc,ref}$ — Maximum short circuit current of PV cell at reference weather condition

$V_{oc,ref}$ — Maximum open circuit voltage of PV cell at reference weather condition

$\mu_{v,oc}$ — The Coefficient of open circuit voltage of PV cell at reference weather condition

$\mu_{I,sc}$ — The Coefficient of short circuit current of PV cell at reference weather condition

$N_s$ — Number of series PV cells

$N_p$ — Number of parallel PV cells

$T_{c,ref}$ — Reference temperature of PV cells

Based on the above mathematical models and the simulation parameters listed in Table 3.1. The simulink model of PV cells is established in Figure 3.11.

Table 3.1 The Simulation Parameters of PV Panel

| $V_{oc}$ | $I_{sc}$ | $V_m$ | $I_m$ | $P_m$ | $R_s$ | $T_{ref}$ | $R_{ref}$ |
|---|---|---|---|---|---|---|---|
| 129V | 19.2A | 105.6V | 17.1A | 1800w | 0.2Ω | $25°C$ | $1000W/m^2$ |

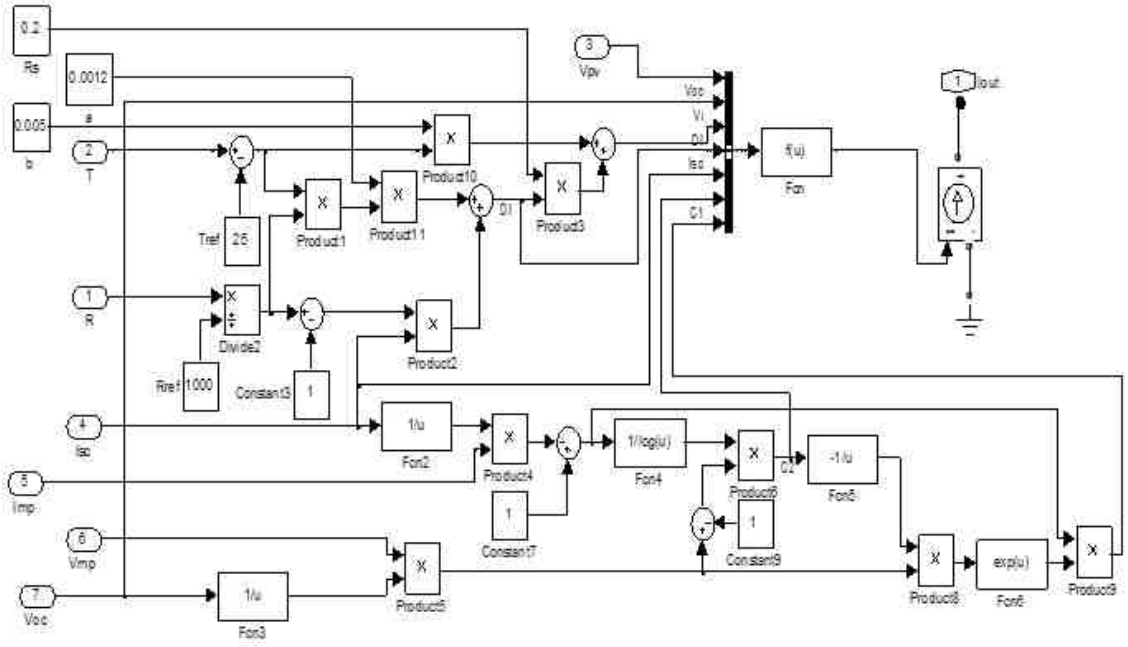


Fig. 3.11. Simulink model of PV cells.

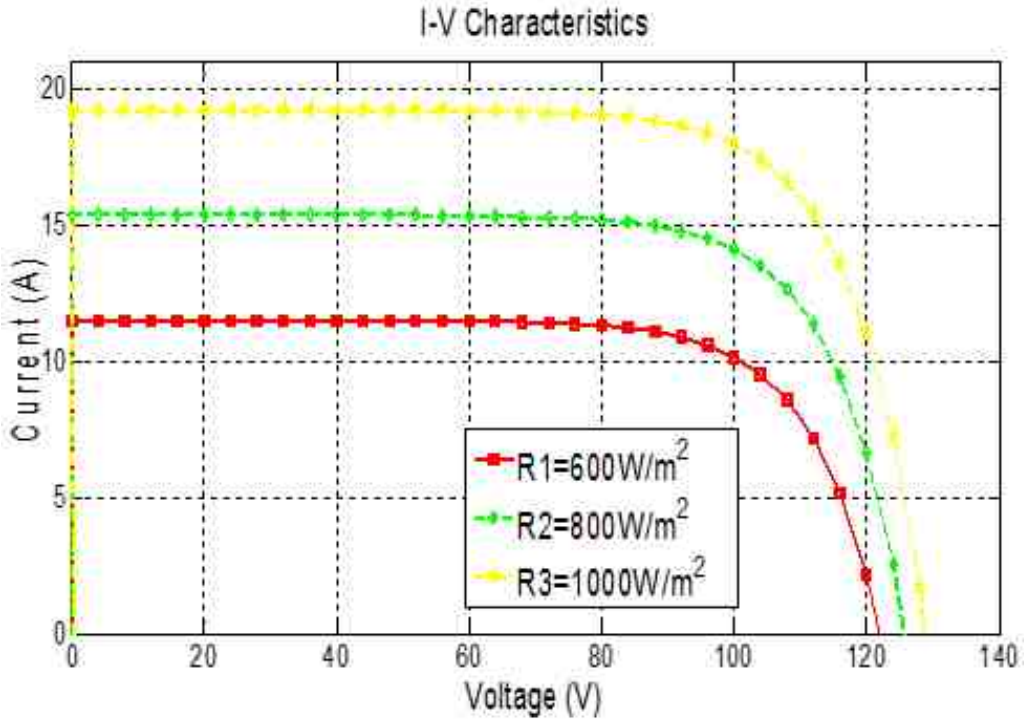


Fig. 3.12. I-V characteristics curve of PV model.

Figures 3.12 and 3.13 present the strong nonlinear curves of I-V and P-V curves of PV model at different solar illumination intensity levels[1], which are $600W/m^2$, $800W/m^2$ and $1000W/m^2$.

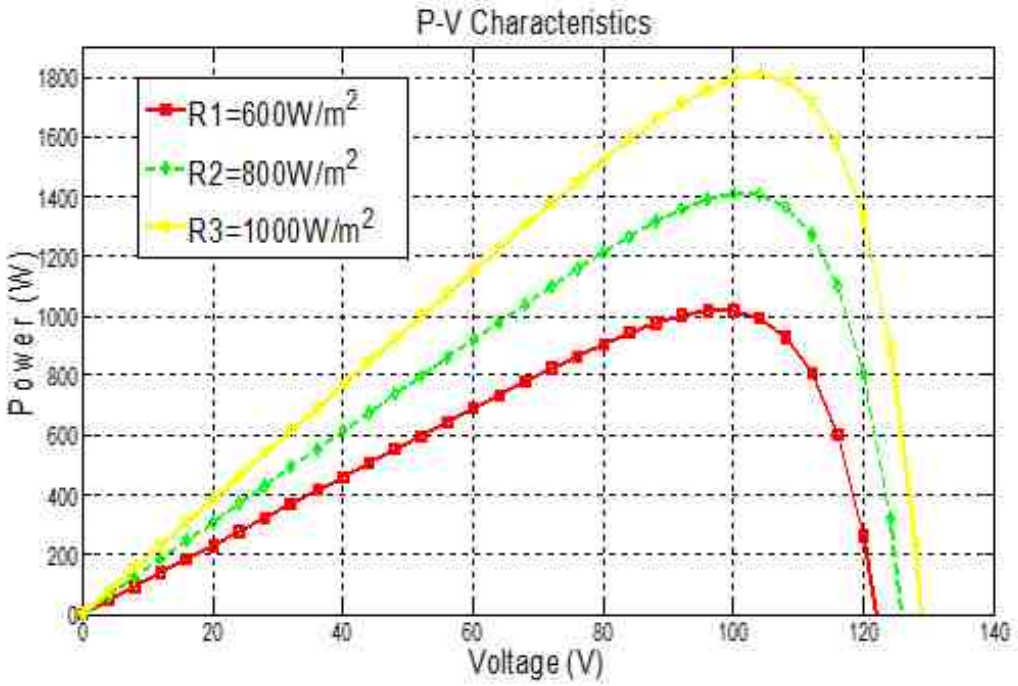


Fig. 3.13. P-V characteristics curve of PV model.

### 3.4 Modeling of Constant Power Load

Nowadays, by considering the effects of each units in DC microgrids on stability of system, the multi-stage distributed energy systems are becoming more and more popular, which contains the source stage, interface DC/DC converter stage and the common load, such as DC constant power load (CPL)[50-51]. The CPLs, e.g. DC motor, point-of-load (POL) converter with resistor etc., are also known as active loads, which can be regulated at the load side. The biggest difference between passive load and constant power load is consuming constant amount of power without consideration of input voltage. This characteristic makes the load side more flexible in practical applications. In addition, CPLs can be used in numerous fields that re-

late to microgrid combination, such as communications technology facilities where all data servers and telecom switches are constant power loads [49]. Therefore, the CPLs are abstracted more and more attention from research scientists.

For the constant power load, the instantaneous output power of it should be fixed based on the load requirements, and the load voltage and current can be adjusted to some extents according to the control demands. In practical applications, only above the minimum voltage value $V_{lim}$, the standard operation of DC constant power load can be observed. When the terminal voltage below the lower band value, the protection device will closed the CPLs. For the nature of constant power load, the output power of CPLs can be expressed as follows:

$$P_l = V_l I_l \tag{3.17}$$

where $P_l$, $V_l$ and $I_l$ are constant power consumed, terminal voltage and current of CPLs.

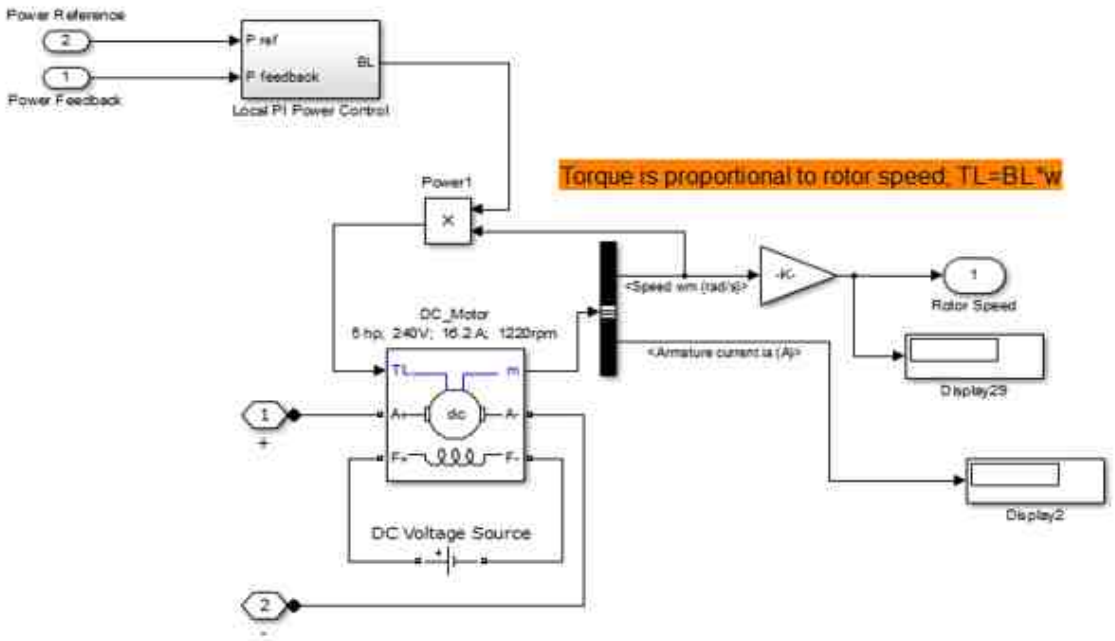


Fig. 3.14. Simulink model of CPLs.

In this thesis, the DC constant power load is mainly composed by a DC motor and a PI power controller. As depicted in Figure 3.14, the rated output power, terminal voltage, operation current and revolutions per minute of DC motor are 5hp, 240V, 16.2A and 1220rpm respectively. The torque TL applied on DC motor is proportional to the rotor speed, and the coefficient BL can be obtained from PI power controller, where the two inputs are power reference and power feedback of DC motor.

### 3.5 Modeling of DC/DC Converter and Battery

DC/DC converters can convert one DC voltage to another DC voltage which required by the load. They have been widely utilized in many areas such as power switches and motor drives due to the high conversion efficiency and reliability. There are many kinds of DC/DC converter including BUCK converter, BOOST converter and BUCK-BOOST converter, where BUCK-BOOST converter can also be separated into CUK converter, Flyback converter and SEPIC converter and many other configurations.In this thesis, the single BOOST converter, cascade BOOST converter and SEPIC converter are modeled and analyzed in proposed power system. The battery which can store surplus energy is also built and established in Matlab/Simulink.

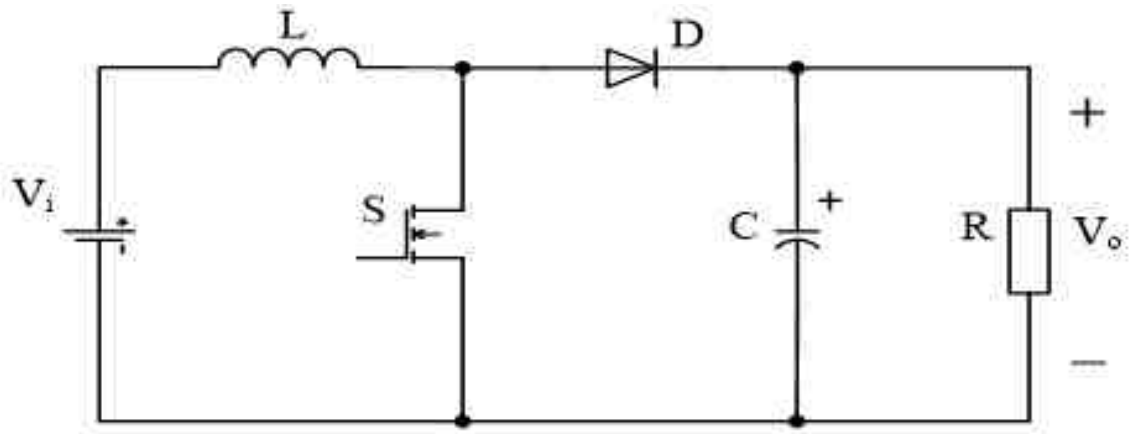


Fig. 3.15. Schematic diagram of BOOST converter.

A schematic diagram of BOOST converter has been illustrated in Figure 3.15. It consists of a power source $V_{in}$, inductor L, switch S, diode D, capacitor C and resistor R. The operation status of BOOST converter can be categorized into continuous current mode (CCM) and discontinuous current mode. Under CCM, BOOST converter has two equivalent circuit with the existence of power switch, which is shown in Figure 3.16. As demonstrated in (a), the switch S is closed, the inductor charged by the power supply, the diode is now reversed, so that the capacitor discharges to the load. When the switch S is open, because the current going through inductor cannot be changed instantaneously, the diode will be turned on due to the superimposition of induced electromotive and the power source. So now the energy in the inductor will be discharged to the load with the increment of output voltage.

With the control signals u applied on power switch, the mathematical state-space model of BOOST converter can be expressed as follows:

$$\begin{cases} L\dfrac{di_L}{dt} = -(1-u)V_o + V_i n \\ C\dfrac{dV_o}{dt} = (1-u)i_L - \dfrac{V_c}{R} \end{cases} \tag{3.18}$$

In order to get higher conversion ratio in solar system, the cascade BOOST converter is also built for integrated renewable energy system. The schematic diagram of cascade BOOST converter is illustrated in Figure 3.17. With control signals $u_1$ and $u_2$ for the two stage BOOST converter[2], the switched state-space model of the cascaded BOOST converter[2], the system dynamic behavior can be described from the following four differential equations according to Figure 3.17 by using the Kirchhoff's voltage and current laws as follows[2]:

$$\begin{cases} L_1 \dfrac{di_{L_1}}{dt} = V_p - V_{c_1}(1-u_1) \\ L_2 \dfrac{di_{L_2}}{dt} = V_{c_1} - V_{dc}(1-u_2) \\ C_p \dfrac{dV_P}{dt} = i_p - i_{L_1} \\ C_1 \dfrac{dV_{c_1}}{dt} = i_{L_1}(1-u_1) - i_{L_2} \end{cases} \tag{3.19}$$

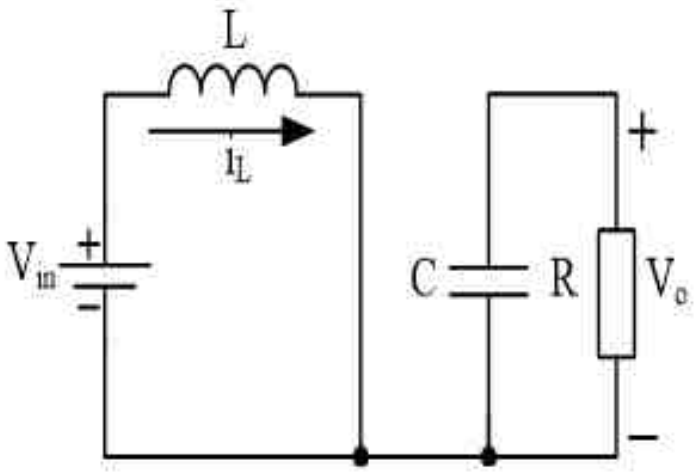


(a) Switch ON.

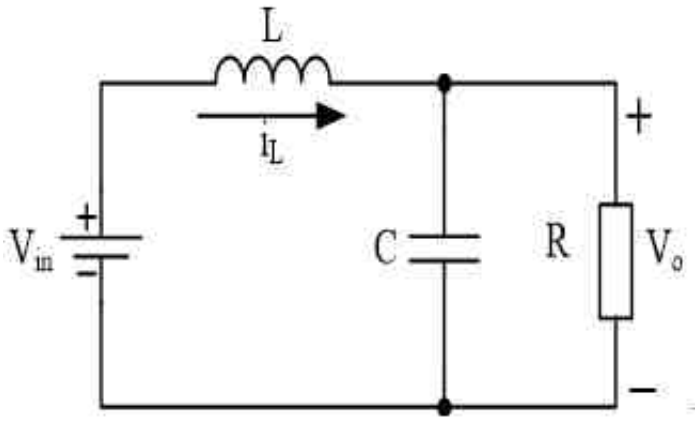


(b) Switch OFF.

Fig. 3.16. Two equivalent circuits of BOOST converter.

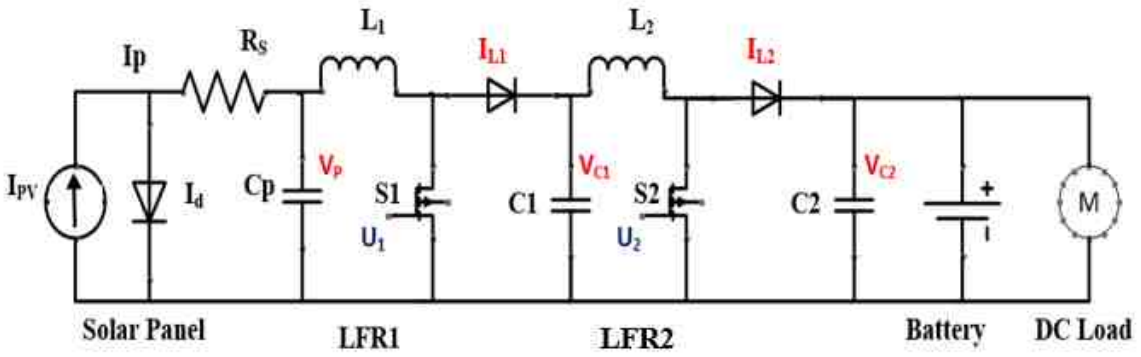


Fig. 3.17. Schematic diagram of cascade BOOST converter.

A schematic diagram of SEPIC converter has also been shown in Figure 3.18. It includes input capacitor $C_{in}$, two inductors $L_1$ and $L_2$, power switch $Q_1$, isolation capacitor $C_s$, diode $D_1$ and the output capacitor $C_{out}$. The SEPIC converter is called single ended primary inductance converter, the main advantage of SEPIC converter is that its output voltage is always positive regardless of input.

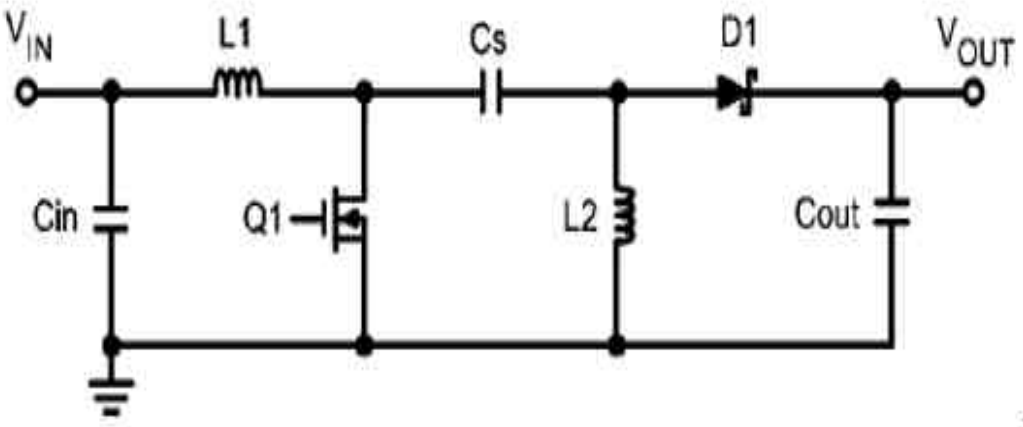


Fig. 3.18. Schematic diagram of SEPIC converter.

The two operation modes of SEPIC converter under CCM are depicted in Figure 3.19. When switch $Q_1$ is ON, there are $C_{in}$—$L_1$—$Q_1$ and $Q_1$—$L_2$—$C_s$ two loops in the circuit. The inductor $L_1$ is charged by the input voltage $V_{IN}$, and the energy stored in the $C_s$ discharge to the inductor $L_2$. Thus the output capacitor $C_{out}$ satisfies the load due to the reversed diode. When switch $Q_1$ is OFF, there are still two loops

in the circuit, they are $C_{in}$—$L_1$—$C_s$—$L_2$ and $L_2$—$D_1$—$C_{out}$. Now the capacitor $C_s$ is charged by the input voltage $V_{IN}$ and the induced electromotive force of inductor $L_1$. $L_2$ discharges to the output capacitor $C_{out}$, and then $C_{out}$ discharges to the load.

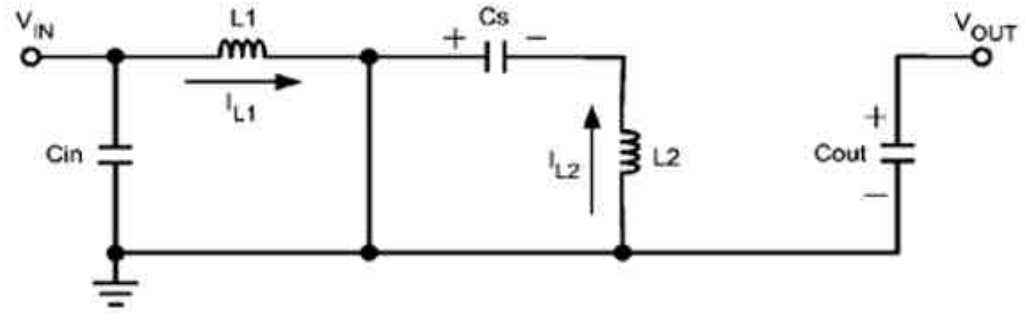


(a) Switch ON.

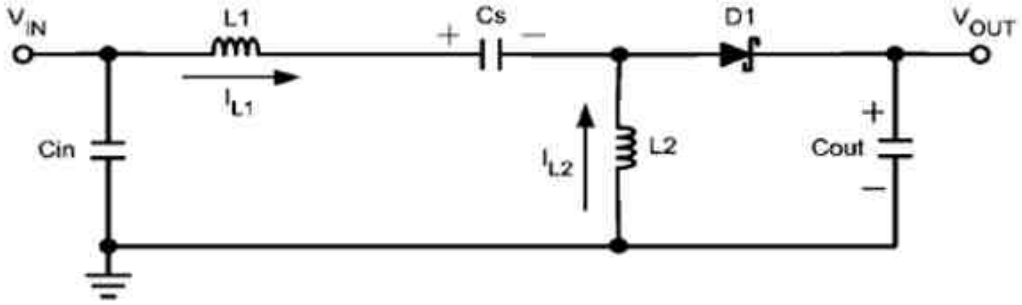


(b) Switch OFF.

Fig. 3.19. Two operation modes of SEPIC converter.

By applying the control signal u and ignoring the input capacitor $C_{in}$ in the previous figures, the state-space model of SEPIC converter can present its dynamic operation as follows:

$$\begin{cases} L_1 \dfrac{di_{L_1}}{dt} = V_{in} - (V_{c_s} + V_{C_{out}})(1-u) \\ C_s \dfrac{dV_{C_s}}{dt} = (1-u) i_{L_1} - u i_{L_2} \\ L_2 \dfrac{di_{L_2}}{dt} = u V_{C_s} - V_{out}(1-u) \\ C_{out} \dfrac{dV_{C_{out}}}{dt} = (i_{L_1} + i_{L_2})(1-u) - i_{L_2} \end{cases} \tag{3.20}$$

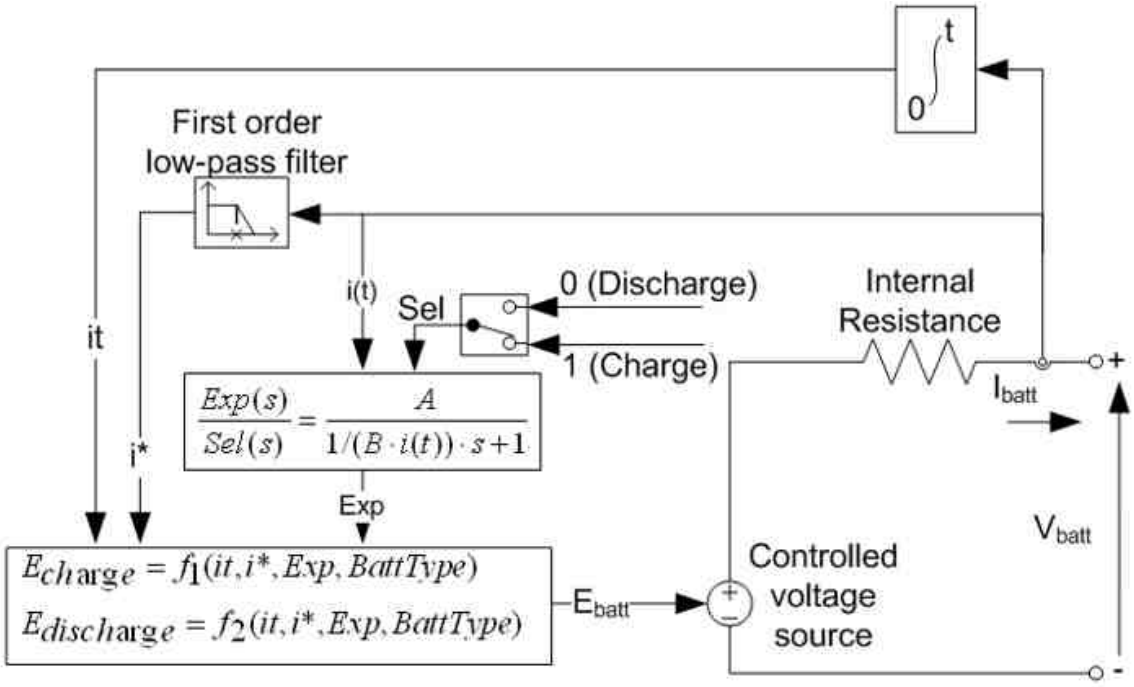


Fig. 3.20. Equivalent circuit of battery.

The storage device used in the thesis is the lead-acid battery, which can be directly chosen in the SimPowerSystems of Matlab/Simulink, which can be represented by the equivalent circuit of battery in figure 3.20. Some fundamental parameters of battery are its nominal voltage, rated capacity and state of charge. By taking reference from Matlab/Simulink, the mathematical model of charging and discharging battery are as follows:

Discharge model ($i^* > 0$)

$$f_1(it, i^*, i, Exp) = E_o - K\frac{Q}{Q - it}i^* - K\frac{Q}{Q - it}it + Laplace^{-1}[\frac{Exp(s)}{Sel(s)}0] \quad (3.21)$$

Charge model ($i^* < 0$)

$$f_2(it, i^*, i, Exp) = E_o - K\frac{Q}{0.1Q + it}i^* - K\frac{Q}{Q - it}it + Laplace^{-1}[\frac{Exp(s)}{Sel(s)}\frac{1}{s}] \quad (3.22)$$

Where,

$E_0$ — Constant voltage (V)

Exp(s) — Exponential zone dynamics (V)

Sel(s) — Represents the battery mode.Sel(s) = 0 during battery discharge,Sel(s) during battery charging

K — Polarization constant (Ah-1) or Polarization resistance (Ohms)

$i^*$— Low frequency current dynamics (current comes through a low-pass filter)

i — Battery current (A)

it — Extracted capacity (Ah)

Q — Maximum battery capacity (Ah)

## 3.6 Modeling of Other Components

This section introduces some other components of the combined energy system, such as permanent magnet synchronous machine (PMSM) and the three phase universal bridge. They are all directly used from the Matlab/Simulink.

The PMSM block in Simulink can operate in either generator mode or motor mode. It can transfer mechanical power from the wind turbine to electric energy and deliver them to the circuit. The mode of operation is dictated by the sign of applied

mechanical torque, which is positive for motor mode, negative for generator mode. The sinusoidal model selected in PMSM block assumes that the flux established by the permanent magnets in the stator is sinusoidal, which implies that the electromotive forces are sinusoidal waveform. The simulink model of PMSM working at generator mode is shown in Figure 3.21. The input of PMSM is mechanical torque generated from the prime mover, which equals to the output torque of wind turbine regardless of gear box. The two outputs are rotor speed of PMSM and the three-phase voltage. The following three equations of three-phase sinusoidal model electrical system are presented in the rotor reference frame (qd frame), which means all the quantities in the rotor reference frame are corresponding to the stator as follows:

$$\begin{cases} L_d \dfrac{di_d}{dt} = V_d - Ri_d + L_q \rho \omega_r i_q \\ L_q \dfrac{di_q}{dt} = V_q - Ri_q + L_d \rho \omega_r i_d - \lambda \rho \omega_r \\ T_e = \dfrac{3}{2} \rho [\lambda i_q + (L_d - L_q) i_d i_q] \end{cases} \tag{3.23}$$

Where,

$L_q$, $L_d$ — q and d axis inductances

R — Resistance of stator windings

$I_q$, $I_d$ — q and d axis currents

$V_q$, $V_d$ — q and d axis voltages

$\omega_r$ — Angular velocity of rotor

$\lambda$ — Amplitude of the flux induced by the permanent magnets of rotor in stator phases

$\rho$ — Number of pole pairs

$T_e$ — Electromagnetic torque

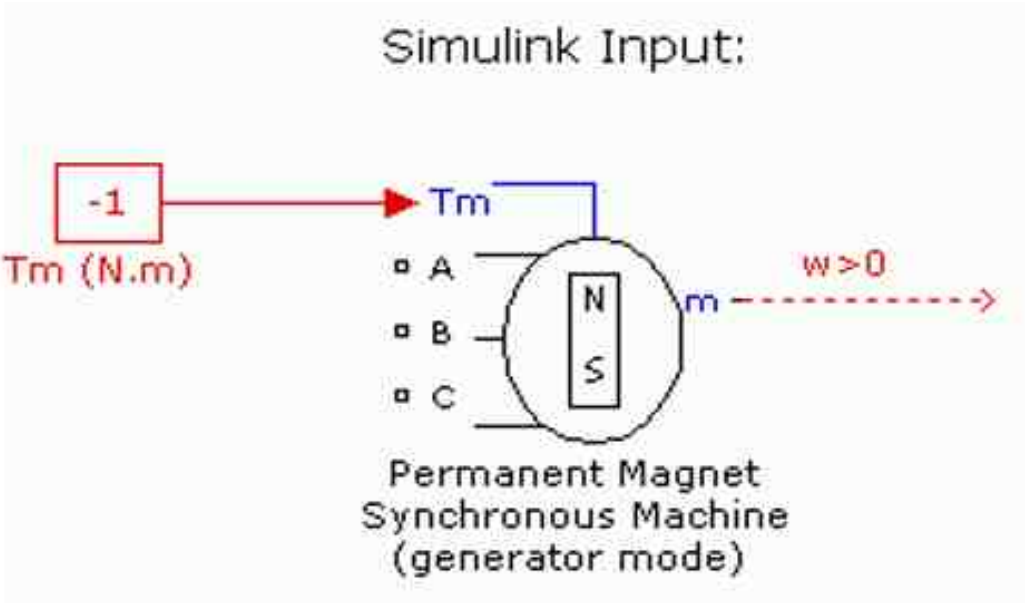


Fig. 3.21. Simulink model of PMSM.

The universal bridge block implements a universal three-phase power AC/DC converter, which concludes of maximum to six power switches in each bridge. As depicted in Figure 3.22, the model utilized in the thesis contains diodes in the universal bridge configuration, each arm has two diodes. The DC link output voltage can be obtained below:

$$V_{dc} = \frac{3\sqrt{3}V_{peak}}{\pi} \tag{3.24}$$

Where,

$V_{peak}$ — Peak value of phase (line to neutral) input voltages

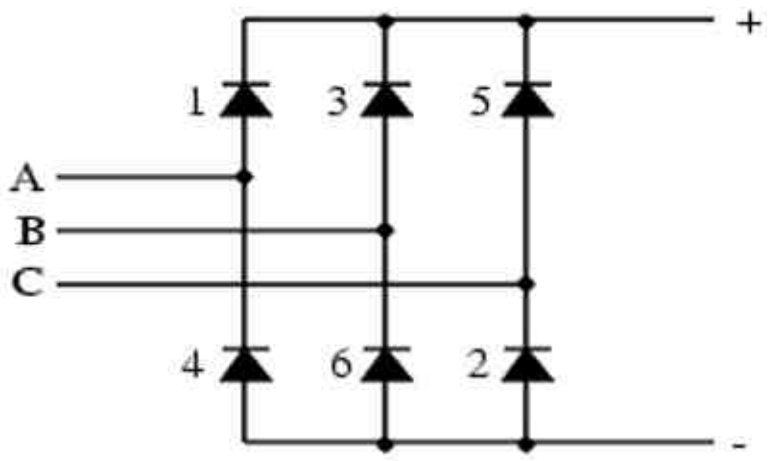


Fig. 3.22. Circuit diagram of three-phase universal bridge.

## 3.7 State-Space Models of Hybrid Power Systems

This section presents the state-space models of the hybrid DC power systems. The state-space representations are categorized into four cases based on the configurations of combined DC power systems in Chapter 2 and the mathematical models of every single components in the system. As can be seen in the following figure[3], the state-space models and the corresponding applied control signals of wind-wind-storage DC power system, the state-space model of solar-solar-storage DC power system, the state-space model of wind-solar-storage DC power system and the state-space mode of wind-solar DC power system are demonstrated in Figure 3.23 to Figure 3.26 respectively.

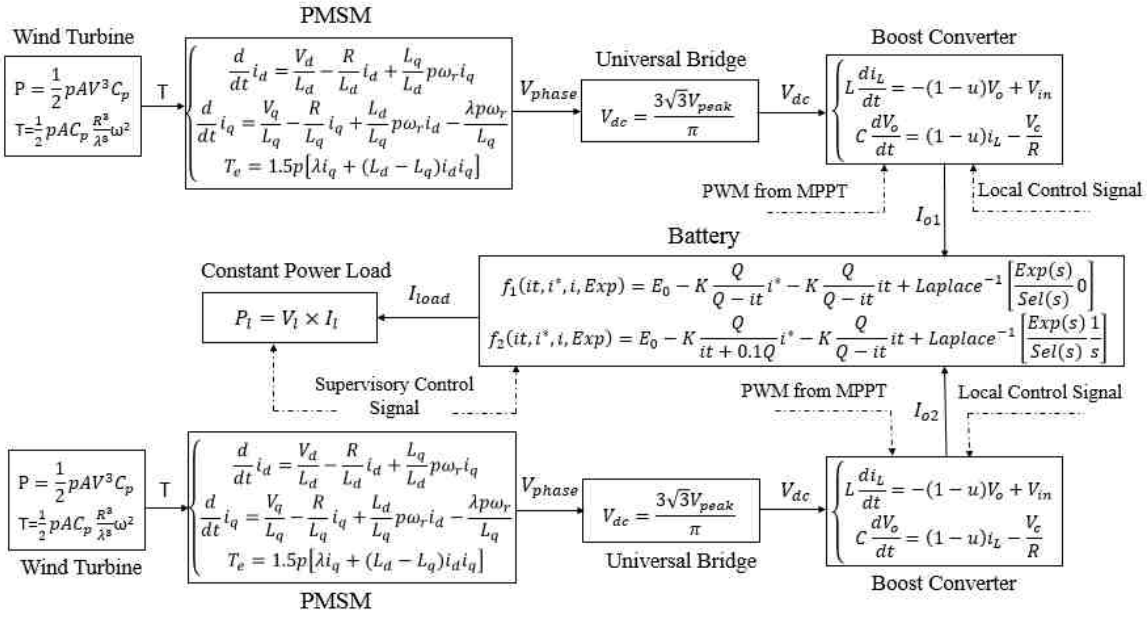


Fig. 3.23. State-space model of wind-wind-storage DC power system.

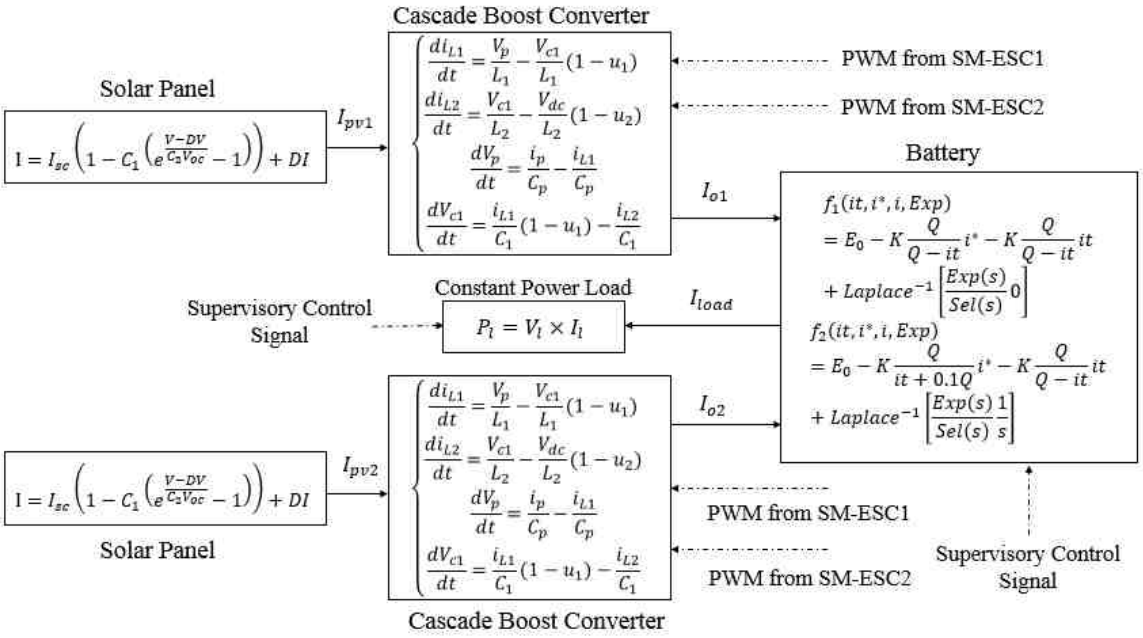


Fig. 3.24. State-space model of solar-solar-storage DC power system

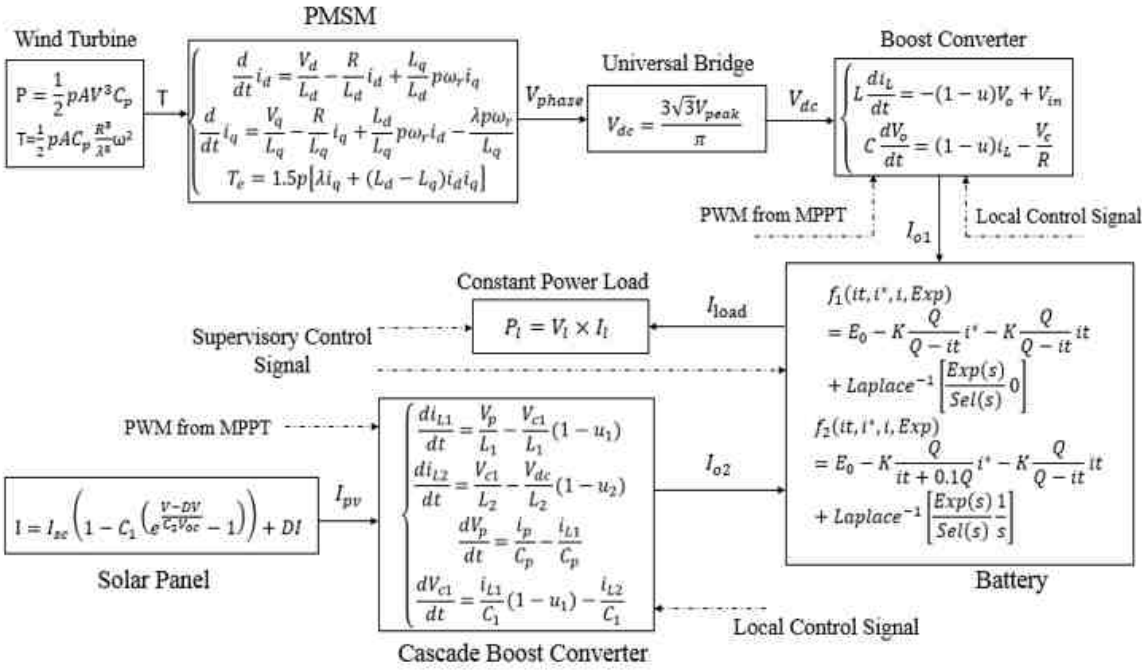


Fig. 3.25. State-space model of wind-solar-storage DC power system

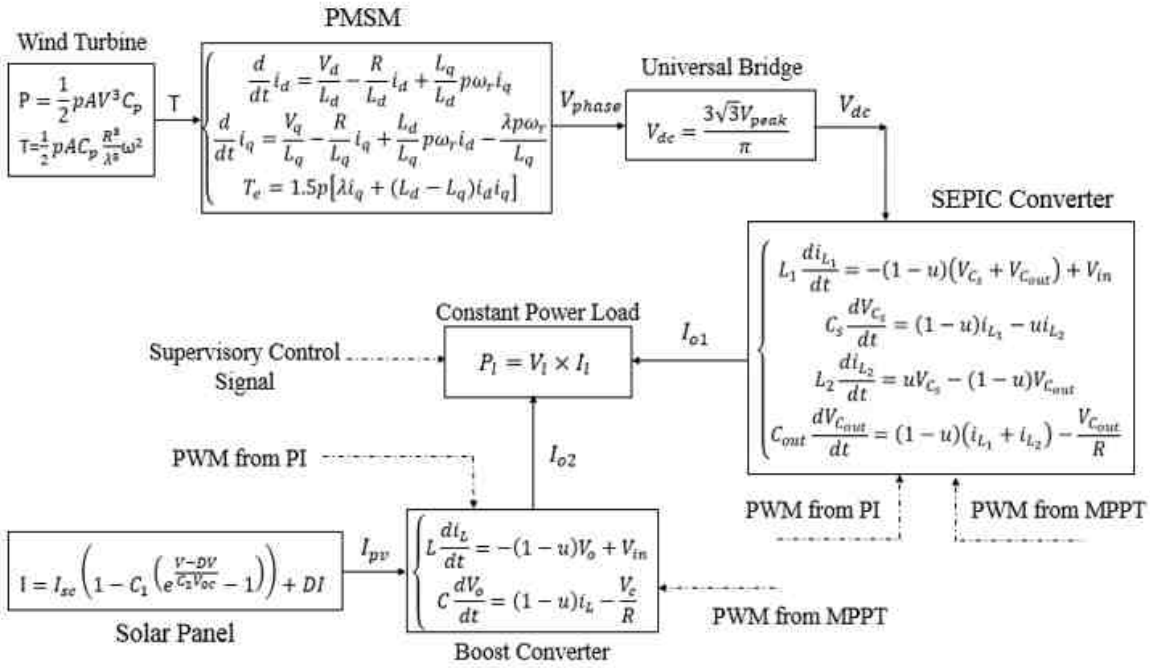


Fig. 3.26. State-space mode of wind-solar DC power system

# 4. CONTROL FOR HYBRID DC POWER SYSTEM

Chapter 4 introduces the control strategy for the integrated wind-solar-storage DC energy system, which includes maximum power point tracking methods for both wind and solar system and the supervisory control for the entire hybrid power system. First of all, this chapter presents some traditional wind MPPT methods, such as Tip Speed Ratio (TSR), Power Signal Feedback Control (PSF) and Perturbation and Observation (P&O)[4]. After that, the new Sliding Mode Extremum Seeking Control (SMESC) which combines sliding mode and extremum seeking control theories has been discussed[4]. Moreover, for solar system, the traditional MPPT control methods of P&O and the new MPPT strategy of SMESC are also introduced and designed. At last, according to the changing of weather condition, SOC of battery and the load requirement, the supervisory control strategies are established.

## 4.1 Control Methods for Wind Maximum Power Point Tracking

As discussed in the previous Chapter, according to the aerodynamic characteristic of wind turbine, it cannot absorb the wind energy completely[4]. Based on the ideal model of wind turbine, the wind turbine output the maximum power when and only when the wind speed in front of the turbine has been decreased to one third to original, so that the wind utilization coefficient reaches the maximum value 17/26, and the wind turbine can convert nearly 59.3% of wind energy without any power losses[4].

From Figure 3.3, the relationship between the wind utilization coefficient $C_p$ and the tip speed ratio $\lambda$ can be identified, where $\lambda$ is defined as ratio of wind turbine blade tip rotation circumferential velocity and wind speed. With regard to the fixed wind

turbine utilized in the thesis, the $C_p$ value changes with the variations of tip speed ratio, because it is a single-peak function, which means that only under one specific $\lambda$ value, the wind utilization coefficient can be maximized. Therefore, the control method with the effect of capture and keep the maximum $C_p$ value by regulating the rotor speed of wind turbine is called MPPT[1].

### 4.1.1 Tip Speed Ratio Control

The TSR control refines the rotational speed to keep the optimal tip-speed ratio for the maximum wind power utilization coefficient under different wind speeds[1]. Figure 4.1 depicts the control block diagram of TSR. After measuring the wind speed v and the rotation speed of wind turbine, the actual tip speed ratio can be calculated, and then based on the error of actual value and the optimized tip speed ratio, a closed-loop controller can be designed and applied to find and maintain the best operation point.

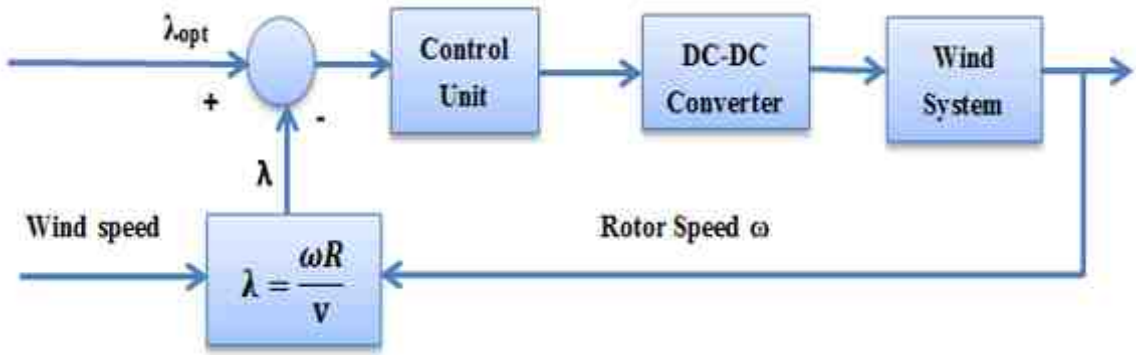


Fig. 4.1. Control Block Diagram of TSR

The advantage of this method is the simple implementation[1]. The system can be controlled by a PI controller without static error theoretically[1]. However, because of the requirement of wind information, the performance of TSR control approach relies on the anemometer accuracy or the estimated wind speed[1]. There

are strong non-linearity and uncertainty of wind speed in time and space, so it is difficult to achieve accurate measurement. In addition, different wind turbines has different optimized tip speed ratios, so the portability of the algorithm is poor.

### 4.1.2 Power Signal Feedback Control

The PSF controller is mainly based on the maximum power characteristics curve resulting from simulation or field tests[1]. The curve can be stored in form of lookup table in the controller[1]. Based on the error of benchmark output power from the table and the real output power from the system, the closed-loop controller regulates the rotor speed of wind turbine and then achieve the maximum power point. The PSF control block diagram is shown in Figure 4.2.

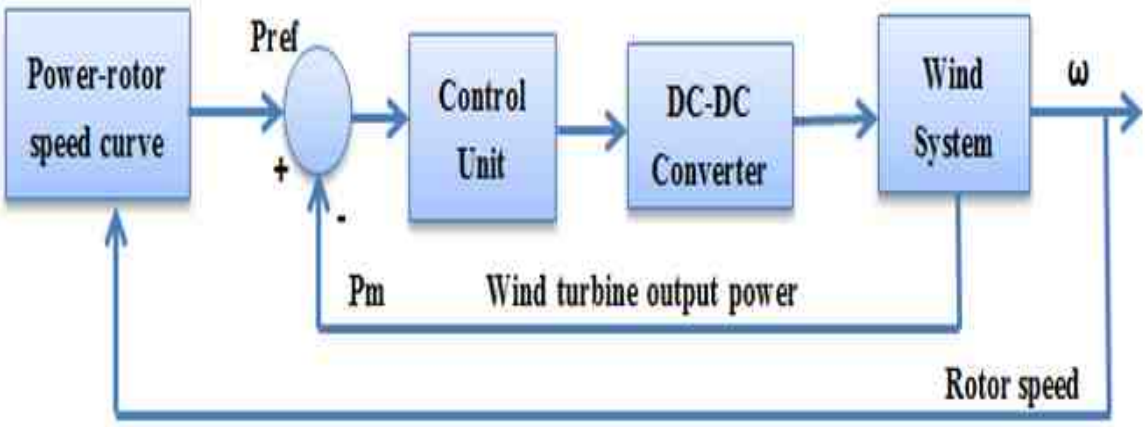


Fig. 4.2. Control Block Diagram of PSF

Figure 4.3 shows the relationship of wind turbine maximum power characteristic and maximum power point capturing curve. In the figure, the black curve is the wind turbine output power vs. wind turbine rotor speed[1], and the red curve is the MPP tracking feature. Assuming the wind speed is $v_1$ and the actual rotor speed is $\omega_1$, the corresponding maximum power point $P_1$ can be obtained by PSF controller. If wind speed changes from $V_1$ to $V_2$, the output power of wind turbine also changes from $P_1$ to $P_1{}'$ due to the reason of inertia, but actually the maximum power point of wind

turbine should be around $P_0$ that is larger than the captured power $P_1{}'$. Therefore, the PSF controller increases the rotor speed from $\omega_1$ to $\omega_0$, and track the MPP $P_0$ to make the wind system more efficient.

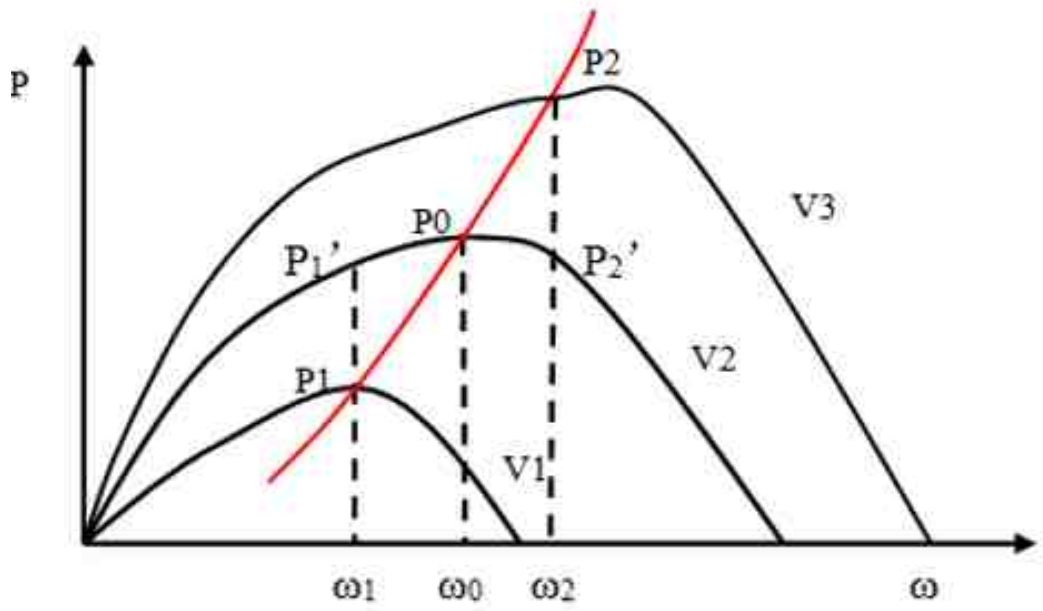


Fig. 4.3. Relationship of wind turbine maximum power characteristic and maximum power point capturing curve

It obvious to conclude the controller is easy to implement for tracking of the best rotor speed to generate the corresponding power reference value without the need for wind speed measurement[1]. Moreover, PSF is a stable approach as the data is interpolated from the data points available in the experimentally recorded lookup table[1]. However, it is difficult to obtain the accurate field data during the experiment[1]. Also, different wind turbines has different characteristic curves, so the portability of this method is poor[1].

### 4.1.3 Perturb and Observe Control

The P&O technique mainly generates a rotor speed perturbation and observes the variation of the output power to search for the point of maximum power. In

the proposed wind power system, the input power is constant when the wind speed is constant[1]. Therefore, according to the principle of conservation of energy, if the output power can be increased, the energy consumed in the generator is decreased and then the rotor speed of generator is decreased[1]. A DC/DC converter is employed to connect the wind turbine and load[1]. With the increase of duty cycle, the output voltage increases and leads to the increment of output power[1]; with the decrease of duty cycle, the output voltage decreases and leads to the decrement of output power[1]. Thus, the P&O method for wind MPPT can be accomplished by adjusting the duty cycle of DC/DC converter to change the rotor speed and keep the maximum $C_p$[1]. Figure. 4.4 demonstrates the variation of rotor speed when tuning the duty cycle[3]. Figure 4.5 demonstrates the control block diagram of P&O method[1].

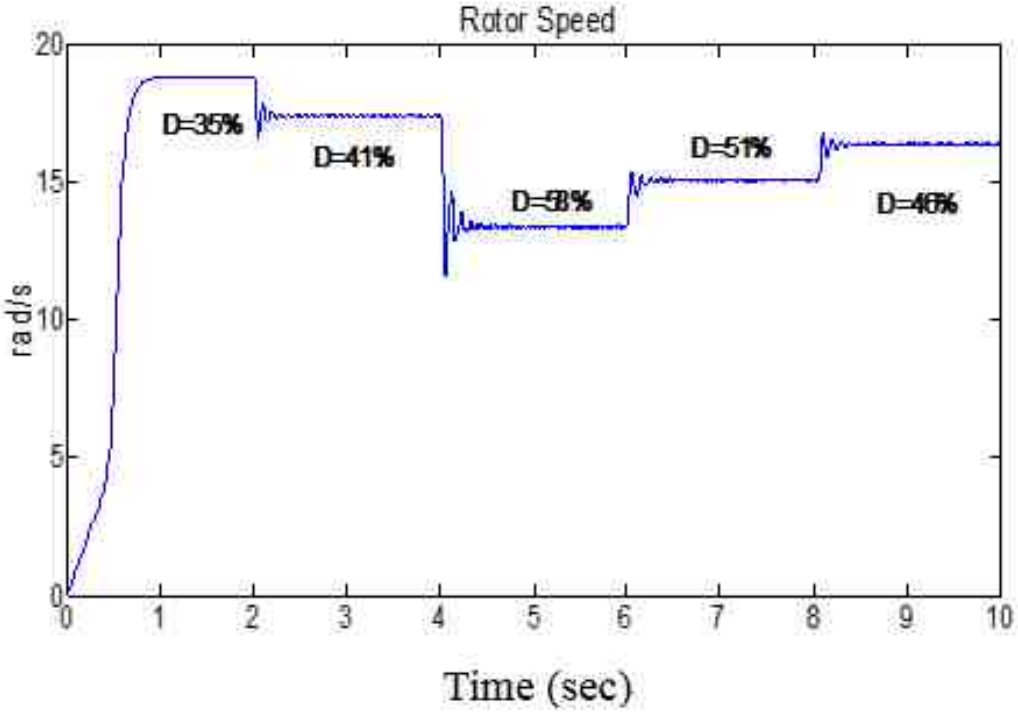


Fig. 4.4. Variation of rotor speed

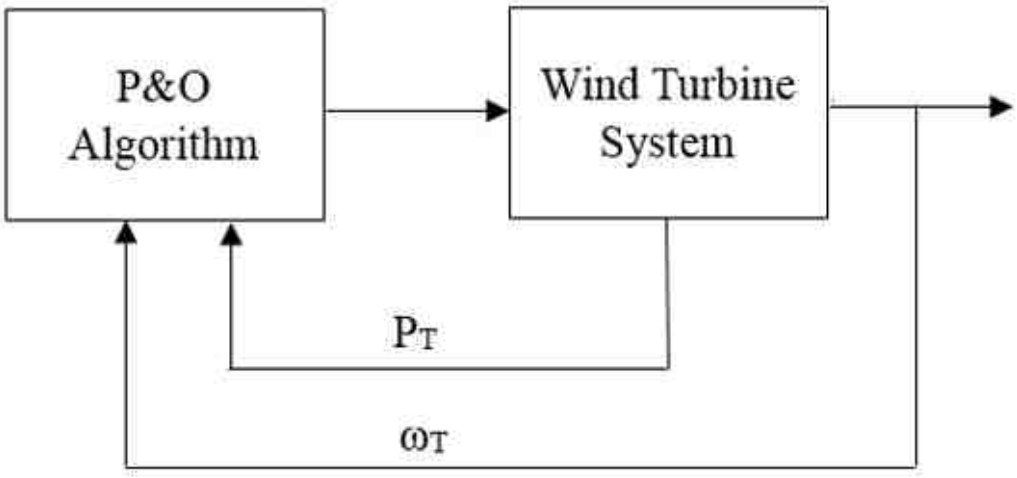


Fig. 4.5. Control block diagram of P&O

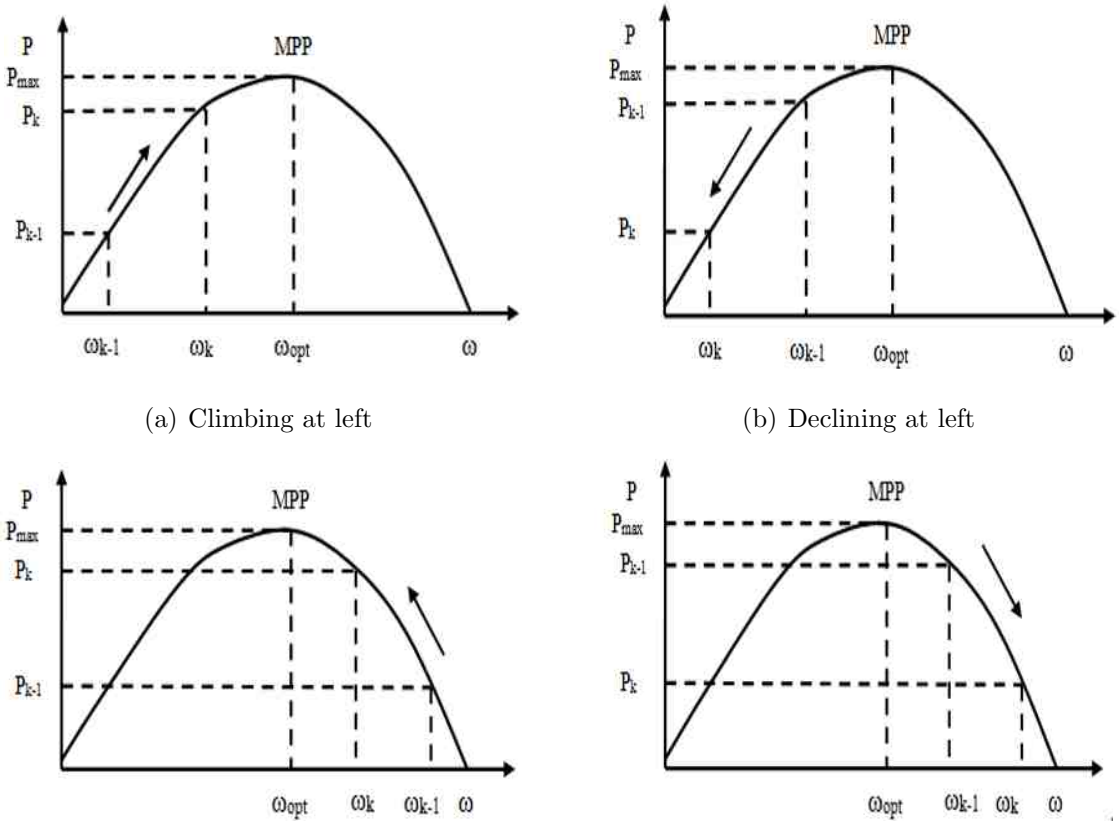


(a) Climbing at left

(b) Declining at left

(c) Climbing at right

(d) Declining at right

Fig. 4.6. MPPT control strategy for wind power system

As can be seen in Figure 4.6, assuming the wind speed is constant, the MPPT control for wind system can also be categorized into four circumstances[3]:

In Figure 4.6 (a), $P_k > P_{k-1}$ and $\omega_k > \omega_{k-1}$, the output power at k moment is larger than that of k-1 moment, so the operating point is at the left side of MPP[1]. $\omega_k > \omega_{k-1}$ means that the rotor speed increases, so the last duty cycle perturbation is negative[1]. This causes that the next perturbation become negative[1].

In Figure 4.6 (b), $P_k < P_{k-1}$ and $\omega_k < \omega_{k-1}$, the output power at k moment is less than that of k-1 moment, so the operating point is at the left side of MPP[1]. $\omega_k < \omega_{k-1}$ means that rotor speed decreases, so the last duty cycle perturbation is positive[1]. This causes that the next perturbation to become negative[1].

In Figure 4.6 (c), $P_k > P_{k-1}$ and $\omega_k < \omega_{k-1}$, the output power at k moment is larger than that of k-1 moment, so the operating point is at the right side of MPP[1]. $\omega_k < \omega_{k-1}$ means that rotor speed decreases, so the last duty cycle perturbation is positive[1]. This causes that the next perturbation become positive[1].

In Figure 4.6 (d), $P_k < P_{k-1}$ and $\omega_k > \omega_{k-1}$, the output power at k moment is less than that of k-1 moment, so the operating point is at the right side of MPP[1]. $\omega_k > \omega_{k-1}$ means that rotor speed increases, so the last duty cycle perturbation is negative[1]. This causes that the next perturbation to become positive[1].

The control command of P&O method can be expressed in terms of the four circumstances in Figure 4.6:

$$D(n) = D(n-1) + sign(\Delta P)sign(\Delta\omega)D_{step} \tag{4.1}$$

Where D(n) is the control signal for DC/DC converter, $\Delta P$ and $\Delta\omega$ are variations of output power from wind turbine and variations of rotor speed. $D_{step}$ represents the step size of converter control signal.

The advantage of the P&O method is that it requires neither wind turbine characteristics curve nor the generator parameters, so the control system can be used even under parameters changes[1]. However, the P&O method loses its effectiveness in large-scale wind turbine systems because the generator power is largely influenced by the variation of turbine inertia[1]. In addition, this method generates power generation oscillations that might become very large in higher power rating systems[1]. As typical MPPT control methods are shown in Figure 4.5, the P&O method can eliminate the measurement of wind speed so it is widely used for its ease of implementation[1].

### 4.1.4 Sliding Mode Extremum Seeking Control

In order to catch the $C_{pmax}$ from the nonlinear curve of $C_p$-$\lambda$ and improve the MPPT performance of extremum seeking control method, this paper presents the SM-ESC to further enhance the output response of wind power by combining sliding mode and extremum seeking control theories[4]. Although conventional ESC MPPT has already been used well in many solar and wind applications [4],[47]-[48], the switching function sign (s) usually operates at infinite frequency to reach the ideal condition[4]. Such high switching frequency cannot be accomplished in actual systems and also make the output unstable with creation of high frequency noise (chatter) [4],[49]-[50]. Hence, the sliding layer control concept which effectively avoids the operation of continuous switching is proposed[4]. A three states function of sliding layer replaces sign (s) as follows [4],[49]:

$$sat(s,\alpha) = \begin{cases} 1, s > \alpha \\ \frac{s}{\alpha}, |s| \leq \alpha \\ -1, s < -\alpha \end{cases} \tag{4.2}$$
$$= \begin{cases} sign(s), |s| > \alpha \\ \frac{s}{\alpha}, |s| \leq \alpha \end{cases}$$

The switching space can be separated into three regions, namely $s > \alpha$ ,$|s| \leq \alpha$, and $s < -\alpha$, where $|s| \leq \alpha$ indicates the sliding layer, $\alpha$ represents the thickness of the sliding layer[4]. The function sat(s,$\alpha$) is showing switching surface for a manifold defined by x: s(x) =0. As shown in Figure 4.7, SM-ESC utilizes the three states switch to replace sign(s) in ESC and can achieve better effect of high frequency oscillation[4]. Figure 4.8 is the wind MPPT scheme based on SM-ESC [49], [50], in which the variable s represents the sliding surface[4].

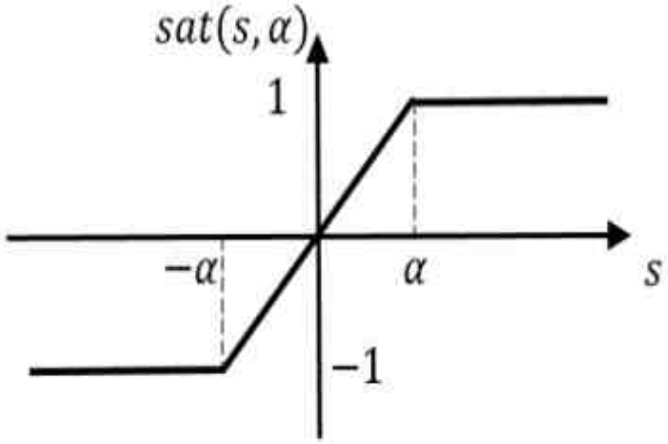


Fig. 4.7. Sliding layer concept

The specific parameters of the controller in Figure 4.8 can be expressed as follows[4]:

$$s = \gamma - y \tag{4.3}$$

$$u = U_0 sign(s) \tag{4.4}$$

$$\frac{d\gamma}{dt} = \rho - z \tag{4.5}$$

$$z = Z_0 sat(s, \alpha) \tag{4.6}$$

$$d = G + u \tag{4.7}$$

where $\rho$, $Z_0$, $U_0$ and G are constants; x is the input signal for the wind energy system; y is the mechanical output power of wind turbine[4]. The variable d is duty cycle of the DC-DC BOOST converter[4]. This has to satisfy the following relationship $Z_0 >> \rho$ and $Z_0 >> U_0$[4]. For MPPT controller rely on SM-ESC in this system the following is considered $\rho = 250$ , $Z_0 = 15000$, $\alpha = 0.02$ and G=0.7[4].

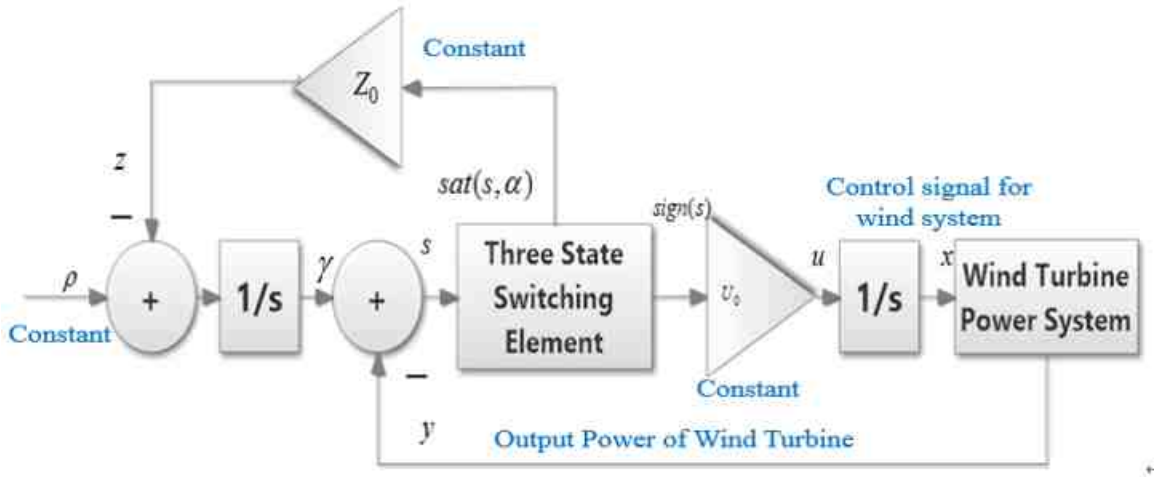


Fig. 4.8. Block diagram of sliding mode extremum seeking control algorithm

Parameter $U_0$ presents the step size of controller[4]. The adaptive step size based on the wind speed variations is also applied in SM-ESC for tuning control signal[4]. Initially, $U_0$ is 12e-5 because it cannot be too large or too small due to the requirements of tracking speed and stability of the system[4]. When the system operating point is approaching to the MPP, which means the absolute value of power variation is

smaller than 2W and the power coefficient $C_P$ is over 0.4795, so that the step size $U_0$ should changes to 2e-5 by using the Hysteretic Comparator with the sampling time 0.005 sec, which can make the elapsed time exceed five time constant of the circuit[4]. Hence, the current and voltage could reach steady-state response around maximum power point[4]. Moreover, there are different step size regarding the wind speed changing[4]. $U_0$ is 5e-5 with positive perturbation and 12e-5 with negative perturbation when wind speed is increasing; $U_0$ is 12e-5 with positive perturbation and 5e-5 with negative perturbation when wind speed is decreasing[4].

## 4.2 Control Methods for Solar Maximum Power Point Tracking

A solar power system usually consists of solar panels, power converters and load[1]. The maximum power point can be captured by tuning the controller and regulating the converter[1]. Some MPPT control methods have also been proposed for PV generation system to eliminate the probable mismatch between load current and PV voltage and point of maximum power[1]. In this way, tracking MPP is quite important for solar system not only to enhance the efficiency of system but also to reduce the cost of energy[1]. These technologies include the fractional open-circuit voltage over short circuit current method, the incremental conductance (INC) method, the P&O method, the power differential feedback control, the dc-link capacitor droop control and some other intelligent control methods[1]. Among them, the P&O method have been widely adopted because of its simplicity and system independency[1]. Therefore, the P&O method and the new sliding mode extremum seeking control will be designed and introduced in this section[1].

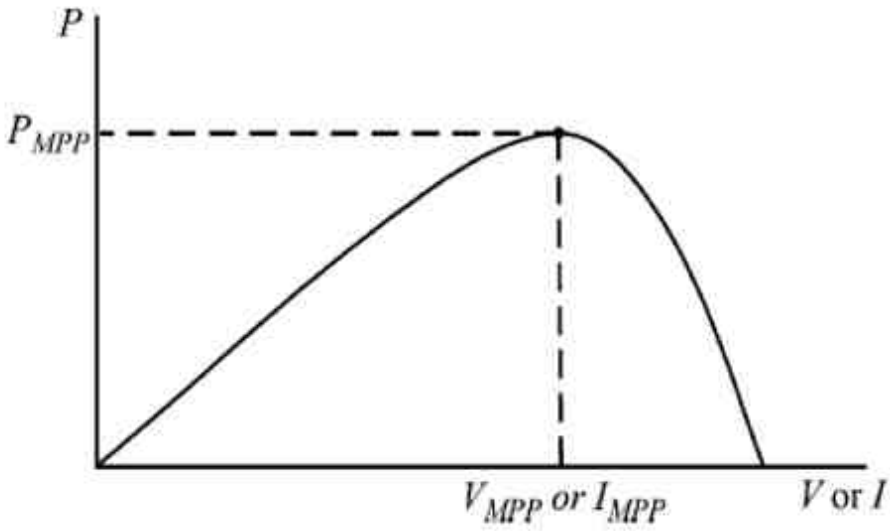


Fig. 4.9. Output power characteristic curve of solar panel

Figure 4.9 shows the output power characteristic curve of solar panel. It can be seen that solar panel has and only has one maximum power point in the possible operating range under a certain temperature and illumination intensity. The voltage or current corresponding to the MPP is called voltage at MPP $V_{mpp}$ or current at MPP $I_{mpp}$. Thus, the MPPT control method for solar system is to search for the MPP and maintain the maximum power at the output end. The MPPT controller monitor the output power from solar array and keep the maximum output power by using scientific algorithm. These effects can be analyzed based on principle from circuit perspective, which can be simulated in Figure 4.10. The load power of this linear circuit is obtained as follow:

$$P_{R_0} = I^2 R_0 = (\frac{V_i}{R_i + R_0})^2 R_0 \tag{4.8}$$

Take the first-order derivative on Ro, and then get,

$$\frac{dP_{R_0}}{dR_{R_0}} = V_i^2 \frac{R_i - R_0}{(R_i + R_0)^3} \tag{4.9}$$

From the formula (4-9), it is known that its first-order derivative is zero only when $R_o$ equals to $R_i$, so that load power has maximum value. Which means the power supply can apply the maximum power on the load when the internal resistance of power source is equal to the load resistance. Although, the output power of solar panel has strong non-linearity, it can be considered as linear circuit by approximation in a very short period of time. Therefore, the key point of solar MPPT under different temperature and illuminations is to regulate its load impedance close to the inner impedance of solar panel.

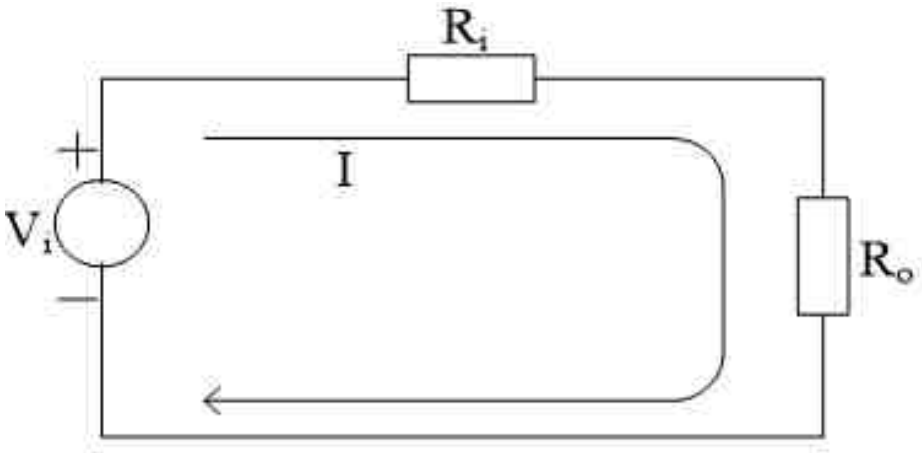


Fig. 4.10. Schematic diagram of a Linear Circuit

The operation schematic diagram of solar panel is depicted in Figure 4.11. The characteristic I-V curves are also demonstrated in the figure. Because of the existence of certain resistor, the linear part is the characteristic I-V curve of load, and the three intersections with characteristic curves of solar panel are operation point of PV. Hence, the actual optimized operation point should be satisfied with the features of both solar panel and load. When the operation point is not located at the MPP, PV and load must be in a state of mismatch. For example, as can be seen in the following figure, the operation point of PV is A when solar radiation is $1000W/m^2$. And then the solar radiation reduces to $800W/m^2$, which means the characteristic curves of solar panel changes from curve 1 to curve 2, and operation point is point B if there is no tuning done on the slope of straight line which indicates the load

value. In order to track the real MPP point C, the load size of the system should be adjusted and equals to the internal resistance of solar panel. In the Figure 4.12, the MPP can be captured by tuning the controller and regulating the converter[3]. Thus, the solar MPPT is achieved through adjusting load resistance as close as possible to internal resistance of power source[3].

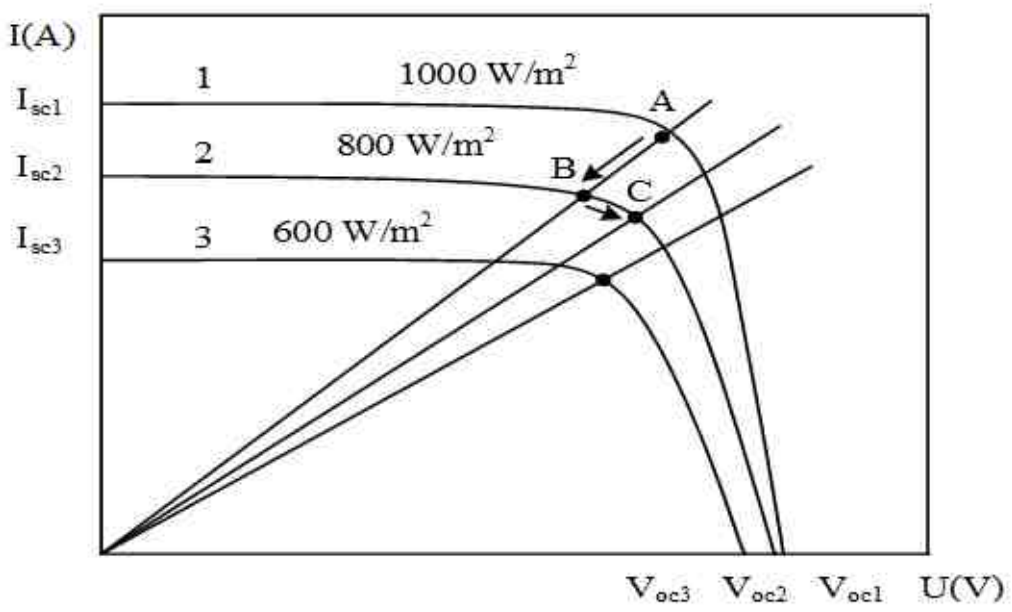


Fig. 4.11. Operation schematic diagram of solar panel

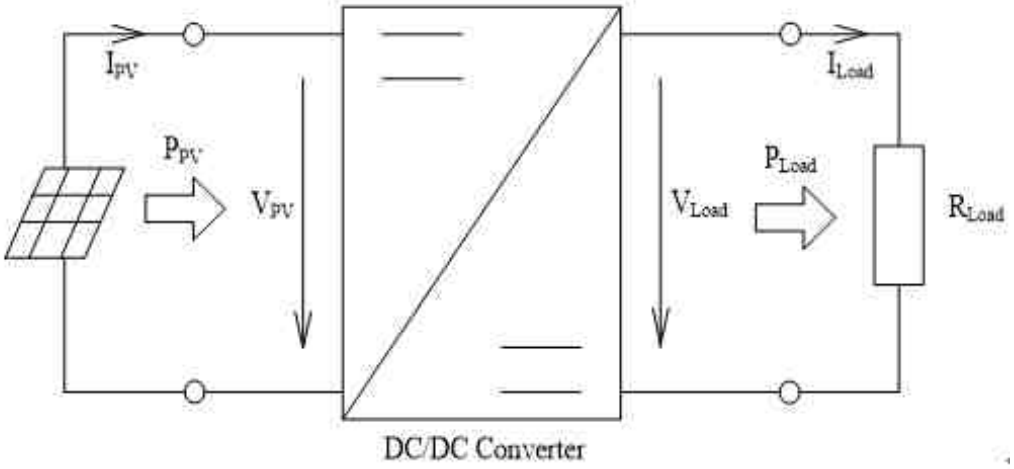


Fig. 4.12. Basic diagram of solar MPPT controller

### 4.2.1 Perturb and Observe Control

It is similar with P&O method used in the wind energy system. P&O algorithm in the solar system is also applied a positive or negative perturbation on the output voltage, output current or duty cycle in the system, and then the updated output power can be obtained and compared to verify whether the current operation point is MPP. Figure 4.13 demonstrates the algorithm of solar P&O control method[3]. Table 4.1 also illustrates the implementation of P&O strategy for solar system[1].

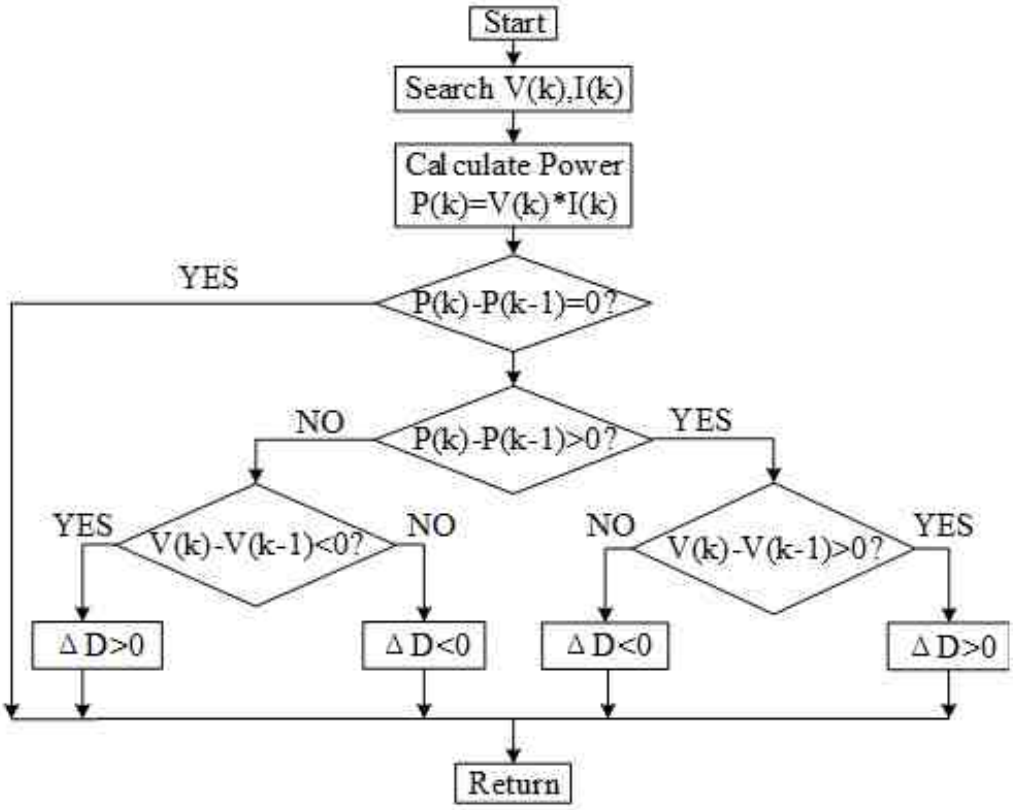


Fig. 4.13. Flow chart of solar MPPT algorithm

From the Figure 4.13, it is assumed that output power of solar array and its working voltage at moment k-1 is P(k-1) and V(k-1). When the time come to moment k, the output power of solar array and its working voltage changes to P(k) and V(k), the MPPT control for solar system can also be categorized into four circumstances[1]:

1. $P(k-1) < P(k)$ and $V(k-1) < V(k)$, the output power and the operating voltage at k moment is larger than those of k-1 moment, so the operating point is at the left side of MPP and it is approaching the MPP because $V(k-1) < V(k)$[1]. This causes that the next perturbation applied on the duty cycle become positive and continue increase the output voltage of PV[1].

2. $P(k-1) > P(k)$ and $V(k-1) > V(k)$, the output power and operating voltage at k moment is less than those of k-1 moment, so the operating point is at the left side of MPP and it is also away from MPP due to $V(k-1) > V(k)$[1]. This causes that the next perturbation of duty cycle become positive and increase the output voltage of PV to capture the MPP[1].

3. $P(k-1) > P(k)$ and $V(k-1) < V(k)$, the output power at k-1 moment is larger than that of k moment, so the operating point is at the right side of MPP[1]. $V(k-1) < V(k)$ means that the output voltage of solar panel is increasing, which means output power is decreasing with the increment of solar output voltage[1]. This causes that the next perturbation of duty cycle become negative and decrease the solar output voltage[1].

4. $P(k-1) < P(k)$ and $V(k-1) > V(k)$, the output power at k moment is larger than that of k-1 moment, so the operating point is at the right side of MPP[1]. $V(k-1) > V(k)$ means that the change in output voltage decreases, so now the output power is increasing with the decrement of output voltage[1]. This causes that the next perturbation to become negative and continue decrease the output voltage of solar panel to track the MPP[1].

Table 4.1 P&O Algorithm in Solar System

| *Original Perturbation* | *Change in Power* | *Next Perturbation* |
|---|---|---|
| Positive | Decrease | Negative |
| Positive | Decrease | Negative |
| Negative | Increase | Negative |
| Negative | Decrease | Positive |

### 4.2.2 Sliding Mode Extremum Seeking Control

In this work, a two-stage method is proposed by using cascaded BOOST converters due to its high conversion ratios[2]. However, the cascaded configuration has some inherent drawbacks regarding on the controller design and system dynamic stability, which can be seen with the impedance ratio criteria by R.D. Middlebrooks [2],[50]. So this section focuses on the solar MPPT controller based on the sliding mode approach from the following three parts[2].

1. PV Impedance Matching and Sliding Mode Controller

In MPPT searches the operating voltage close to the maximum power point (MPP) in various environmental conditions[2]. As it is known, the electrical circuit of power converters can be represented and analyzed by using the ideal canonical elements, such as LFR which belongs to a range of circuits named POPI (power input equals to the power output)[2],[52],[53]. Thus, the input port can absorb the power and then transfer it to the output without losses [2],[54], [55]. The architecture of PV system connecting to BOOST-BOOST converter with a DC load is illustrated in Figure 4-14[2]. The output power can be obtained by the following function of the LFR conductance $g_1$=$\frac{1}{r_1}$[2]:

$$P_o = g_1 V_P^2 \tag{4.10}$$

The I–V curve of PV module and the LFR steady-state load line are also depicted in Figure 4-15[2]. Note that the intersection of them is the working point of PV panel, so the conductance (slope of LFR load line) can be tuned to search the optimal operating point of solar system through modifying g conductance value [2],[54],[55]. The following two sliding mode control surfaces are also set to behave as switches for each BOOST converters[2]:

$$s_1(x) = g_1 V_p - i_{L_1} \tag{4.11}$$

$$s_2(x) = g_2 V_{C_1} - i_{L_2} \tag{4.12}$$

where $g_1$ is conductance of PV panel, $V_p$ is output voltage of PV cell[2], $i_{L_1}$ is output current of the first stage, $g_2$ is the conductance of second BOOST converter[2], $V_{C_1}$ is the capacitance of intermediate capacitor between converters, and $i_{L_2}$ is the output current of the system[2].

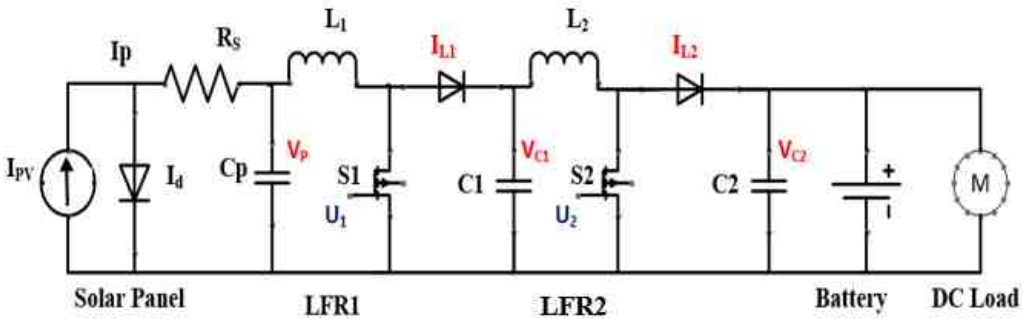


Fig. 4.14. Schematic diagram of two cascaded BOOST converters based on LFRs

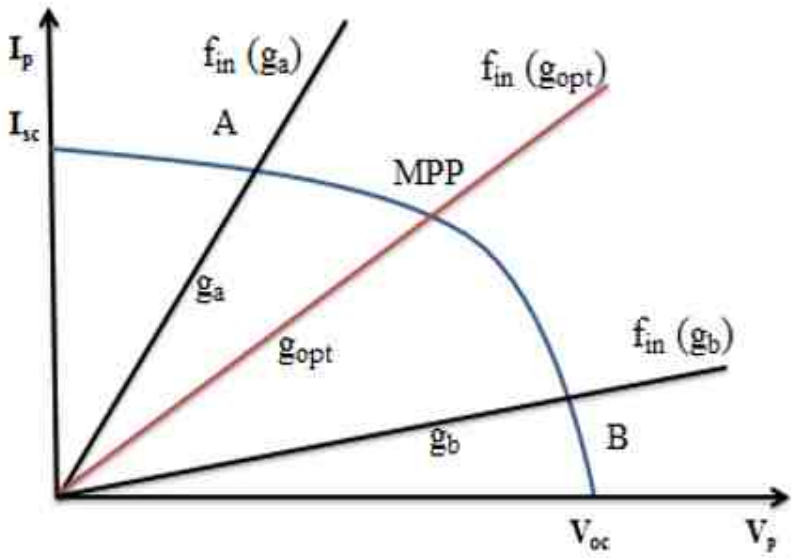


Fig. 4.15. PV panel operating points for impedance matching between the PV generator and the LFR

2. Maximum Power Point Tracking Technique

The purpose of MPPT in PV is to obtain the best operating point that controls the PV around the MPP in spite of the temperature, insolation and load variation[2]. There are many tracking methods applied to different types of DC-DC converters [2],[56]-[59]. The Extremum Seeking Control (ESC) is one of the popular MPPT algorithms which can control the PV system to approach the MPP by increasing or decreasing a suitable control signal, its block diagram is shown in Figure 4.16[2]. The input of the MPPT controller sets the output voltage and current of the PV panel, and is passed through a low pass filter, the power variation, dP, is calculated as the input signal of hysteretic comparator (HC)[2]. HC can generate a binary signal which reflects whether dP is positive or negative. This key information is sent to a logic circuit that can determine the next direction of maximum power point tracking control signal maintained or changed[2]. In the last stage, the control signal of searching direction is introduced to an integrator to get the conductance g1 of first stage BOOST converter [2],[54].

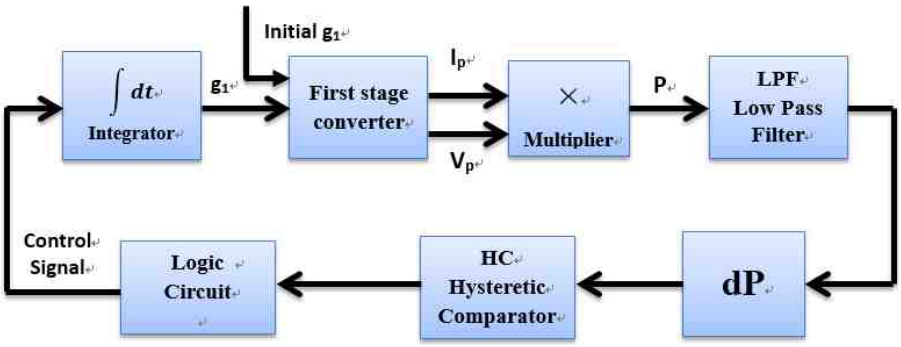


Fig. 4.16. PV MPPT scheme based on ESC

For the voltage control at the terminal of cascaded BOOST converters, a PI controller is established to generate $g_2$ as the conductance value of the second LFR[2]. So the terminal voltage is fixed to satisfy load requirement under different weather conditions[2]. However, actually the PI controller in this condition is just giving a limit of conductance $g_2$ value for MPPT, because the terminal voltage is clamped by the rear-end battery terminal voltage. And the solar MPPT can be accomplished when $g_2$ is in an appropriate range, but still has some power losses.

Table 4.2 Lookup table between solar radiation and $g_2$

| *Solar Radiation* $(W/m^2)$ | $g_2$ |
|---|---|
| 1400 | 0.180 |
| 1300 | 0.171 |
| 1200 | 0.160 |
| 1100 | 0.149 |
| 1000 | 0.137 |
| 900 | 0.125 |
| 800 | 0.113 |
| 700 | 0.100 |
| 600 | 0.090 |

In the proposed third configuration of hybrid renewable energy system, $g_2$ value can be obtained from a fitting function, which depends on the variations of solar radiation. The main reason regarding that is to improve the tracking efficiency with respect to the previous PI method. Due to the utilization of DC constant power load, every accurate $g_2$ value is corresponding to one specific solar radiation. Thus, a lookup table of $g_2$ and solar radiation is built in table 4.2. Therefore, the fitting function can be obtained by using the curving fitting toolbox in Matlab. The fitting curve which reflects the relationship in Table 4.2 is shown in Figure 4.17, where axis x indicates the solar radiation and axis y indicates the $g_2$ value.

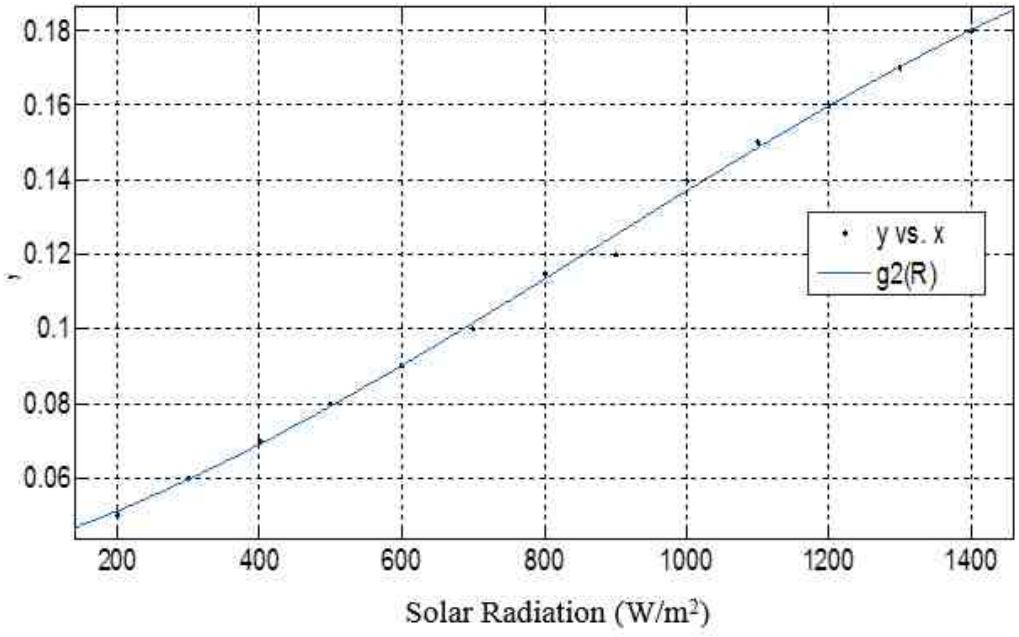


Fig. 4.17. Fitting curve of solar radiation and $g_2$ value

3. Mathematical Modeling

For the switched model of the cascaded BOOST converter, the system dynamic behavior can be described from the following four differential equations according to Figure 4.14 by using the Kirchhoff's voltage and current laws as formula (3-19)[2]. When the first stage or the second stage control command equals unity, it means

the switch $S_1$ or $S_2$ is closed; and a zero control command means switch $S_1$ or $S_2$ is open[2].

The two terminal sliding mode functions $s_1(x)$ and $s_2(x)$ is defined in (4-11) and (4-12)[2]. If the sliding surface s(x) is always kept at zero such that[2]:

$$s_1(x) = g_1 V_p - i_{L_1} = 0 \tag{4.13}$$

$$s_2(x) = g_2 V_{C_1} - i_{L_2} = 0 \tag{4.14}$$

To continue the SMC design, the time derivative of the two terminal sliding mode surfaces along (4-13) and (4-14) can be obtained as follows[2]:

$$\dot{s}_1(x) = g_1 \frac{dV_p}{dt} + V_p \frac{dg_1}{dt} - \frac{di_{L_1}}{dt} = 0 \tag{4.15}$$

$$\dot{s}_2(x) = g_2 \frac{dV_{C_1}}{dt} - \frac{di_{L_2}}{dt} = 0 \tag{4.16}$$

In order to achieve the fast convergence of the sliding surfaces and drive the trajectories of the system are evolving on the switching manifolds, the control signals $u_1$ and $u_2$ can be represented from the full-order switched model and equations (4-13) to (4-16)[2]. Under sliding mode conditions, the control laws which describe the dynamic behavior of the system that is restricted to the two switching surfaces can be obtained as follows[2]:

$$u_1 = 1 - \frac{V_d}{V_{C_1}} - \frac{1}{V_{C_1}} V_p L_1 \left(\frac{m_2(m_3 V_c - \epsilon)}{\tau_1}\right) \tag{4.17}$$

$$u_2 = 1 - \frac{1}{V_{dc}}\left(V_{C_1} + \frac{g_2 L_2}{C_1}\left(g_2 V_{C_1} + \frac{g_1 V_p}{V_{C_1}}\left(V_p - \frac{g_1 L_1}{C_p}(i_p - g_1 V_p)\right)\right)\right) \tag{4.18}$$

where $m_2$ and $m_3$ are constants, $\epsilon$ is the next direction of maximum power tracking and $\tau_1$ is a time constant[2]. It should be noted that the control variables u1

and $u_2$ are PWM signals which must be bounded between minimum 0 and maximum 1 [2],[54], i.e.:

$$0 \leq u_1 \leq 1 \; and \; 0 \leq u_2 \leq 1 \tag{4.19}$$

## 4.3 Supervisory Control Strategy for Hybrid Power System

In a DC-system fed by multiple converters on a common bus, current must be shared among all sources according to their available power while ensuring the stability of the bus voltage[3]. According to the existence of battery, there are two supervisory control strategies is established and introduced in this section[3]. Therefore, the supervisory control is designed to set the voltage of DC bus and manage the power among sources and storage devices[3].

1. With Storage Device

In the first three types of proposed configurations of combined DC power systems, which considering the wind or solar and a storage system feeding a common load, several contingencies may occur which are listed in Table 4.3[3]. Since the battery storage is directly connected to the DC bus, the supervisory controller can charge or discharge it by setting the DC bus voltage slightly higher or lower than the battery terminal voltage[3]. To charge the battery, the converter of another source such as wind or solar must be controlled as a voltage source while the other is controlled as a current source[3]. This decision is based on the amount of power each source is instantaneously generating[3]. When the battery is fully charged and is required to feed the load, the battery maintains the voltage while other converters are controlled as a current source[3]. A smooth transition from voltage to current source by the use of local controllers results in high performance and efficient controls [3],[60-61]. The net power that battery needs to provide,$\Delta P$ can be obtained from the renewable energy balance equation deficit as follows[3]:

$$\Delta P = P_s + P_w - P_{Load} \tag{4.20}$$

where $P_s$ is the output power of solar, $P_w$ is the output power of wind, $P_{load}$ is the power demand from load. The supervision mode is shown in Table 4-3 which can be stated as follow[3]: In mode 1, if $\Delta P$ is greater than or equal to zero and SOC is not higher than 95%, then the energy source should feed and the net power is used to charge the battery[3]; In mode 2, when $\Delta P$ is greater than or equal to zero and SOC is higher than 95%, then the energy source feeds load and floating charge the battery to maintain the SOC, and a dummy load is also required to consume the surplus power[2],[3]; In the worst case which is mode 3, in case $\Delta P$ is lower than or equal to zero and SOC is lower than 40%, the load is disconnected to make sure that all the source power are used to charge the battery[2],[3]; In mode 4, i.e.$\Delta P$ is less than or equal to zero and SOC is higher than 40%, the load can be reconnected and the available energy both from power sources and battery are used to satisfy the load[3]. In extreme weather conditions, a dump load is required to consume the extra power generated form the sources[3], and some shut-off measures is utilized to assure the safety of the whole operation of system[3].

Table 4.3 Supervisory Control Contingencies with battery

| *Mode* | *Condition* | *Control Effect* |
|---|---|---|
| 1 | $\Delta P \geq 0$,$0 \leq SOC \leq 95\%$ | Feeding Load and charge Battery |
| 2 | $\Delta P \geq 0$, $SOC > 95\%$ | Feeding Load and battery(Surplus power through a dummy load) |
| 3 | $\Delta P \leq 0$, $SOC < 40\%$ | Charge battery and off load |
| 4 | $\Delta P \leq 0$, $SOC > 40\%$ | Feeding load and battery discharge to the load |

2. Without Storage Device

In the fourth type of the proposed configurations of combined DC power systems, the DC system fed by multiple converters on a common DC bus without application of battery, power must be shared among the solar source and the wind source according to their available output power[1]. Therefore, a supervisory controller is designed to track the maximum power generated from the two sources and manage the power to satisfy the load requirement[1]. It is noted that this strategy only considers obtaining the maximum power delivering to the load and not maintaining a constant power to the load[1]. The DC bus voltage regulating and an energy storage charge or discharge procedure is discussed in the future works[1]. In order to accomplish the supervisory control strategy, the energy balance equation can be also obtained as formula (4-20), the only difference with condition of existence of battery is that $\Delta P$ is the net power of the system, $P_s$ is the output power of solar, $P_w$ is the output power of wind, $P_{Load}$ is the power demand from load[1]. The supervision modes can be clarified into two types (listed in Table 4.4[1]). It can be categorized as follows:

(a) If $\Delta P \leq 0$, means that the power generation unit cannot satisfy the load[1]. In this situation, both solar and wind power supplies must work in MPPT mode to generate the maximum power under different weather conditions to reduce the power shortage[1].

(b) If $\Delta P > 0$, means that the power generation system can satisfy the load with surplus energy[1]. In this situation, one source can be selected to operate in MPPT mode and the other source is set in power tracking mode by means of a PI current controller. The current reference value is determined as follows[1]:

$$I_{ref} = \frac{P_{Load} - P_{MPPT}}{V_{Load}} \tag{4.21}$$

where $P_{MPPT}$ is the output power of the source which operates in MPPT mode, and $V_{Load}$ is the output voltage of load.

Table 4.4 Supervisory Control Contingencies without battery

| *Mode* | *Condition* | *Control Action* |
|---|---|---|
| 1 | $\Delta P \leq 0$ | Both in MPPT Control Mode |
| 2 | $\Delta P > 0$ | Larger Power in MPPT Mode Smaller Power in Power Tracking Mode) |

# 5. SIMULATION RESULTS

In order to verify the previous applied theories[2], all types of the proposed DC power systems are simulated in Matlab/Simulink. Chapter 5 represents the simulation results regarding the MPPT control methods and supervisory control strategies in every kinds of previous introduced combined new energy systems. Simulation results show accurate operation of the supervisory controller and functionality of the maximum power point tracking algorithm for solar and wind power sources[3].

## 5.1 Wind Maximum Power Point Tracking Control Effect

This section shows two MPPT control performances in wind system, which are P&O and sliding mode extremum seeking control. The tracking effects of these methods are also compared[4].

### 5.1.1 Perturb and Observe Control

For the load is a 30Ω load that is a linear load. Simulations of wind P&O MPPT profile with wind speed variation from 4m/s to 12m/s are illustrated in Figure 5.1 and Figure 5.2[1]. They depict the wind maximum power point tracking effects when the wind speed changes from 4m/s to 6m/s to 8m/s to 6m/s to 4m/s, and 8m/s to 10m/s to 12m/s to 10m/s to 8m/s respectively[1]. The figures also show the output power generated directly from wind turbine and the actual power captured to the load[1].

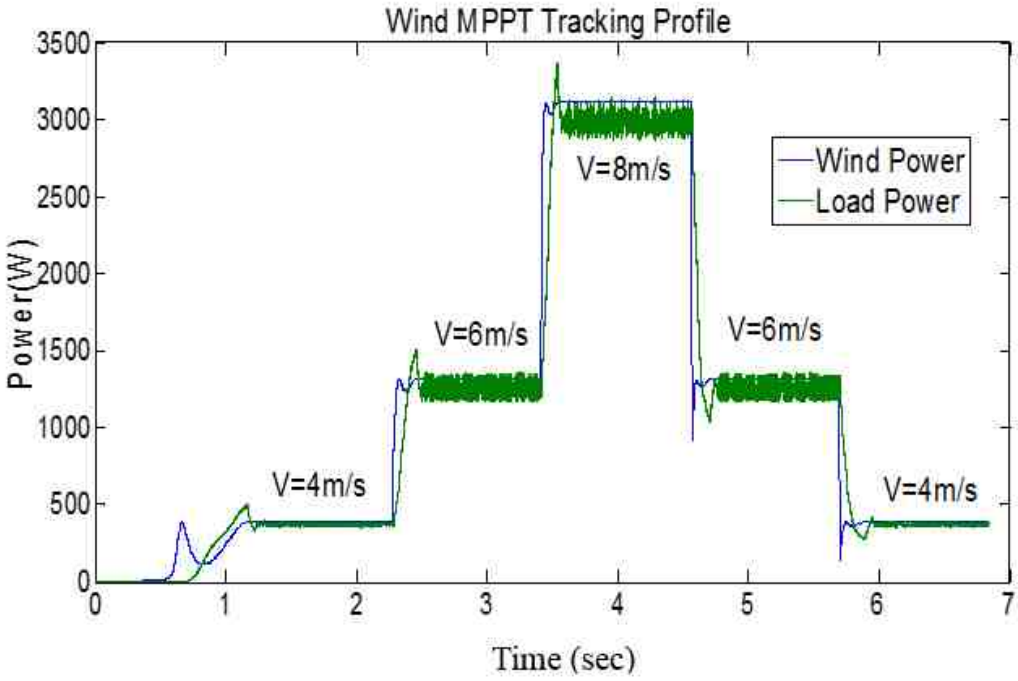


Fig. 5.1. Wind MPPT tracking profile to step change in the wind speed from 4m/s to 6m/s to 8m/s to 6m/s to 4m/s

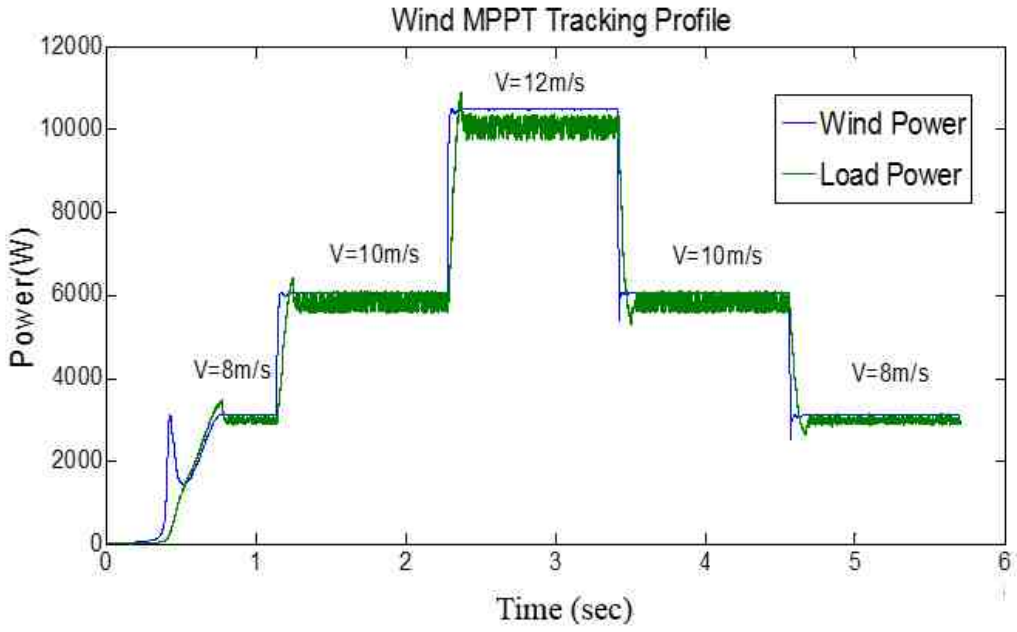


Fig. 5.2. Wind MPPT tracking profile to step change in the wind speed from 8m/s to 10m/s to 12m/s to 10m/s to 8m/s

Similarly, the wind MPPT tracking efficiency has also been evaluated in the Table 5.1[1]. The table lists the wind power, load power and power loss to the step change of wind speed from 4m/s to 12m/s[1]. The calculation results show that the tracking efficiencies are all around 96% and that the intended target powers were achieved[1].

Table 5.1 MPPT Tracking Efficiency in Wind System

| $WindSpeed$ | $WindPower$ | $LoadPower$ | $TrackingEfficiency$ |
|---|---|---|---|
| 4m/s | 390W | 370W | 94.9% |
| 6m/s | 1310W | 1260W | 96.2% |
| 8m/s | 3110W | 3000W | 96.8% |
| 10m/s | 6080W | 5850W | 96.2% |
| 12m/s | 10500W | 10050W | 95.7% |

When the load is a DC constant power load (2.5kw)[3]. Simulations of wind MPPT profile for a DC constant power load (2.5kw) and battery with wind speed variations are illustrated in Figure 5.3 and 5.4[3]. Figure. 5.3 (a) depicts the MPPT tracking profile and the load power conditions when the wind speed changes from 8m/s to 10m/s. Figure.5.3 (b) shows the power coefficient $C_p$ is keeping the maximum value 0.48. Figure.5.4 (a) illustrates the MPPT tracking profile and the load power conditions with the variations of wind speed from 12m/s to 10m/s. Figure.5.4 (b) also demonstrates the power coefficient $C_p$ reaching the maximum value 0.48.

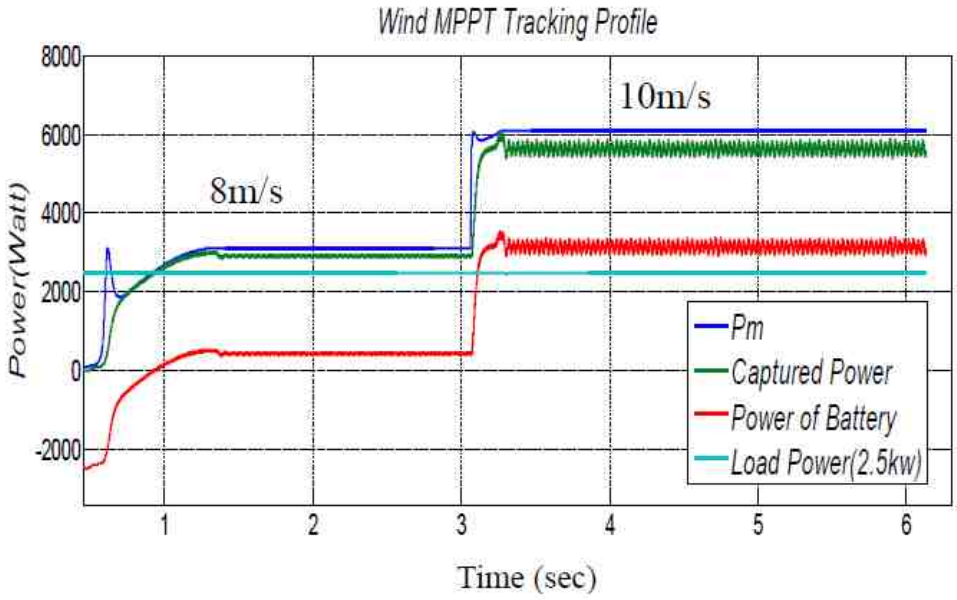


(a) Wind MPPT tracking effect

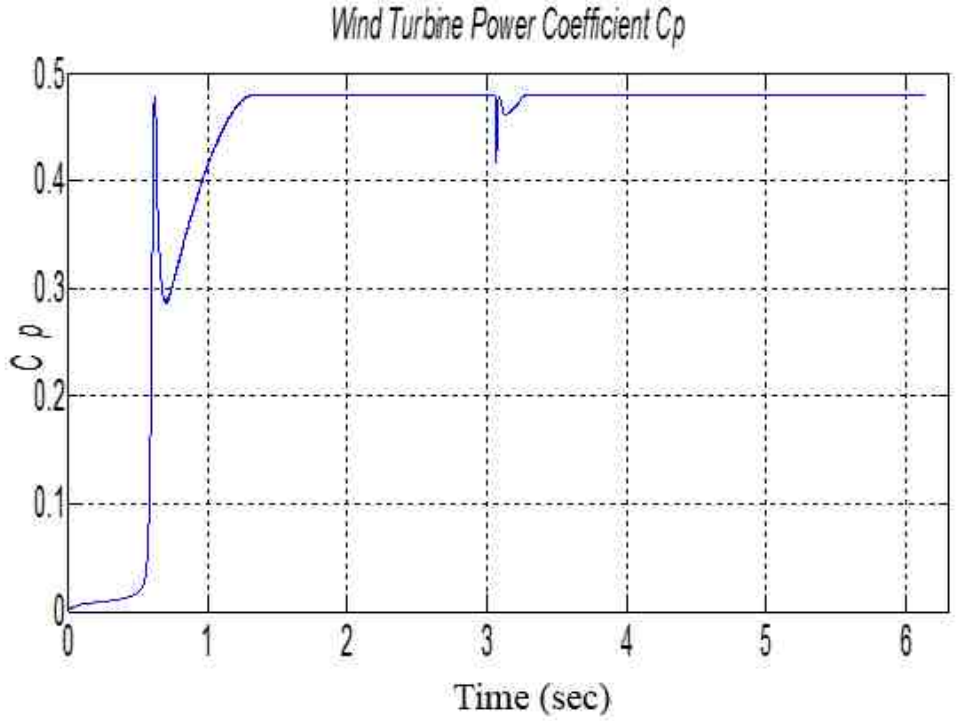


(b) Wind power conversion coefficient

Fig. 5.3. Wind MPPT P&O tracking profile to step change in wind speed from 8m/s to 10m/s with CPL (2.5kw)

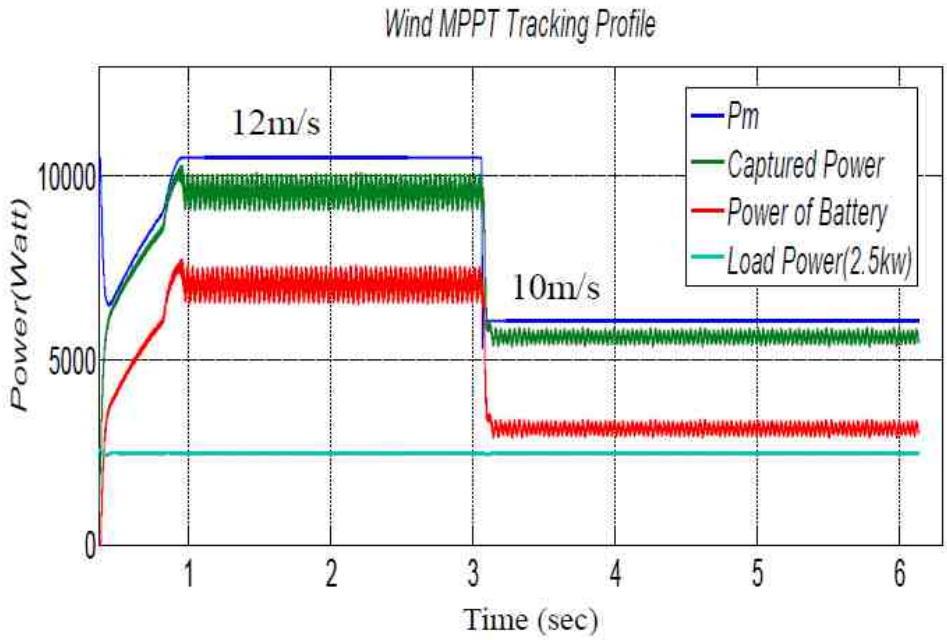


(a) Wind MPPT tracking effect

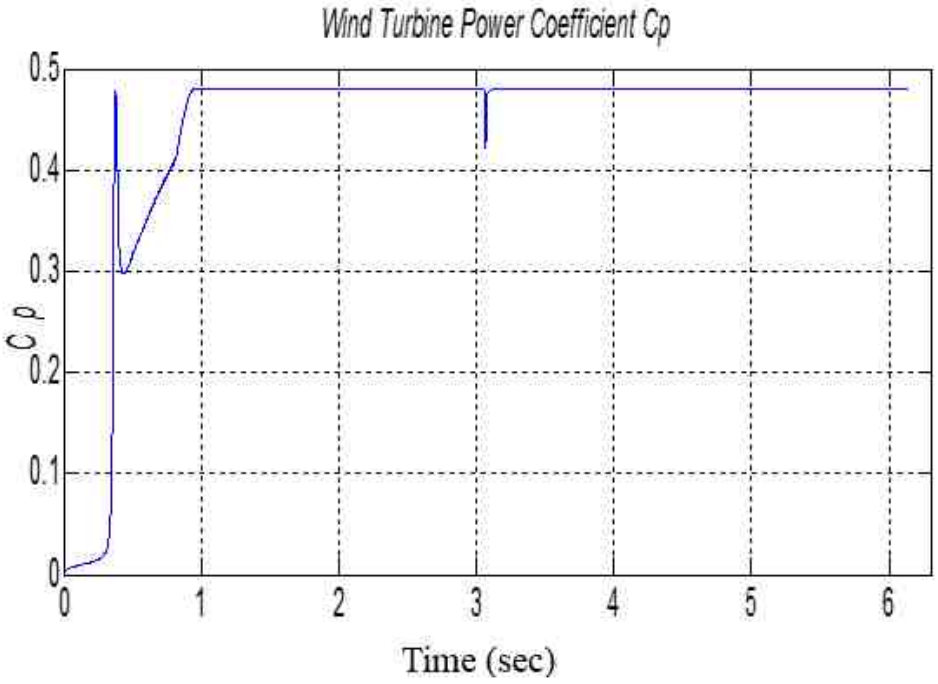


(b) Wind power conversion coefficient

Fig. 5.4. Wind MPPT P&O tracking profile to step change in wind speed from 10m/s to 8m/s with CPL (2.5kw)

### 5.1.2 Sliding Mode Extremum Seeking Control

This section demonstrates some simulation performances of sliding mode extremum seeking control with DC constant power load[4]. The MPPT tracking profile, wind power coefficient and tuning signal for PWM under the wind speed changing from 7m/s to 8m/s to 9m/s to 10m/s are illustrated in Figure 5.5[4]. Figure 5.6 depicts the MPPT tracking profile, the power and coefficient tuning signal for PWM with the variations of wind speed from 10m/s to 9m/s to 8m/s to 7m/s. As represented in the figures, the $C_p$ value always remains at the maximum level 0.48[4].

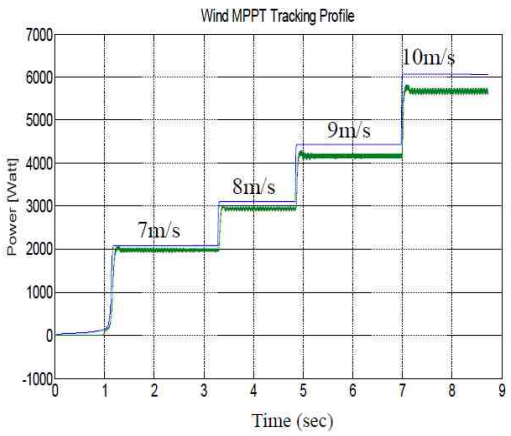


(a) MPPT tracking profile

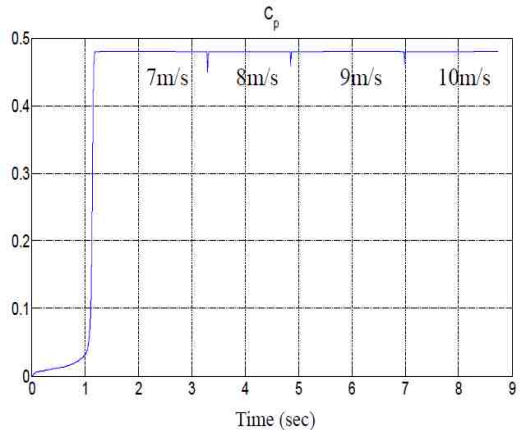


(b) Wind power coefficient

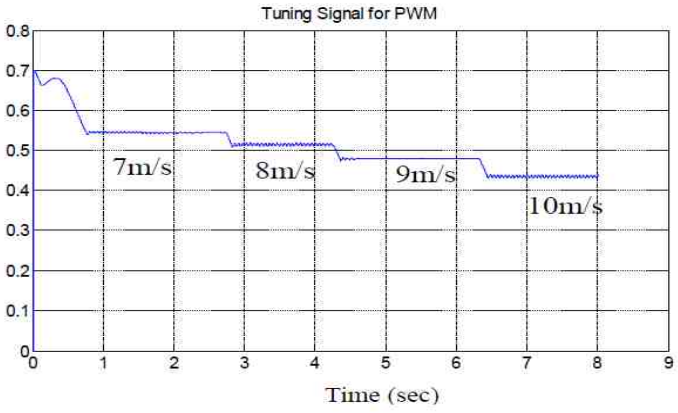


(c) PWM signal for DC/DC converter

Fig. 5.5. System SM-ESC MPPT dynamic response when wind speed changing from 7m/s to 8m/s to 9m/s to 10m/s

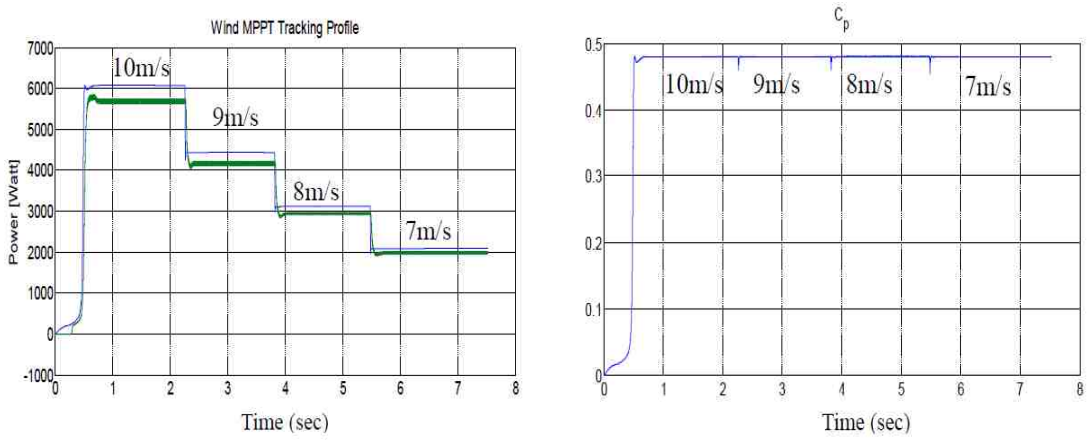


(a) MPPT tracking profile

(b) Wind power coefficient

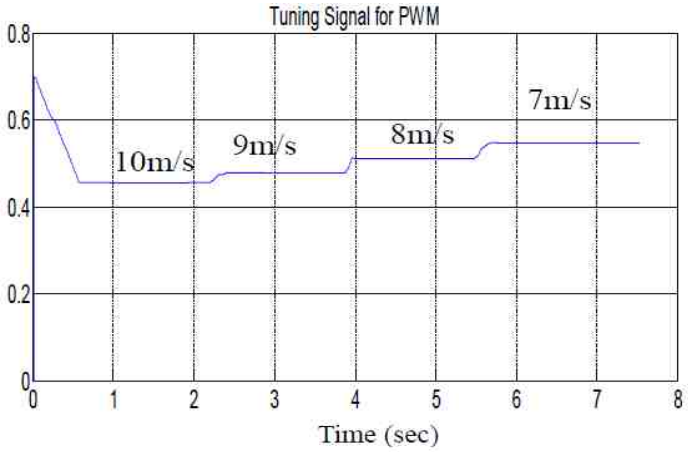


(c) PWM signal for DC/DC converter

Fig. 5.6. System SM-ESC MPPT dynamic response when wind speed changing from 10m/s to 9m/s to 8m/s to 7m/s

The whole system with SM-ESC MPPT controller is simulated in Matlab/Simulink[2],[4]. The functionality of the proposed system has also been verified in the following figures, the sample time of the simulations has been set to 1e-6s[2],[4]. Regarding the lead-acid battery used in the system, the terminal voltage of battery is 229V when SOC is 30% and the terminal voltage is around 245V when the SOC over 95%. Thus the DC bus voltage should show that it can be controlled to a certain extent for charging or discharging the battery[4]. Figure 5.7 and Figure 5.8 represent the system responses

under a step change of the DC load voltage from 220V to 255V and 255V to 220V to show the feasibility of the control system[2],[4]. It can be observed that increasing or decreasing the DC bus voltage in appropriate range does not affect to capture the maximum power of the wind turbine in the proposed control strategy[2],[4].

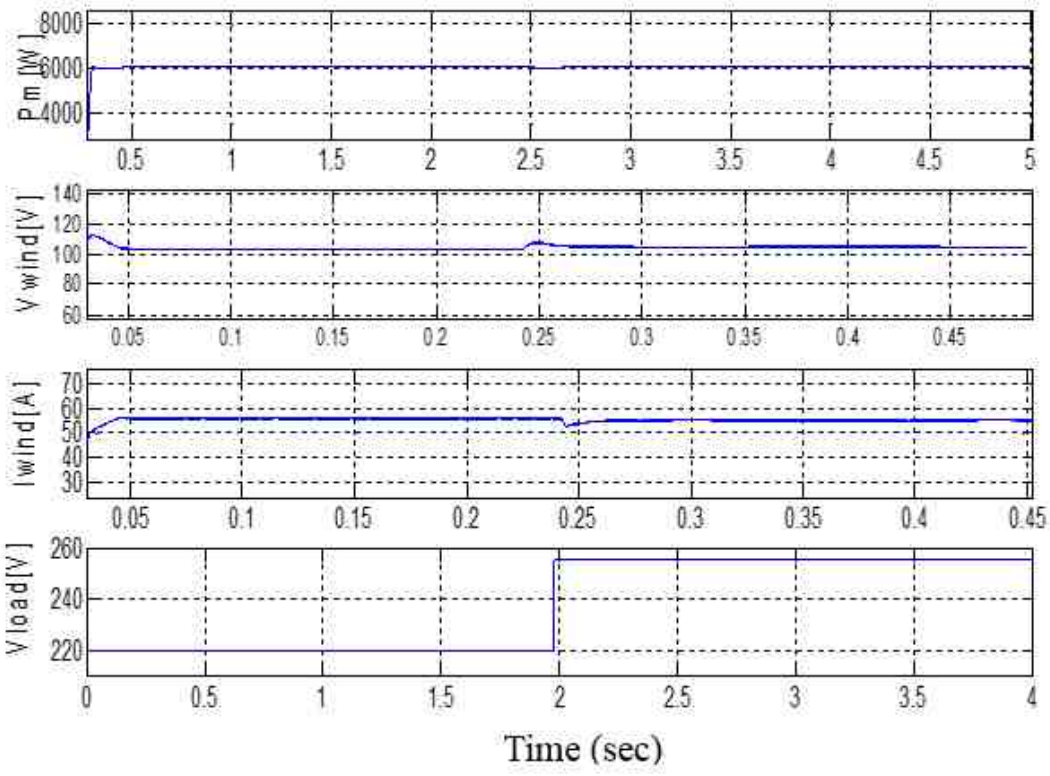


Fig. 5.7. Waveforms of the wind power, input voltage and current during the load voltage changes from 220V to 255V

In addition, the wind MPPT control performances associated with load conditions of 300 Ah battery of 80% of SOC and CPL are shown in Figure 5.9 and Figure 5.10[4]. The CPL changes from 5kW to 2kW in Figure 5.9 and changes from 4kW to 6kW in Figure 5.10. Both control effects represent the desired results[4].

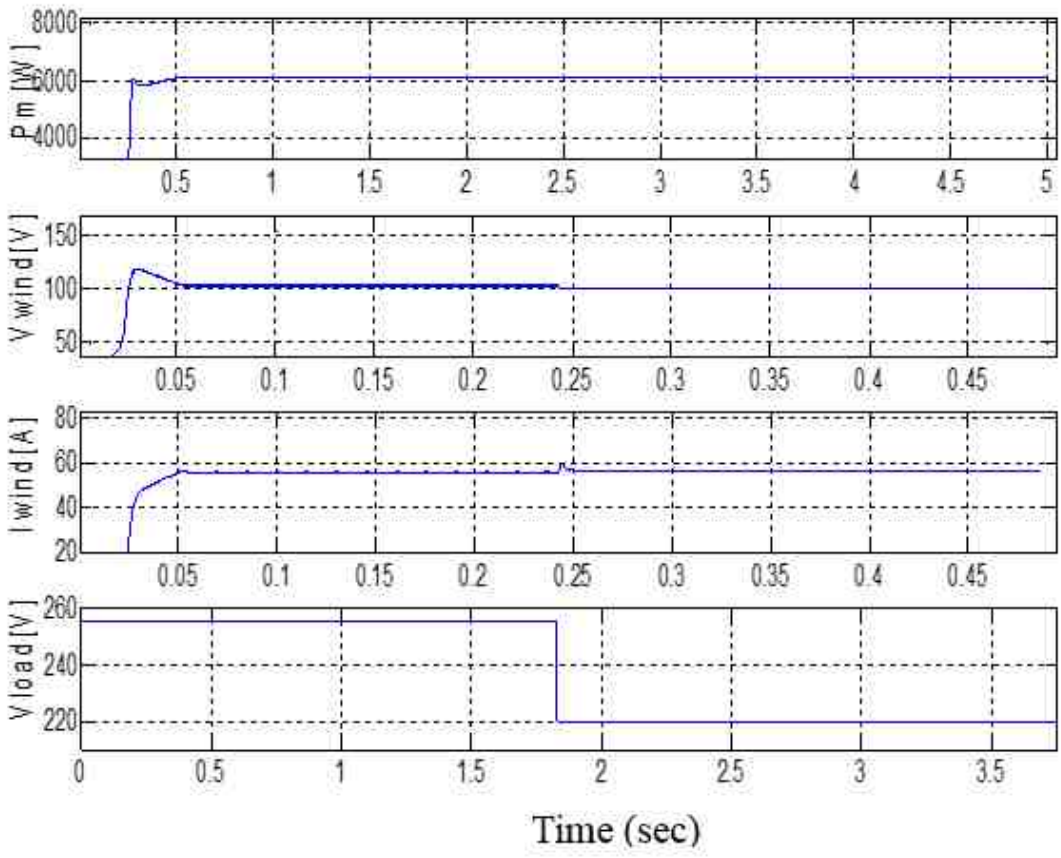


Fig. 5.8. Waveforms of the wind power, input voltage and current during the load voltage changes from 255V to 220V

In the beginning of Figure 5.9, CPL is 5kW and wind speed is 6m/s, there is not enough energy to supply the DC constant power load so it is necessary to discharge the battery and satisfy the CPL[4]. Then the wind speed increases to 8m/s, the total power generated from wind turbine is still smaller than 5kW, the gap power is still obtained from discharging of the battery[4]. When the CPL decreases to 2kW and the wind speed keeps at 8m/s, which means the total power given by the wind source is higher than load power requirement and the surplus power can be used to charge the battery[4]. Eventually, wind speed decreases to 6m/s, the battery need to be discharged again to maintain the 2kW DC constant power load[4].

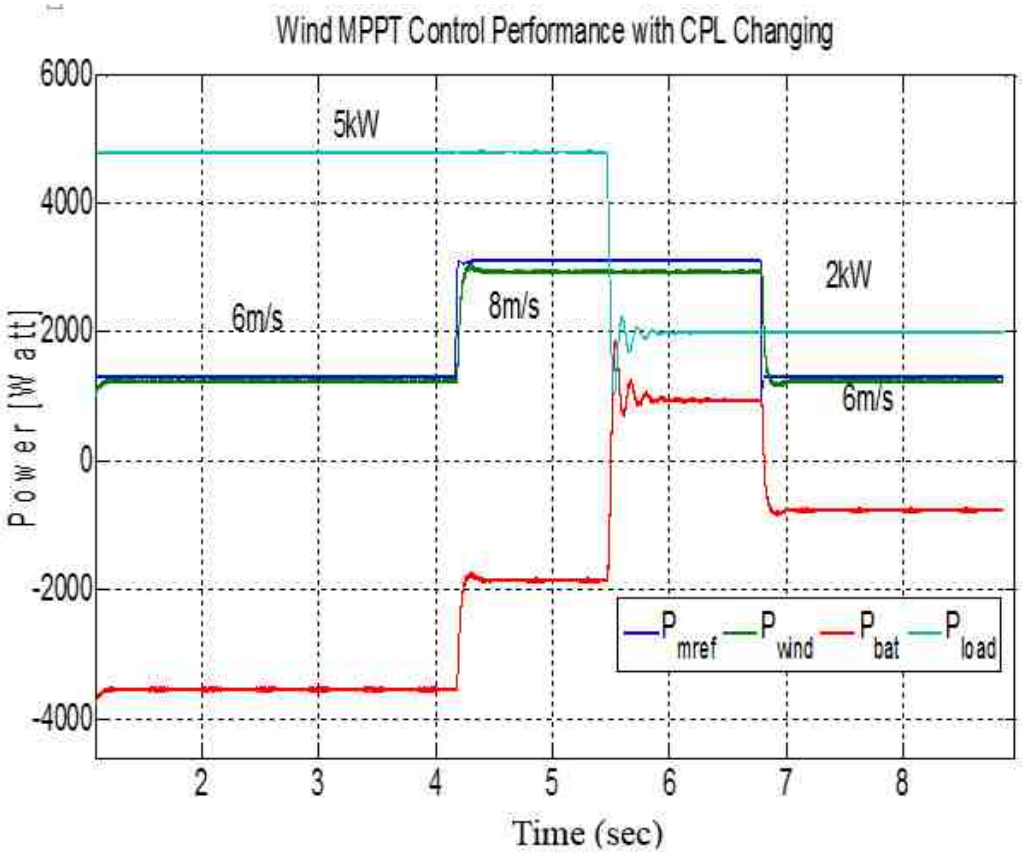


Fig. 5.9. Wind MPPT control performance with CPL changing from 5kW to 2kW

For the Figure 5.10, CPL is 4kW and wind speed is 10m/s, the produced energy can supply the DC constant power load totally, the surplus power should be fully used to charge the battery[4]. Then the wind speed decreases to 8m/s, the total power generated from wind turbine decreases to about 3kW, which is smaller than 4kW, and the battery is discharged to make up energy deficiency[4]. When there is a 2kW power increment of the CPL and the wind speed keeps at 8m/s, the same case as before which indicates that the battery continues to discharge and remain the load satisfaction[4]. At last, wind speed increases to 10m/s, the total power generated from wind system is nearly the same as 6kW of the constant power load[4]. Therefore, the battery is under floating charged status with the DC bus voltage setting around the terminal voltage of the battery, which can maintain its capacity without the power loss[4].

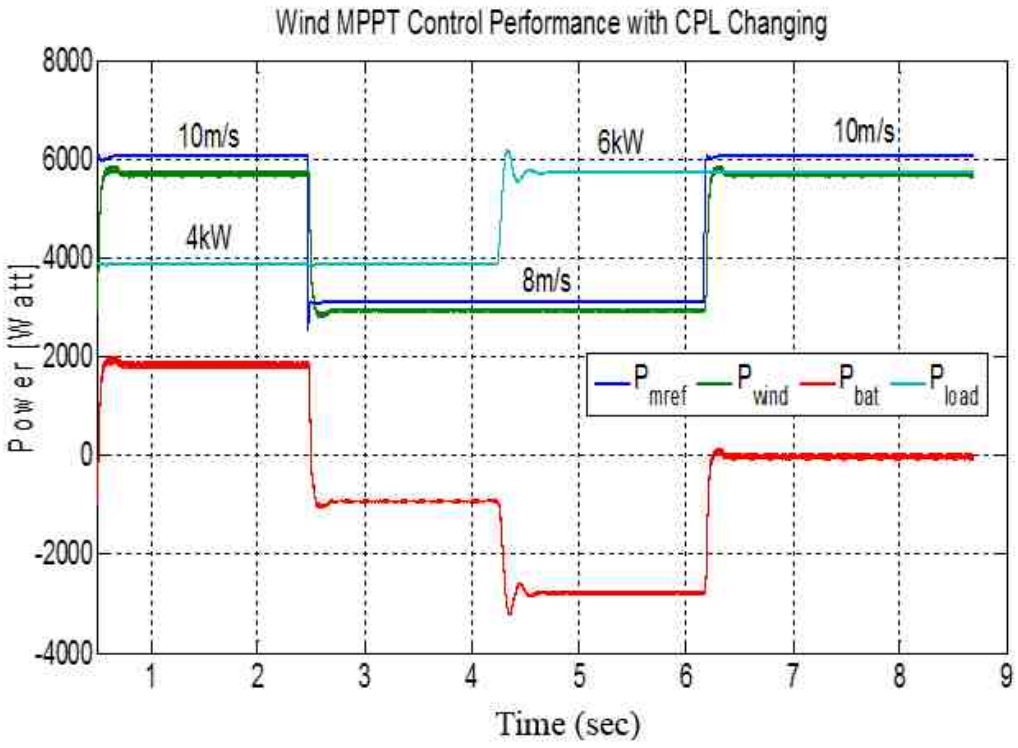


Fig. 5.10. Wind MPPT control performance with CPL changing from 2kW to 5kW

### 5.1.3 Comparisons

The maximum power point tracking dynamic response of P&O and SM-ESC algorithms with constant wind speed 8m/s are compared in Figure 5.11[4]. From the comparison results, the output power oscillations of SM-ESC method in wind system are found to be smaller than the P&O method applied in the system, and the wind MPP tracking speed under SM-ESC strategy is faster than the MPP tracking speed under P&O method[4]. This is because the SM-ESC has utilized the adaptive step size to accomplish the tracking and results in smaller vibration with respect to the traditional P&O method. The oscillation of P&O is about 200W, but only 50W of MS-ESC[4]. Thus, it can greatly enhance the capturing efficiency and has better regulation performance than P&O method[4].

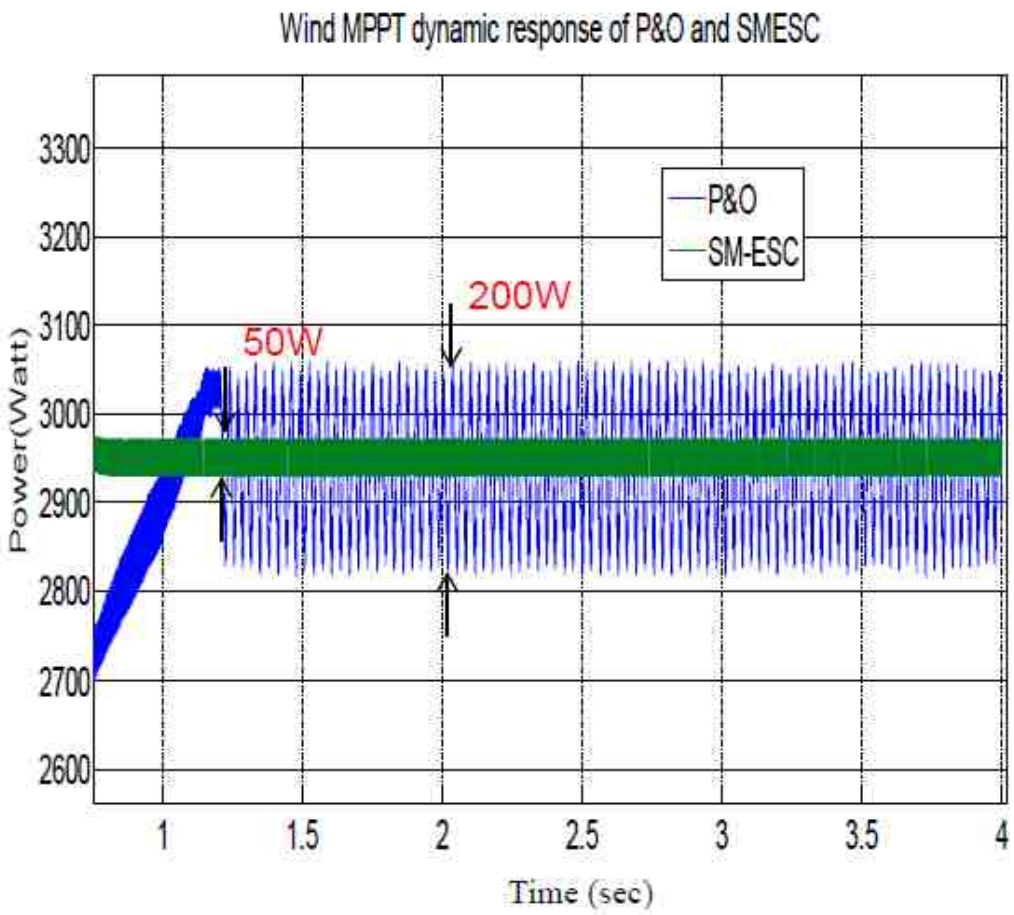


Fig. 5.11. Wind MPPT dynamic response of P&O and SM-ESC

## 5.2 Solar Maximum Power Point Tracking Control Effect

This section shows two MPPT control performances in solar system, which are perturb & observe and sliding mode extremum seeking control. The tracking effects of them are also compared.

### 5.2.1 Perturb and Observe Control

Similar with wind P&O control, the solar P&O control is also separated into linear load and non-linear load[1]. Simulation of PV P&O profile for a 30Ω load when the temperature is ($25°C$) has been shown in Figure 5.12[1]. Figure 5.12(a) depicts the PV current $I_{pv}$ is around 17.1 A under the standard weather condition $1000W/m^2$[1]. This shows the reach of maximum power point delivered from PV panel[1]. Figure 5.12(b) illustrates the variation of perturbation signal during the irradiance changing from $600W/m^2$ to $1000W/m^2$ and then come back to $600W/m^2$, which oscillates slightly around the best duty ratio when the radiation changes quickly[1]. As the figure shows, the maximum power points of PV model are approximately 1010W, 1400W and 1800W when the solar radiances are $600W/m^2$, $800W/m^2$ and $1000W/m^2$ respectively[1].

In order to evaluate the MPPT tracking efficiency for solar system, Table 5.2 demonstrates the power condition under different irradiance levels[1]. From the table, the output power generated from PV cells, the load power and the power loss are calculated individually[1]. The results show that the tracking efficiencies are more than 97% generally under the step change from $600W/m^2$ to $1000W/m^2$ to $600W/m^2$.

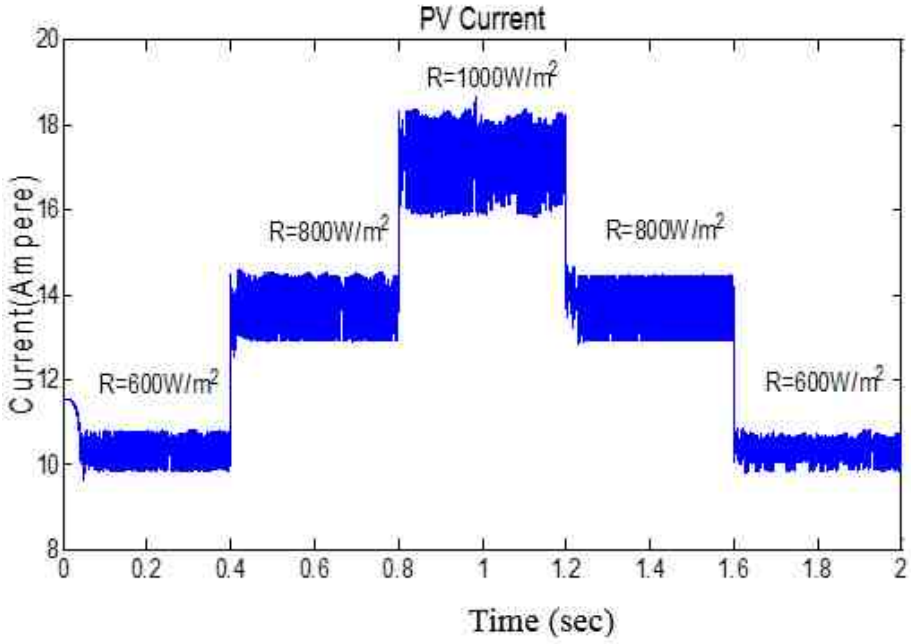


(a) PV current profile

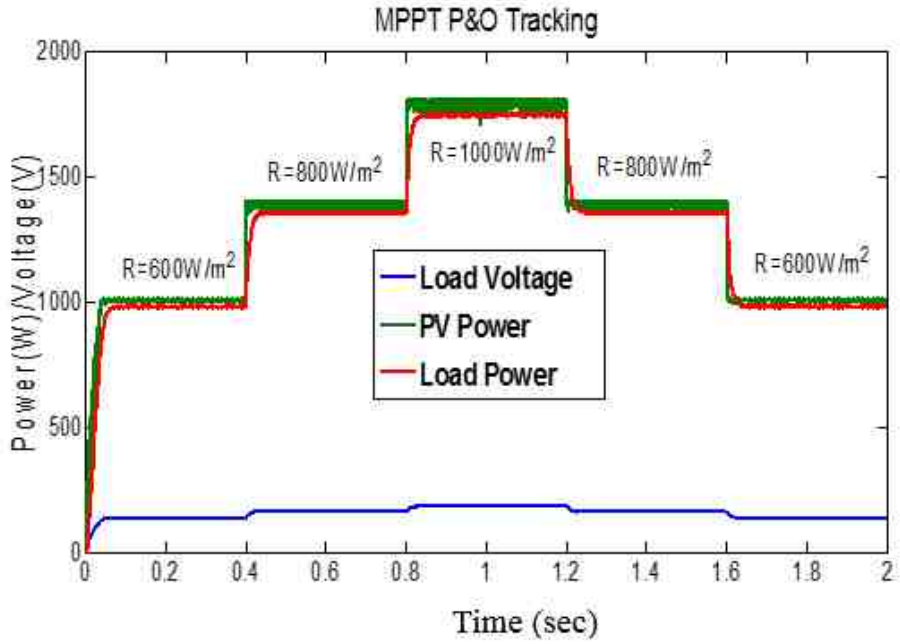


(b) MPPT tracking effect

Fig. 5.12. PV *P&O* MPPT Profile to step change in the irradiance from $600W/m^2$ to $800W/m^2$ to $1000W/m^2$ to $800W/m^2$ to $600W/m^2$

Table 5.2 MPPT Tracking Efficiency in Solar System

| $SolarIrradiance$ | $PVPower$ | $LoadPower$ | $TrackingEfficiency$ |
|---|---|---|---|
| $600W/m^2$ | 1000W | 980W | 98% |
| $800W/m^2$ | 1400W | 1360W | 97.1% |
| $1000W/m^2$ | 1800W | 1750W | 97.1% |

When the load is a DC constant power load (1.5kW)[1]. Simulations of solar MPPT profile for a DC constant power load (1.5kw) and battery with variations of illumination are illustrated in Figure 5.13 and 5.14[1]. Figure 5.13 (a) and (b) show the solar output current and power tracking when the illumination changes from $800W/m^2$ to $1000W/m^2$. Figure 5.14 (a) and (b) depict the solar output current and power tracking when the illumination changes from $1000W/m^2$ to $800W/m^2$.

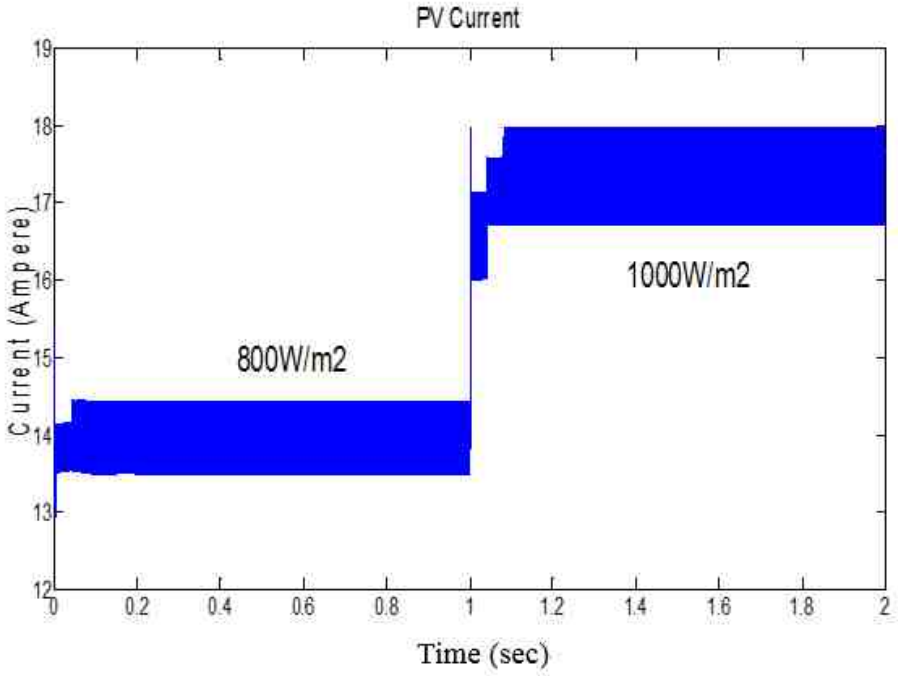


(a) PV current profile

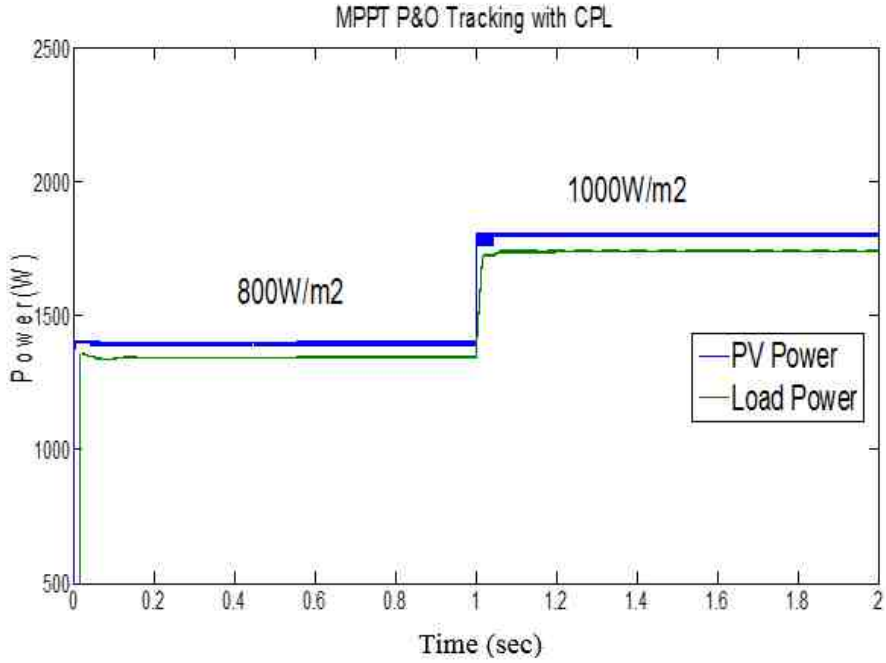


(b) MPPT tracking effect

Fig. 5.13. PV *P&O* MPPT Profile to step change in the irradiance from $800w/m^2$ to $1000w/m^2$ with CPL (1.5kw)

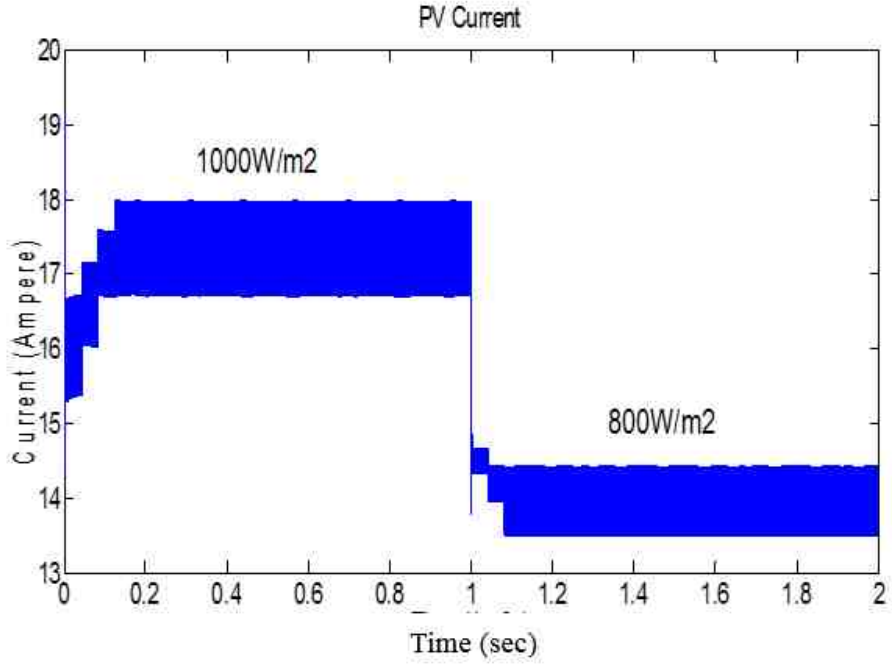


(a) PV current profile

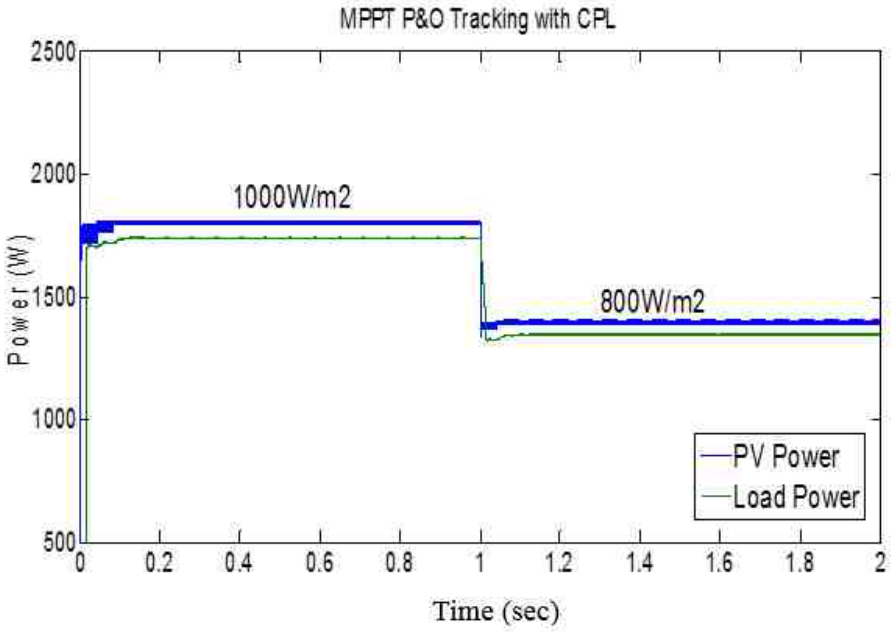


(b) MPPT tracking effect

Fig. 5.14. PV *P&O* MPPT Profile to step change in the irradiance from $1000W/m^2$ to $800W/m^2$ with CPL (1.5kW)

### 5.2.2 Sliding Mode Extremum Seeking Control

In order to verify the sliding mode extremum theory, the whole system is built in Matlab/Simulink[2]. The validity of the proposed system has been checked in the following figures, the sample time of the simulations has been set to 1e-6 sec[2]. The $g_1$ conductance of the first LFR with the illumination changing from $1000W/m^2$ to $800W/m^2$ is shown in Figure 5.15. The $g_2$ conductance of the second LFR with the illumination changing from $700W/m^2$ to $900W/m^2$ is illustrated in Figure 5.16. It is clear that the two conductance values can be controlled automatically under the variations of solar radiations. The waveforms for the cascaded converters behaving as LFRs supplied from PV source under MPPT by applying sliding mode control depicted in Figure 5.17[2]. Figure 5.17 (a) shows the MPP tracking profile with an irradiance change from $1000W/m^2$ to $800W/m^2$ and Figure 5.17 (b) illustrates the waveforms of PV power, voltage and current and first stage voltage during an irradiance change from $800W/m^2$ to $600W/m^2$[2].

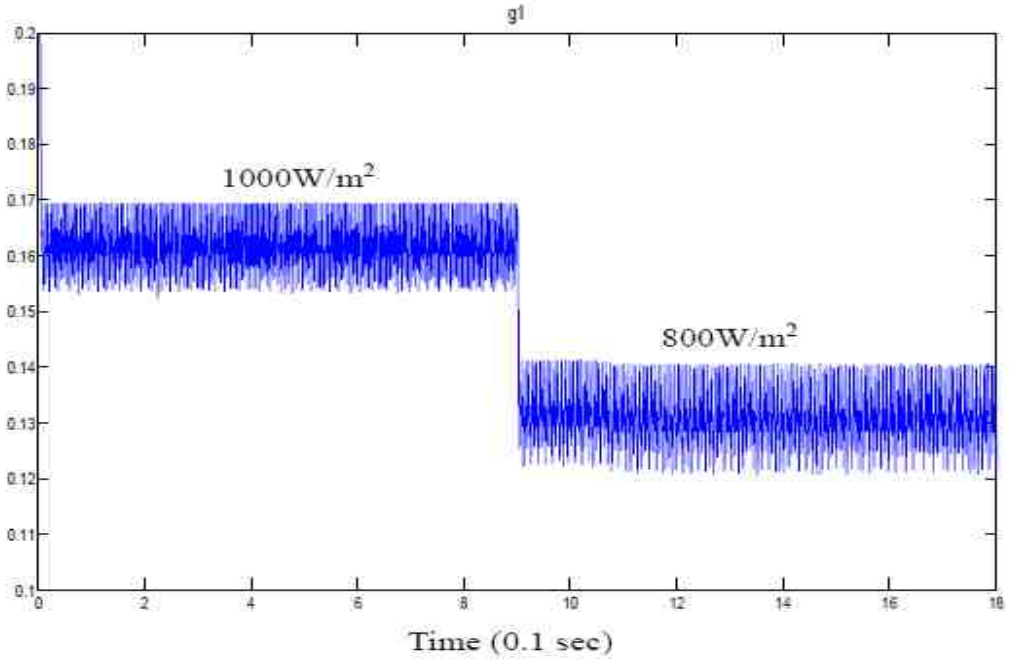


Fig. 5.15. $g_1$ value under Irradiance changing from $1000W/m^2$ to $800W/m^2$

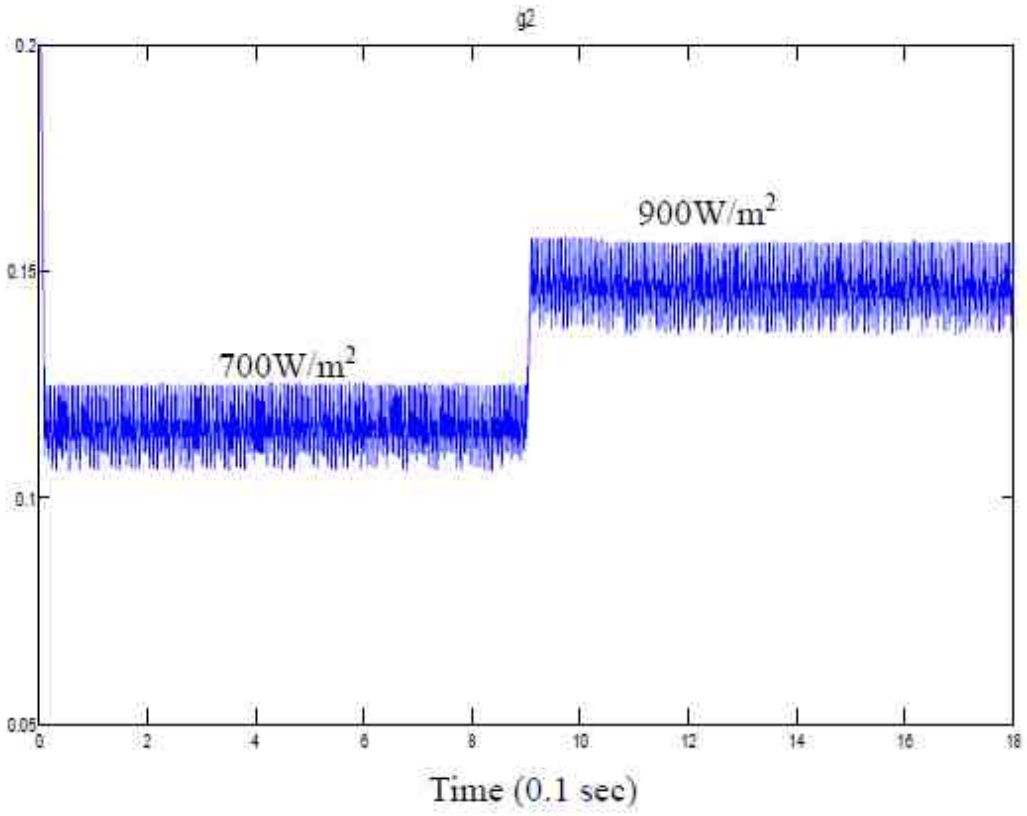


Fig. 5.16. $g_2$ value under Irradiance changing from $700W/m^2$ to $900W/m^2$

Then Figures 5.18 and 5.19 represent the system responses under a step change of the load DC voltage from 240V to 380V and 380V to 240V to show the feasibility of the control system[2]. It can be observed that increasing or decreasing the output voltage does not affect to capture the maximum power of the solar panel in the proposed system[2].

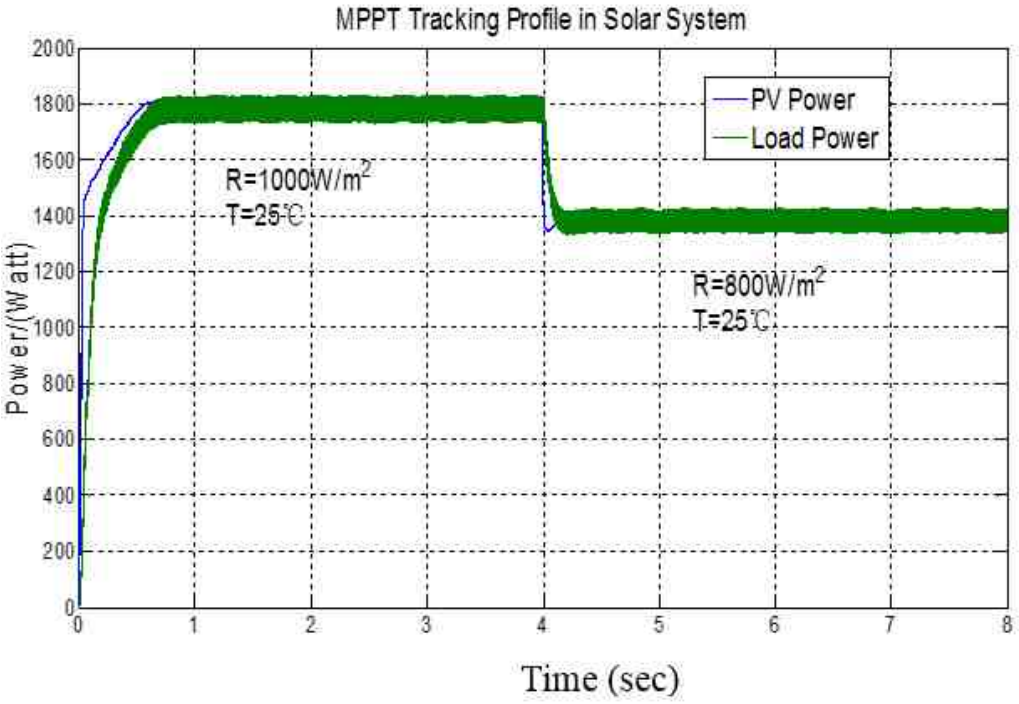


(a) MPPT tracking profile with illumination changing from $1000W/m^2$ to $800W/m^2$

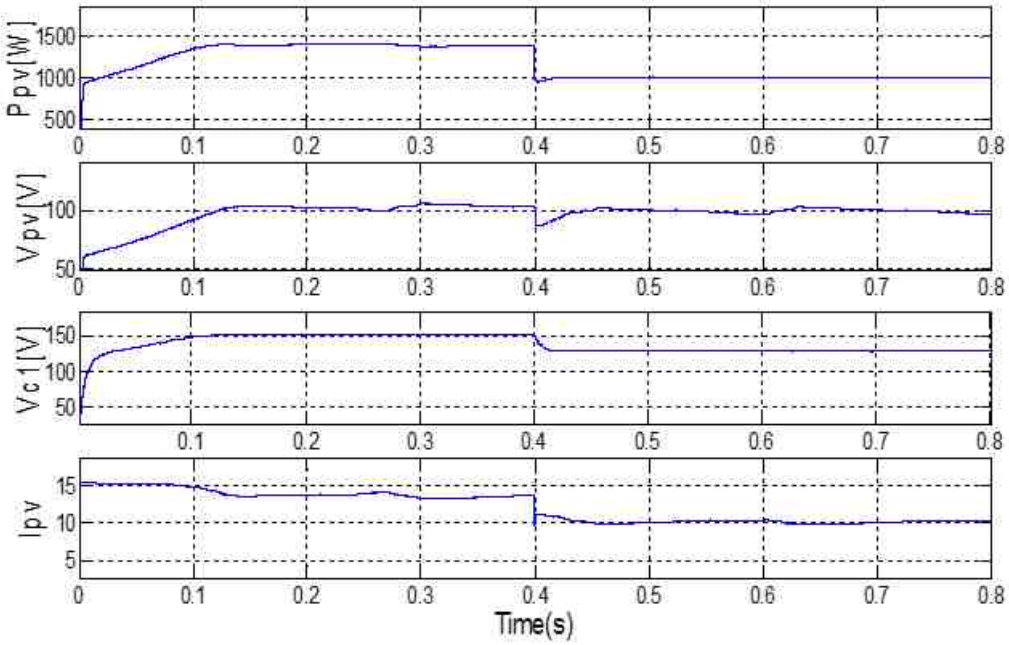


(b) PV power, voltage, current and first stage voltage with illumination changing from $800W/m^2$ to $600W/m^2$

Fig. 5.17. Waveforms for the cascaded converters behaving as LFRs supplied from PV source under MPPT by applying sliding mode control at fixed temperature ($25°C$)

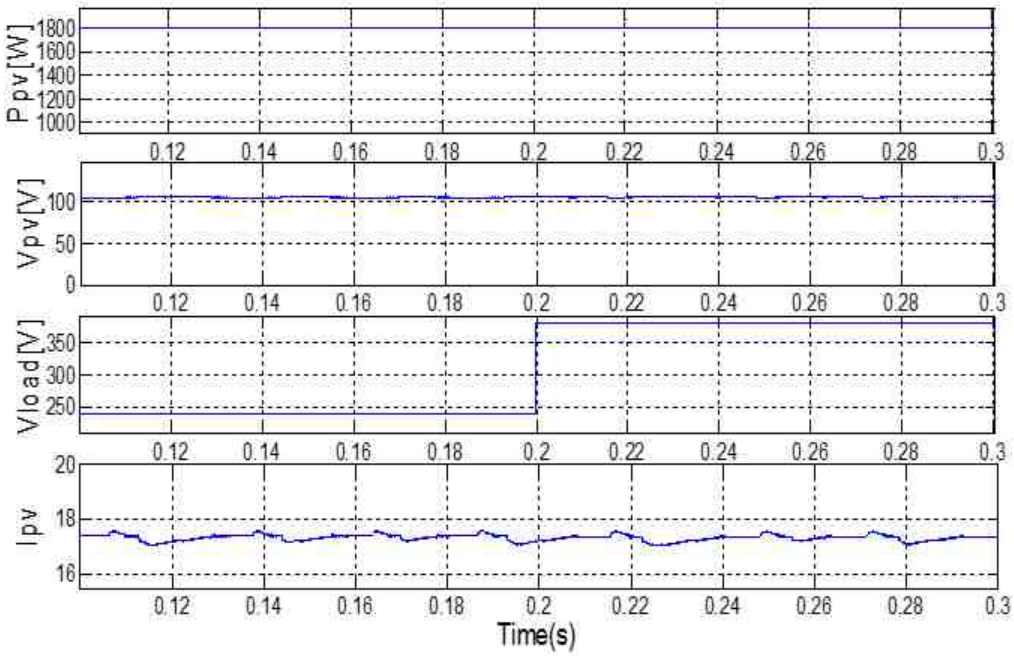


Fig. 5.18. Waveforms of the PV power, PV voltage and current during the load voltage changes from 240V to 380V

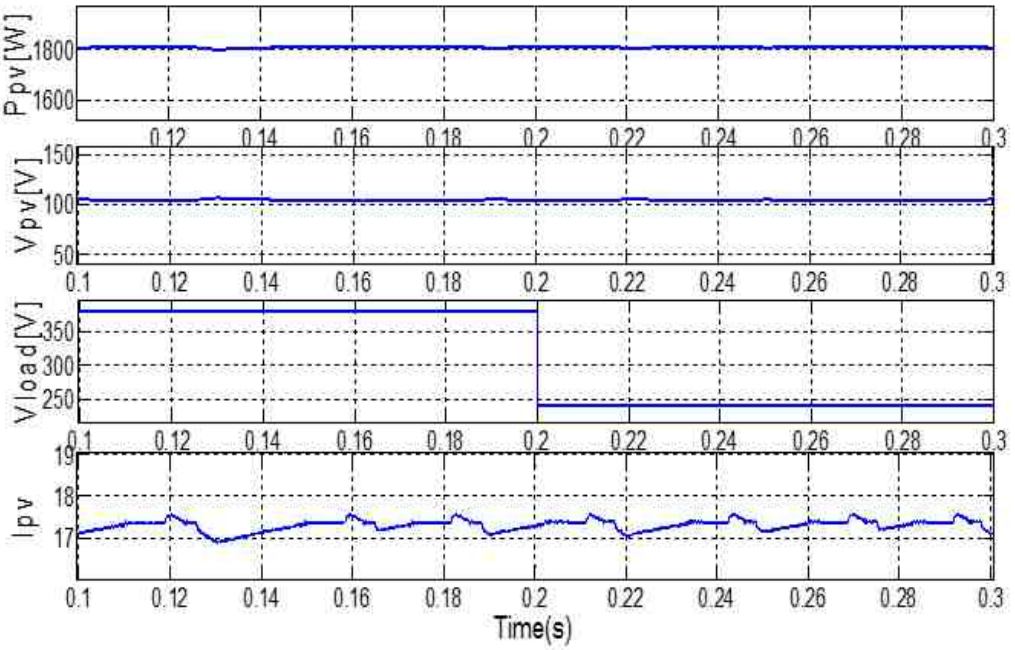


Fig. 5.19. Waveforms of the PV power, PV voltage and current during the load voltage changes from 380V to 240V

### 5.2.3 Comparisons

The MPPT dynamic response of P&O and SM-ESC algorithms with constant solar irradiance are compared in Figure 5.20. From the comparison results, regardless of the 9W power error in solar system, it can be observed that the output power oscillations of SM-ESC method in solar system are smaller than the P&O method, and the tracking speed is nearly the same. The 9W power error in SM-ESC is acceptable with respect to the total generating power around 1300w. Therefore, the SM-ESC control strategy can definitely enhance the capturing efficiency and has better tracking performance than the traditional P&O method.

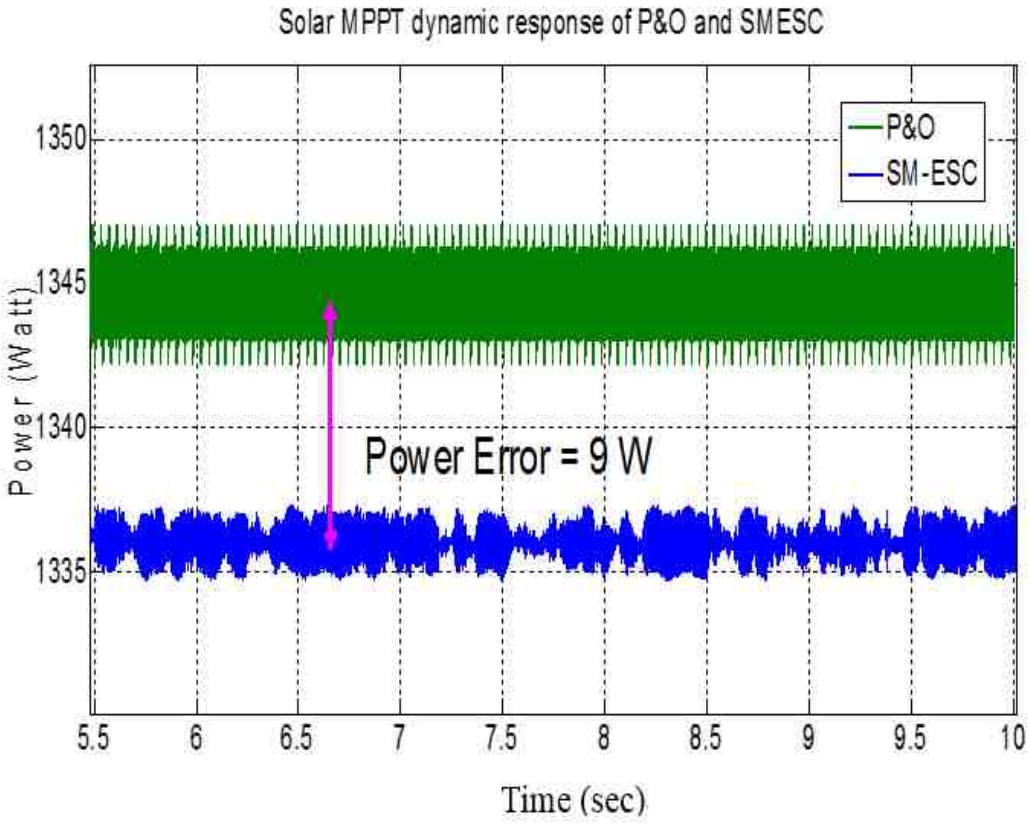


Fig. 5.20. Solar MPPT dynamic response of P&O and SM-ESC

## 5.3 Supervisory Control Effects

This section demonstrates the four supervisory control effects based on the four configurations and supervisory control strategies introduced in the chapter 2 and chapter 4 respectively.

1. Wind-Wind-Storage DC Power System

As depicted in Figure 2.6, the supervisory control effects of wind-wind-storage DC power system by applying SM-ESC approach are represented in the following figures according to the control modes listed in table 4-3. Figure 5.21 mainly depicts the cases of mode 1 and mode 4, where a 300Ah battery feeds the load nearly for about 30 hours without charging at starting SOC of the 80% and the output voltage of the system is regulated around 245V[2], which depends on battery terminal voltage. Initially, the wind speed of turbine 1 and turbine 2 are 7m/s and 10m/s, so the net power injecting to the battery is larger than zero due to the load power demand is 5kw. Thus the power supply can feed the load and charge the battery at the same time that indicates the mode 1. When time comes to 3 seconds, system is in mode 4, because wind speed of turbine 1 and turbine 2 change to 8m/s and 9m/s, and the net power injecting to the battery is less than zero since the load power increase to 9kw, which means now the power supply cannot satisfy the load requirement and battery need to discharge to the load.

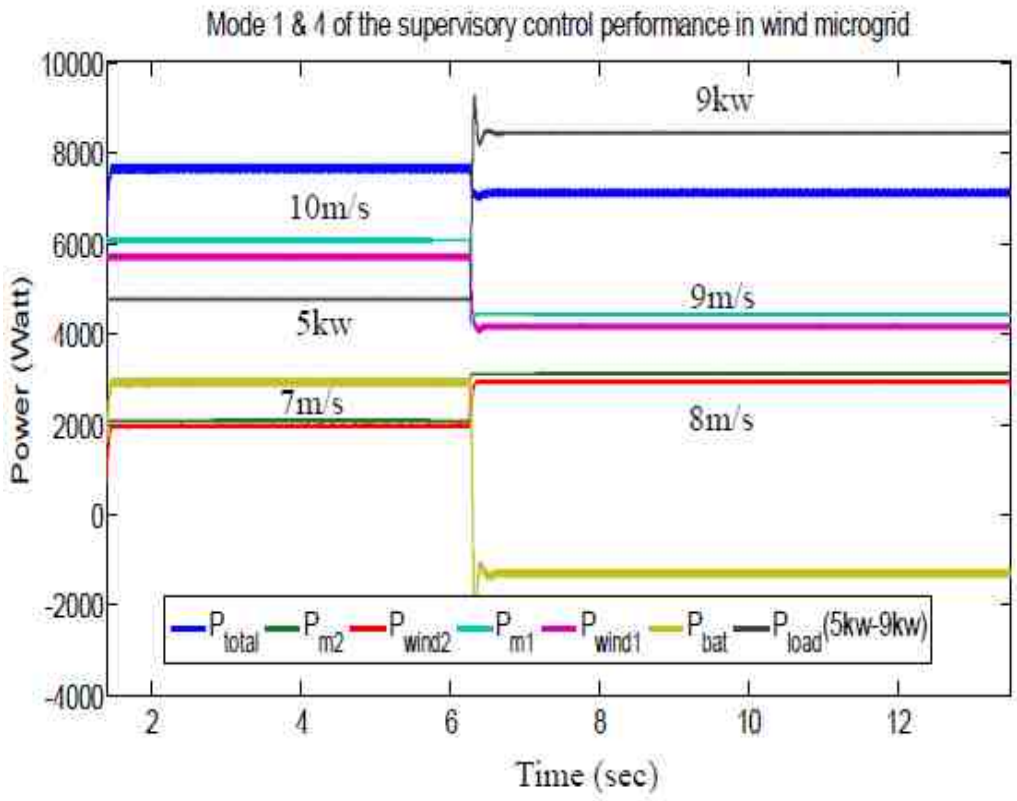


Fig. 5.21. Mode 1&4 of supervisory control performance in wind DC microgrid

Figure 5.22 shows the mode 2 of the distributed system[2]. In this case wind speed of turbine 1 and turbine 2 are 8m/s and 10m/s[2], $\Delta P$ is equal to or larger than zero due to the load power demand is 7kw and SOC is also higher than 95%[2], it is necessary to set the terminal voltage around the battery terminal voltage that floating charges the battery and maintain the capacity[2]. This can also compensate for the self-discharge of the battery[2]. A dummy load is also invoked to consume the surplus energy[2]. Both power controls can be accomplished by limiting the injection of current to the battery and the dummy load based on the DC load requirement[2].

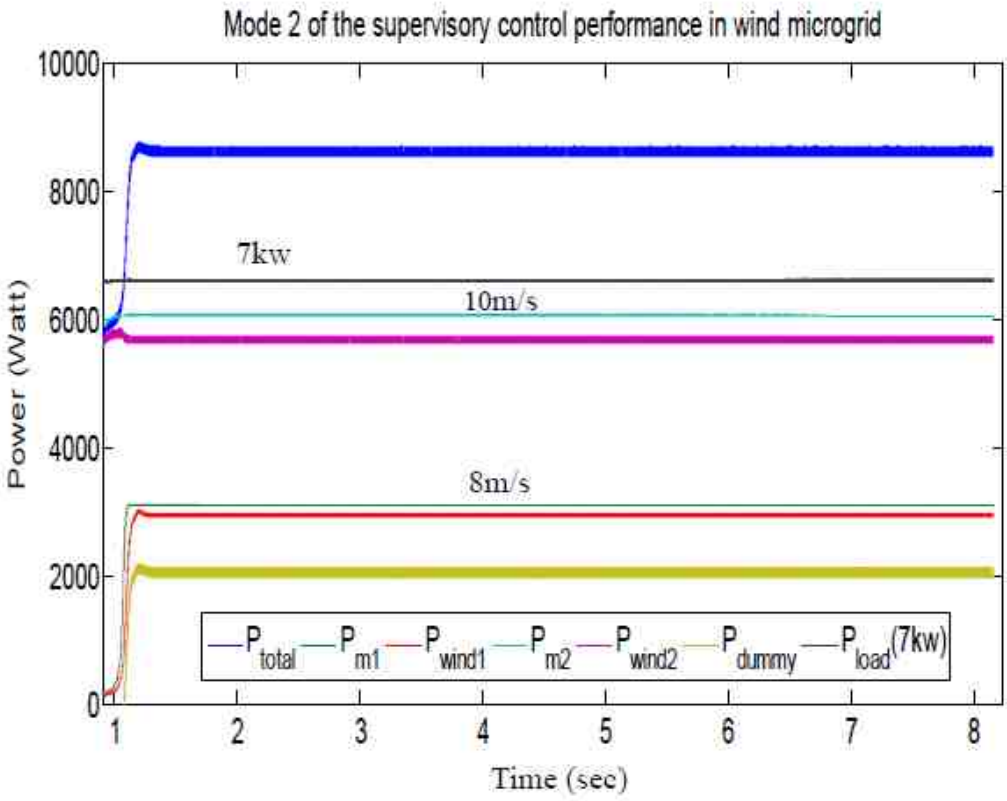


Fig. 5.22. Mode 2 of supervisory control performance in wind DC microgrid

Figure 5.23 illustrates mode 3 in the supervisory control. The wind speed of two turbines are 7m/s and 8m/s. Which presents $\Delta P$ is not larger than zero and SOC lower than 40%[2]. Therefore, the load should be off and the total power captured from two wind turbines is used to charge the battery without satisfying 6kW DC load power[2].

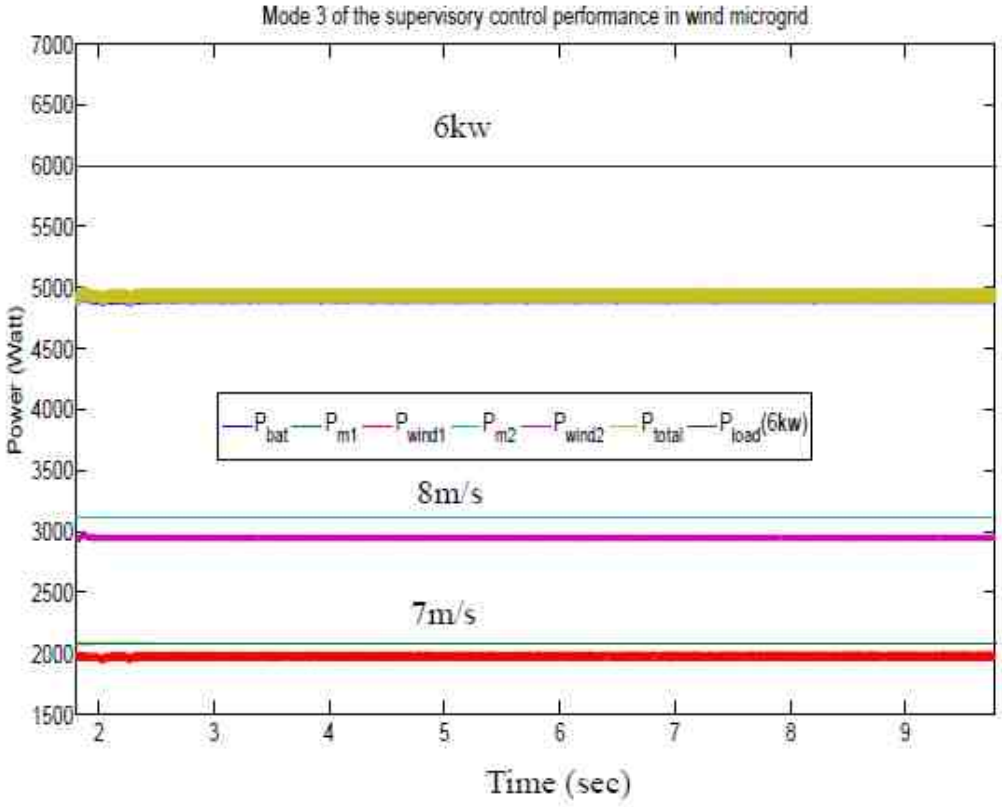


Fig. 5.23. Mode 3 of supervisory control performance in wind DC microgrid

2. Solar-Solar-Storage DC Power System

As depicted in Figure 2.7, the supervisory control effects of solar-solar-storage DC power system by applying SM-ESC approach are represented in the following figures according to the control modes listed in table 4-3. Mode 1 to mode 4 of the supervisory control effects are demonstrated in Figures 5.24-5.26 respectively[2]. Figure 5.24 mainly depicts the cases of mode 1 and mode 4, where a 300Ah battery feeds the load nearly for about 30 hours without charging at starting SOC of the 50% and the output voltage of the system is fixed around battery terminal voltage[2]. Figure 5.24 illustrates the MPP tracking effects of the two solar panels and the response of the battery power with a DC load power change from 2.5kW to 3.5kW to 2.5kW during the irradiance change from $800W/m^2$ to $1000W/m^2$ of PV1 and $700W/m^2$ to $900W/m^2$ of PV2[2]. Figure 5.25 shows the MPP tracking effects of the two solar

panels and the response of the battery power with the same DC load power change during the irradiance change from $1000W/m^2$ to $600W/m^2$ of $PV_1$ and $900W/m^2$ to $700W/m^2$ of $PV_2$[2]. Figure 5.26 depicts the same effects with the same load power change during the irradiance change from $1000W/m^2$ to $600W/m^2$ of $PV_1$ and $700W/m^2$ to $900W/m^2$ of $PV_2$[2]. The operation of controller is verified in Figures 5.24-5.26 under conditions that both PV powers follow the same direction or oppose the direction[2]. The DC microgrid is capable of charging and discharging the battery at the required power rate automatically while capturing the maximum power from two solar panels under variation of irradiance[2].

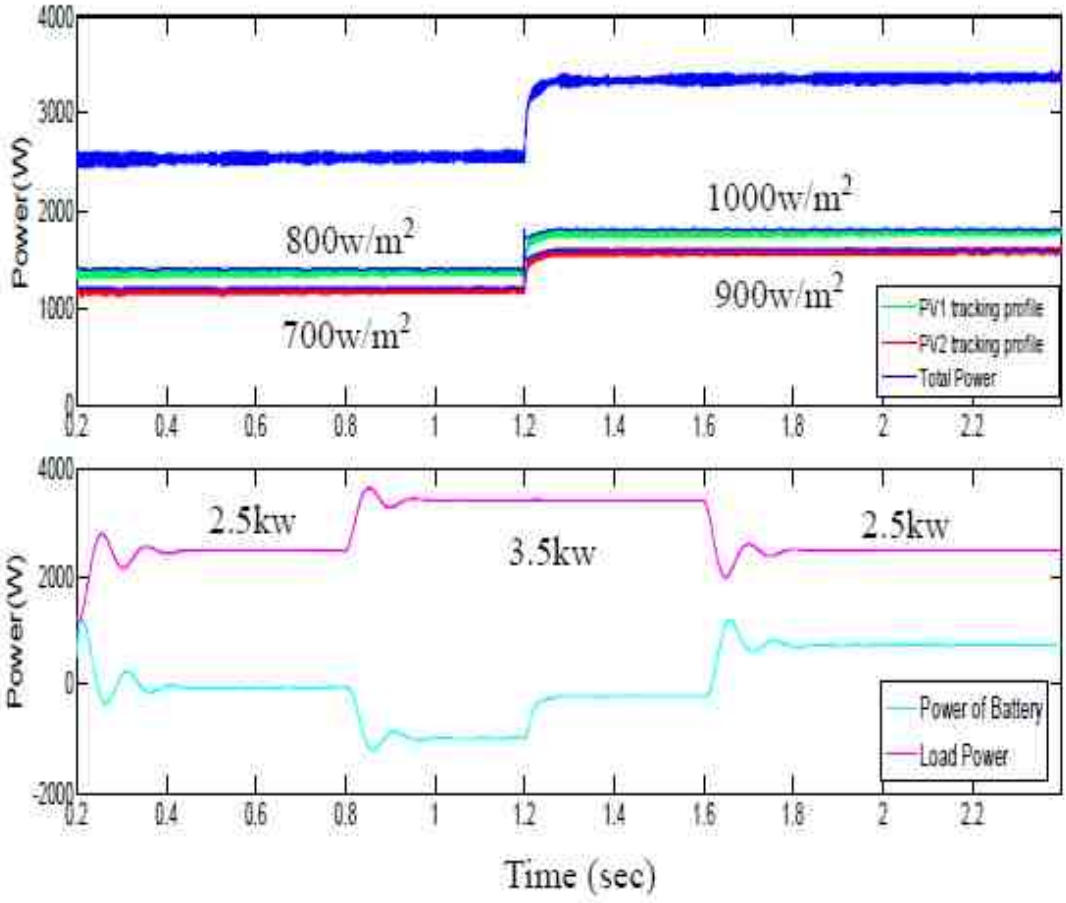


Fig. 5.24. PV MPPT Profile and response of battery power during step change in the load power from 2.5kW to 3.5kW to 2.5kW when irradiance varying from $800W/m^2$ to $1000W/m^2$ of $PV_1$ and $700W/m^2$ to $900W/m^2$ of $PV_2$

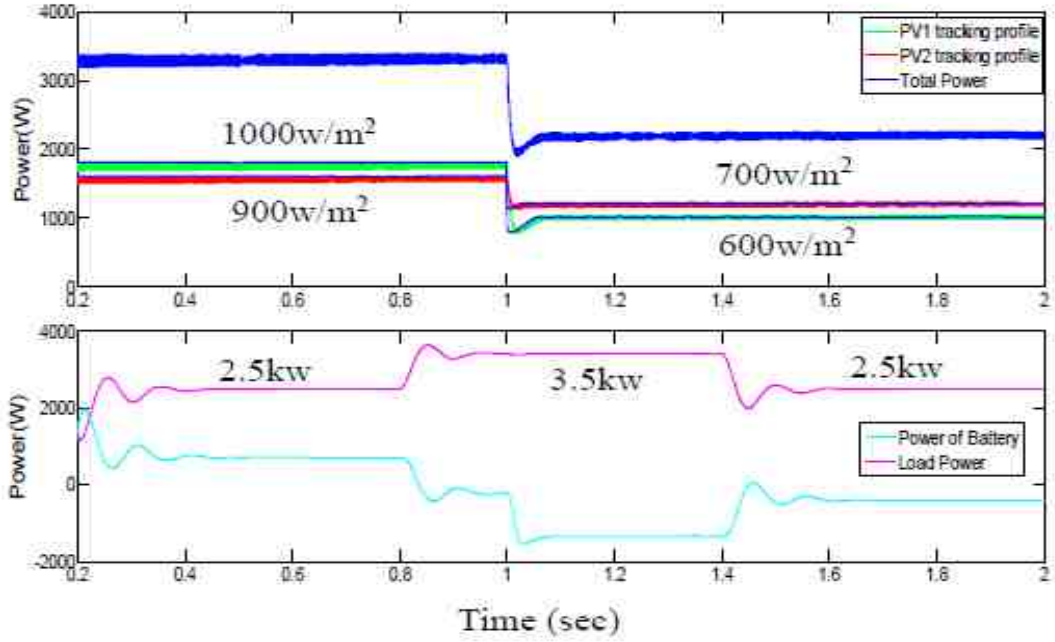


Fig. 5.25. PV MPPT Profile and response of battery power during step change in the load power from 2.5kW to 3.5kW to 2.5kW when irradiance varying from $1000W/m^2$ to $600W/m^2$ of $PV_1$ and $900W/m^2$ to $700W/m^2$ of $PV_2$.

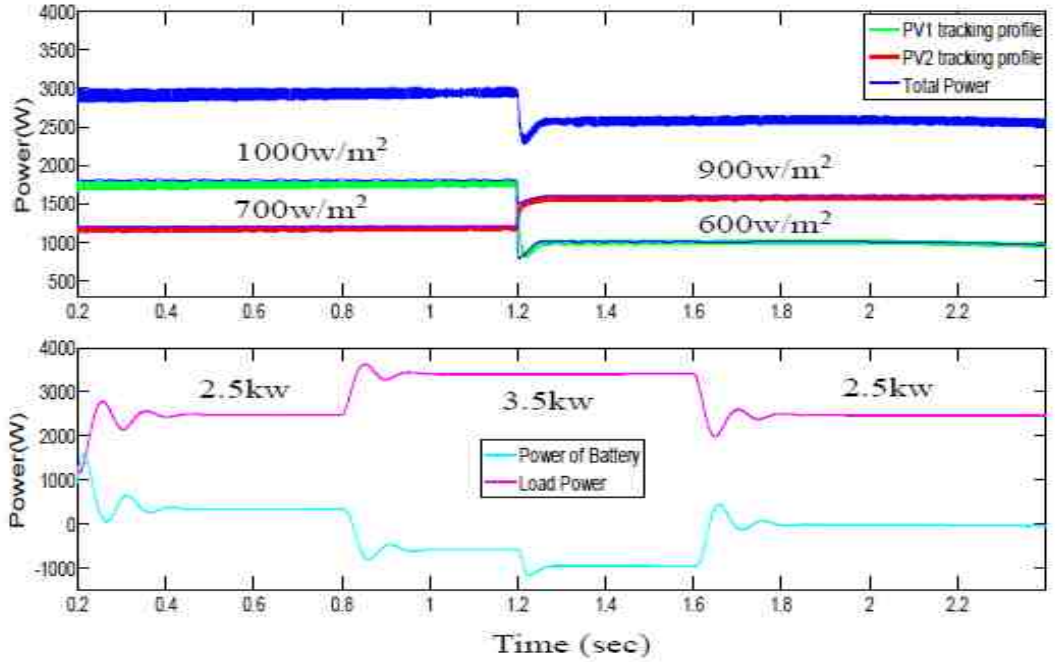


Fig. 5.26. PV MPPT Profile and response of battery power during step change in the load power from 2.5kW to 3.5kW to 2.5kW when irradiance varying from $1000W/m^2$ to $600W/m^2$ of $PV_1$ and $700W/m^2$ to $900W/m^2$ of $PV_2$.

Figure 5.27 shows the mode 2 of the distributed system[2]. In this case $\Delta P$ is equal to or larger than zero and SOC is higher than 95%, it is necessary to set the terminal voltage around 270V that charges the battery and maintain the capacity[2]. This can also compensate for the self-discharge of the battery[2]. A dummy load is also invoked to consume the surplus energy[2]. Both power controls can be accomplished by limiting the injection of current to the battery and the dummy load based on the DC load requirement[2].

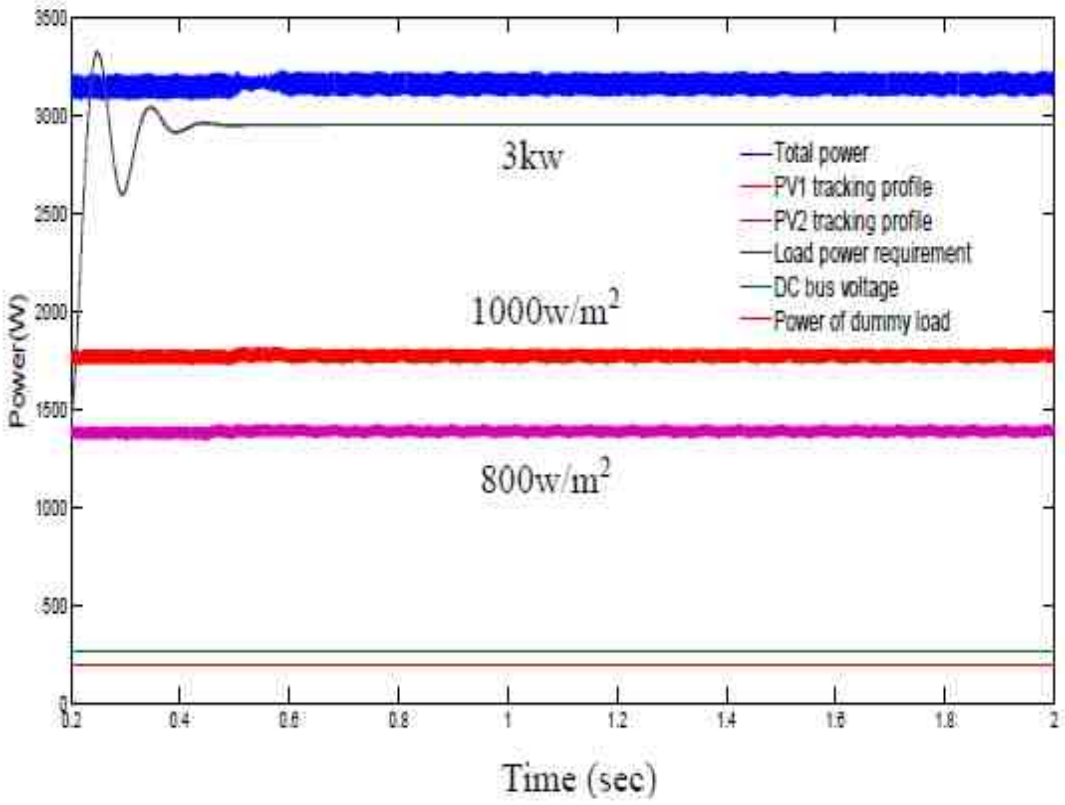


Fig. 5.27. Mode 2 of the supervisory control strategy in solar-solar-storage DC power system

Figure 5.28 illustrates mode 3 which is $\Delta P$ is not larger than zero and SOC lower than 40%[2]. Therefore, the load should be off and the total power captured from two PV sources is used to charge the battery without satisfying 2.5kW DC load power[2].

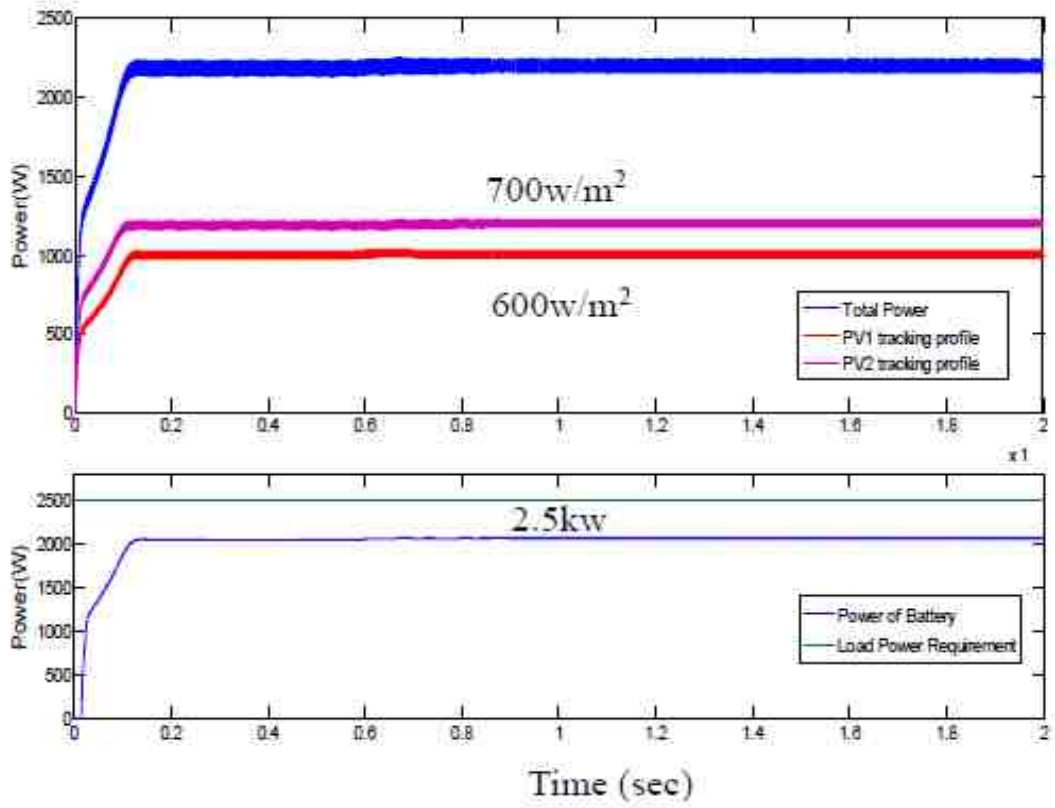


Fig. 5.28. Mode 3 of the supervisory control strategy in solar-solar-storage DC power system

3. Wind-Solar-Storage DC Power System

As depicted in Figure 2.8, the supervisory control effects of wind-solar-storage DC power system by using SM-ESC control method are represented in the following figures according to the control modes listed in table 4-3. The simulation results for the dc constant load and battery that show the supervisory control effect for the combined power system are depicted in Figure 5.29-5.31 respectively[1]. Figure 5.29 mainly demonstrates the mode 1 and mode 4, where the load power reference value changing from 2kw to 4.5kw and the state of charge (SOC) of a 300Ah battery is 80%. It shows the MPP tracking effects of the solar system and wind system[2], and so

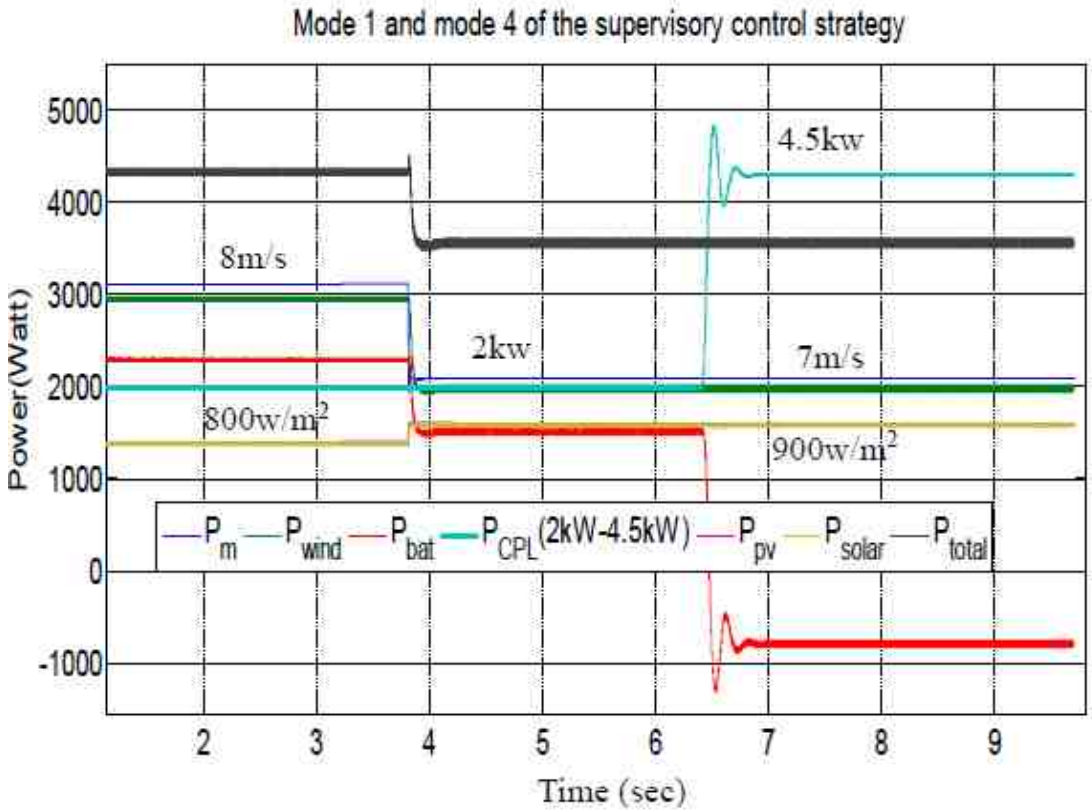


Fig. 5.29. Mode 1 & 4 of supervisory control performance in wind-solar-storage DC power system

the response of the battery power with a DC load power during the irradiance change from $800W/m^2$ to $900W/m^2$ of PV and 8m/s to 7m/s of wind energy system[2]. The DC microgrid is capable of charging and discharging the battery at the required rate automatically while capturing the maximum power from the solar panel and wind system under variations of weather condition[2].

Figure 5.30 illustrates the performance of control in mode 2, where the load power reduces to 5kw and the SOC of battery is 98%. In this case, the solar irradiance experienced a change from $1000W/m^2$ to $800W/m^2$ and the wind speed changing from 9m/s to 10m/s[1]. Now the battery is still be floating charged to maintain the capacity in case of self-discharge. And the surplus power is also consumed through a dummy load.

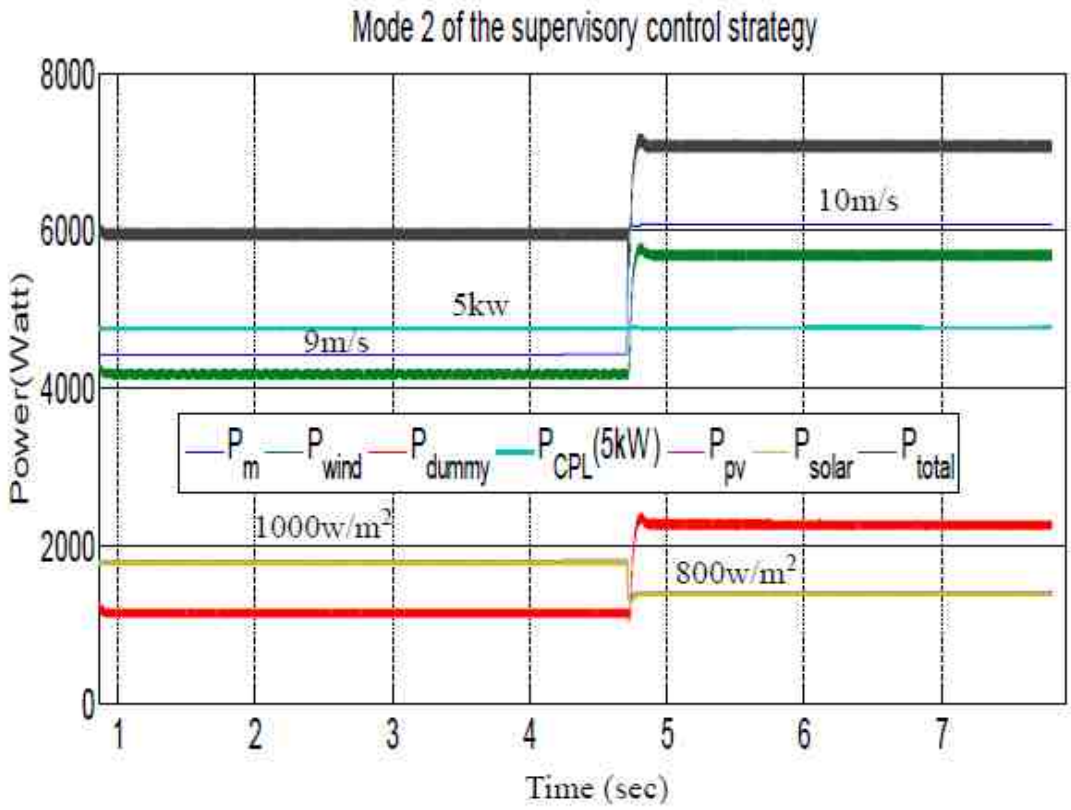


Fig. 5.30. Mode 2 of supervisory control performance in wind-solar-storage DC power system

Figure 5.31 depicts the performance of control in mode 3, where the load power is 5kw and the SOC of battery is 30%. In this case, the solar irradiance changed from $800W/m^2$ to $600W/m^2$ and the wind speed changed from 8m/s to 7m/s[1], which results in $\Delta P$ was not larger than zero and SOC lower than 40%[2]. Therefore, the load should be off and the total power captured from renewable sources was used to charge the battery without satisfying 5kW DC load power[2].

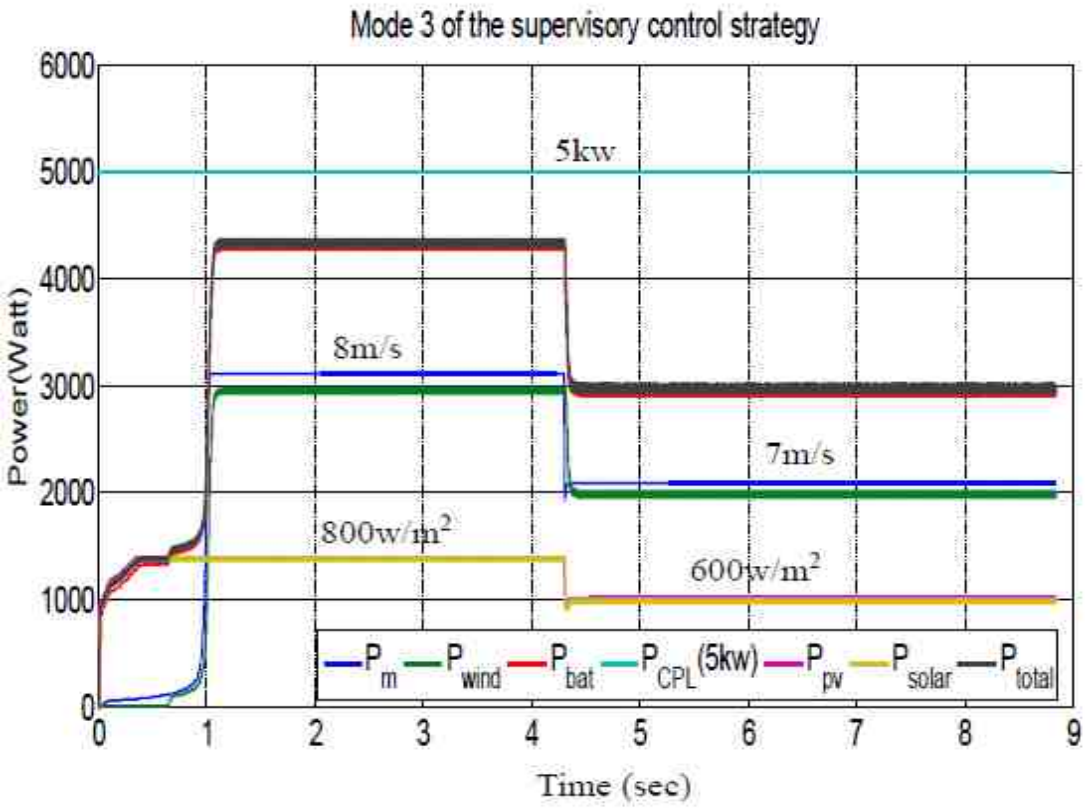


Fig. 5.31. Mode 3 of supervisory control performance in wind-solar-storage DC power system

4. Wind-Solar DC Power System

As depicted in Figure 2.9, the supervisory control effects of wind-solar DC power system by applying P&O approach are represented in the following figures according to the control modes listed in table 4-4.

The simulation results for a 30Ω load that demonstrate the supervisory control for the combined power system are depicted in Figure.5.32-5.34 respectively[1]. Figure 5.32 demonstrates the load power reference value at 7HP and the irradiance is kept constant at $1000W/m^2$[1]. The wind speed is changed from 6m/s to 8m/s to analyze the performance of the proposed supervisory control system[1]. As $\Delta P$ is less than zero

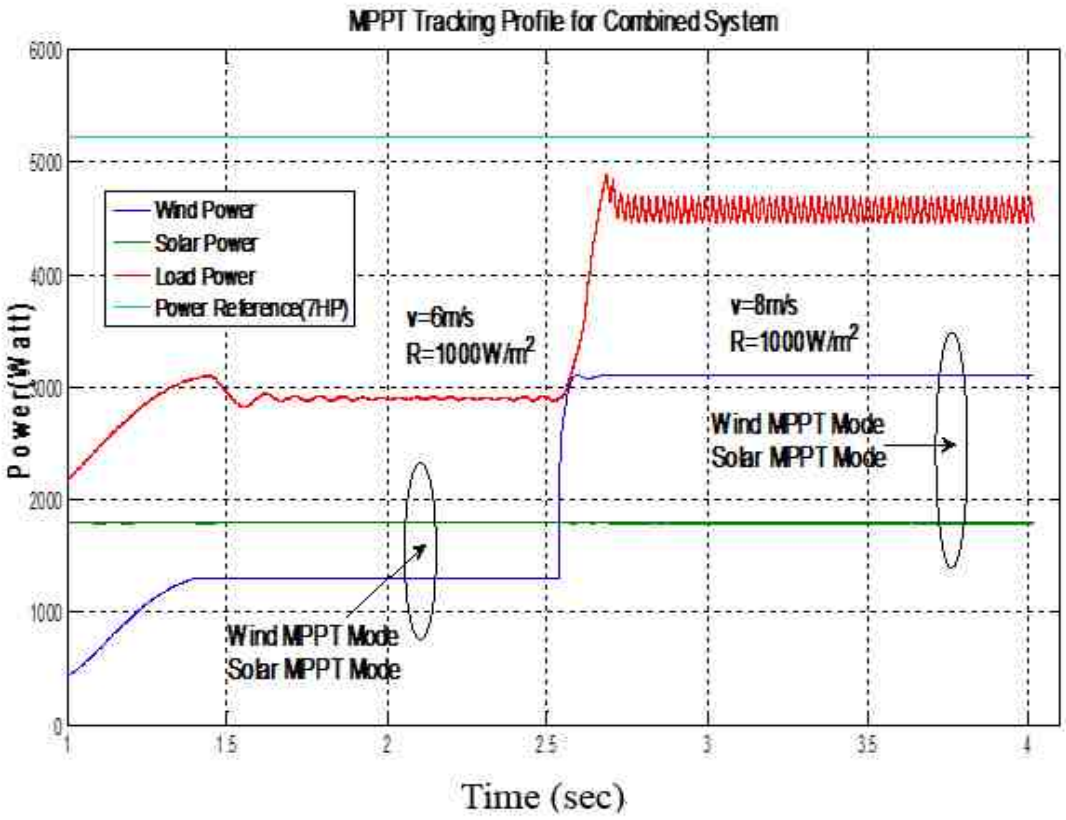


Fig. 5.32. MPPT Tracking profile for combined power generation unit under constant solar irradiance of $1000W/m_2$ and a step change in wind speed from 6m/s to 8m/s

in the simulated wind speeds, both wind and solar power converters operate at MPPT mode[1]. The supervisory controller successfully enabled the power generation unit to track the maximum power from both sources injected to a point of common coupling (PCC) i.e. the DC bus[1]. Thus the power system is in mode 1 of the supervisory control strategy and can satisfy the DC load as much as possible[1].

Figure 5.33 illustrates a load reduction to 5HP under a constant wind speed at rate 8m/s[1]. In this case, the solar irradiance experienced a change from $400W/m^2$ to $1000W/m^2$[1]. At $400W/m^2$, both sources operated at MPPT mode due to the $\Delta P < 0$ condition[1]. As the solar irradiation increased to $1000W/m^2$, $\Delta P > 0$ was hold, suggesting excessive power generation than load demand and the wind power surpassed the solar power generation[1]. Therefore, the wind source is controlled at MPPT mode and solar source is controlled at power tracking mode[1].

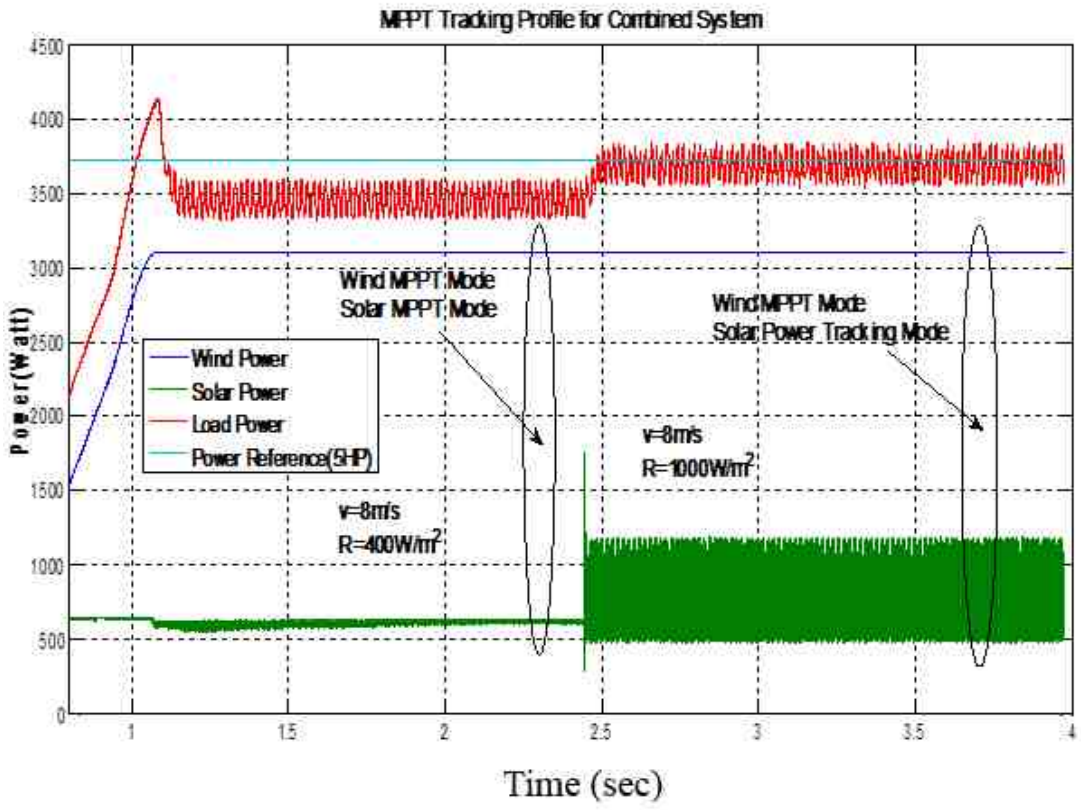


Fig. 5.33. MPPT Tracking profile for combined power system to constant wind speed 8m/s and step change in solar irradiance from $400W/m^2$ to $1000W/m^2$

Figure 5.34 depicts the MPPT tracking profile due to a step change in both wind speed and solar irradiance at a 5HP load power[1]. Initially, the wind speed was 6m/s and the irradiance was $1000W/m^2$[1]. A shortage of energy was observed ($\Delta P < 0$), hence both power sources operated at MPPT mode[1]. Later a wind speed step change to 8m/s and irradiance decrease to $800W/m^2$ generated an excess of energy ($\Delta P > 0$)[1]. Larger power source was set to operate in MPPT mode and the solar power was set to operate in power tracking mode[1].

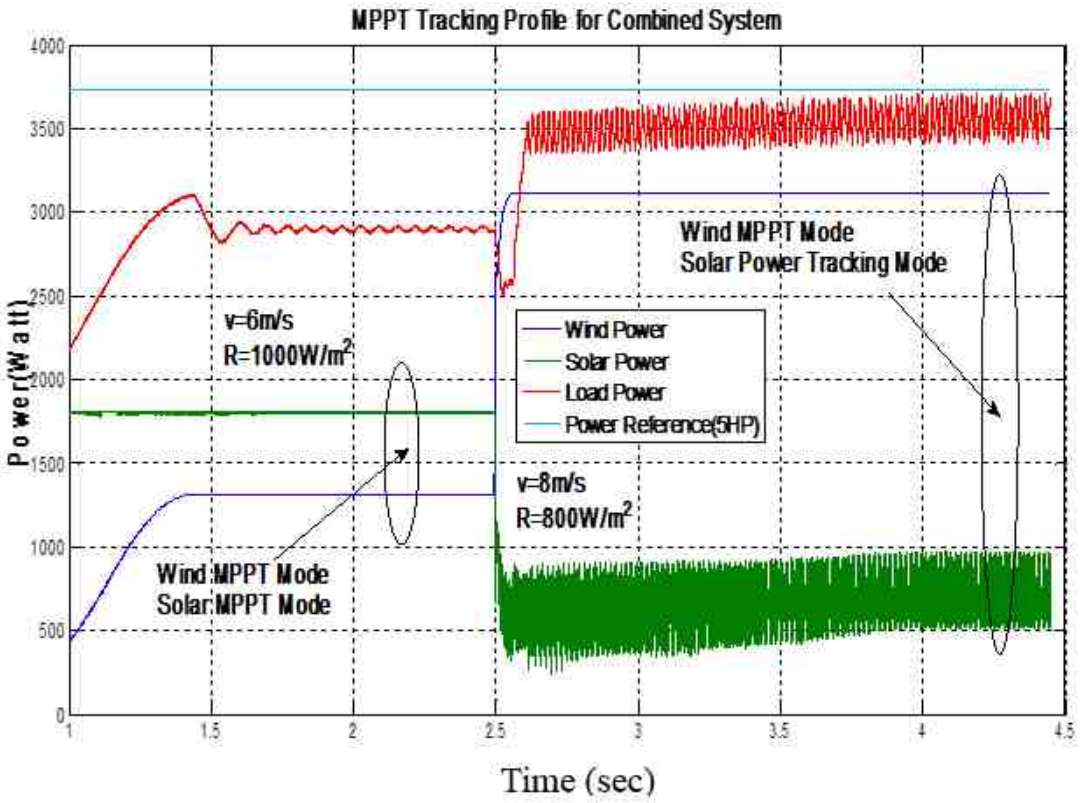


Fig. 5.34. MPPT Tracking profile for combined power system to step change in wind speed from 6m/s to 8m/s and step change in solar irradiance from $1000W/m^2$ to $800W/m^2$

# 6. CONCLUSIONS

This thesis presented the modeling and control of the hybrid distributed renewable energy DC power system. Models of the four proposed configurations of the combined energy generation units are established in Matlab/Simulink.

In wind power system, the P&O method through a SEPIC converter was utilized and the new MPPT controller based on the sliding mode control theory and the extremum seeking control was also applied through a BOOST converter[4]. Both methods illustrated a stable and effective tracking performance with variations of wind speed under DC constant power load[3-4]. Models of wind power systems, SM-ESC MPPT controllers and CPL were built in Matlab/Simulink[2-4]. The BOOST converter can be effectively controlled by a sliding mode structure applying sliding layer concept which represents by a three state function[2],[4]. The specific parameters and operating principle regarding the SM-ESC were also introduced, therefore a sliding mode extremum seeking MPPT controller with adaptive step size can be established[4]. The system responses with step change of DC bus voltage have also been illustrated and analyzed by using the controlled voltage source in the system load side[4].

In solar power system, the P&O method through a BOOST converter was designed and accomplished, and the new MPPT control approach according to the sliding mode extremum seeking control is also investigated and implemented through a cascade BOOST converter. The cascade DC-DC BOOST converters were utilized with high voltage conversion ratios. The cascade connection can be effectively controlled by a sliding mode structure applying a loss free resistor[2]. Therefore, a relationship between the PV voltage and inductor current in BOOST converter can

be established[2]. The full-order switched model of the cascaded circuit has also been established and analyzed by using the Kirchhoff's voltage and current laws[2]. The two sliding mode surfaces and control variables are obtained through a mathematical modeling of circuit and imposing the concept of LFRs[2].

The supervisory control strategy which has four conditions with storage device was also presented to capture the maximum power from each renewable energy sources while connected to a common dc bus[2]. Similar supervisory control strategy without storage device was also proposed to generate the maximum power from these renewable energy sources while connected to a point of common coupling[1]. Robust and smooth supervisory control effects were obtained in both power sources and the four provided integrated systems[1].

Consequently, this thesis developed the control approach for the hybrid sustainable energy DC power systems. The maximum power generated from the power sources can be captured and maintained under the variations of weather condition and the fluctuations of non-linear DC constant power load. By implementing the provided sliding mode extremum seeking control strategy in both wind and solar system, faster tracking speed and smaller oscillations were accomplished with respect to the original P&O method. Satisfied and validated control performances of power flow in each combined energy system are achieved. The simulation results also demonstrated the accurate operation and functionality of the presented control methods.

# 7. FUTURE WORK

The main objective of the thesis is to focus on some preliminary research regarding the modeling and adaptive control of hybrid new energy system. Although many works have been investigated and realized, there are still many deficiencies and drawbacks need to be discovered and enhanced. Generally, it can be categorized as below:

1. Only DC microgrid is introduced and considered in the thesis, including DC/DC converter and DC constant power load. The AC microgrid and AC load are not involved here, and neither running comprehensive experimental tests based on the real solar panel and wind turbine. Therefore, the work should be extended from DC microgrid to hybrid microgrid which containing both DC and AC components, such as DC/DC converter, DC/AC inverter, AC/DC converter and AC/AC inverter according to the practical requirements.

2. Because the battery is connected directly to a common DC bus, so the DC bus voltage is clamped by the battery terminal voltage. There are definitely some advantages by using this connection, such as more convenient and flexible. It should be noticed that many configurations have utilized a bi-directional converter to interface with battery. In this case, more efficient DC bus control and load sharing approaches need to be studied and discussed, droop control, secondary control and so on. In addition, it is similar to the AC bus voltage control strategy.

3. The fault detection and protection technology is also a significant meaningful research area, especially for the power systems. The hybrid power system has many integrated components and each component can be viewed as a smaller system. All parts work together and compensate with each other. Thus, acccurate fault diagnosis

methods should be investigated and implemented in this research. Industry applications should be considered, such as multiple model adaptive estimation (MMAE) technique which can generate probabilities that determine the signature faults for Li-ion battery and Markov Chains which can predict the probability distribution of the next state depends only on the current state.

4. The constant power load significantly affects the stability and robustness of power system. It is therefore meaningful to focus on the global stability of such energy systems by applying the adaptive control effects. One method is to compute the region of attraction (ROA) for the operating points. There are other approaches of obtaining an estimation on the ROA, such as genetic algorithms and mixed Lyapunov functions.

# LIST OF REFERENCES

# LIST OF REFERENCES


[1] D. Shen and A. Izadian, "Modeling and control of a combined wind-solar microgrid," in *IECON 2014-40th Annual Conference of the IEEE Industrial Electronics Society*, pp. 2173–2179, IEEE, 2014.

[2] D. Shen and A. Izadian, "Sliding mode control of a dc distributed solar microgrid," in *2015 IEEE Power and Energy Conference at Illinois (PECI)*, pp. 1–6, IEEE, 2015.

[3] D. Shen, A. Izadian, and P. Liao, "A hybrid wind-solar-storage energy generation system configuration and control," in *2014 IEEE of Energy Conversion Congress and Exposition (ECCE)*, pp. 436–442, IEEE, 2014.

[4] D. Shen, P. Khayyer, and A. Izadian, "Sliding mode extremum seeking control for maximum power point tracking in wind system," in *2016 IEEE Power and Energy Conference at Illinois (PECI)*, IEEE, 2016.

[5] A. Izadian, N. Girrens, and P. Khayyer, "Renewable energy policies: A brief review of the latest us and eu policies," *Industrial Electronics Magazine, IEEE*, vol. 7, no. 3, pp. 21–34, 2013.

[6] B. Beltran, T. Ahmed-Ali, and M. E. H. Benbouzid, "Sliding mode power control of variable-speed wind energy conversion systems," *IEEE Transactions on Energy Conversion*, vol. 23, no. 2, pp. 551–558, 2008.

[7] L. Soder, L. Hofmann, A. Orths, H. Holttinen, Y.-h. Wan, and A. Tuohy, "Experience from wind integration in some high penetration areas," *IEEE Transactions on Energy Conversion*, vol. 22, no. 1, pp. 4–12, 2007.

[8] G. J. Herbert, S. Iniyan, E. Sreevalsan, and S. Rajapandian, "A review of wind energy technologies," *Renewable and sustainable energy Reviews*, vol. 11, no. 6, pp. 1117–1145, 2007.

[9] R. G. Wandhare and V. Agarwal, "Novel control scheme to reduce the effect of intermittent solar radiation on the grid connected pv system power output without losing mppt," in *2012 Twenty-Seventh Annual IEEE of Applied Power Electronics Conference and Exposition (APEC)*, pp. 79–85, IEEE, 2012.

[10] H. Fargli, F. Fahmy, and M. El-Sayed, "Artificial intelligence techniques for controlling pv-wind powered rural zone in egypt," in *Proceedings of International Conference on Renewable Energies and Power Quality. Valencia*, 2009.

[11] O. Onar, M. Uzunoglu, and M. Alam, "Modeling, control and simulation of an autonomous wind turbine/photovoltaic/fuel cell/ultra-capacitor hybrid power system," *Journal of Power Sources*, vol. 185, no. 2, pp. 1273–1283, 2008.

[12] R. G. Wandhare and V. Agarwal, "A control strategy to reduce the effect of intermittent solar radiation and wind velocity in the hybrid photovoltaic/wind scig system without losing mppt," in *2012 38th IEEE of Photovoltaic Specialists Conference (PVSC)*, pp. 001399–001404, IEEE, 2012.

[13] M. Cirstea and A. Parera-Ruiz, "An fpga controller for a combined solar/wind power system," in *2010 12th International Conference on Optimization of Electrical and Electronic Equipment (OPTIM)*, pp. 1103–1108, IEEE, 2010.

[14] F. Nejabatkhah, S. Danyali, S. H. Hosseini, M. Sabahi, and S. M. Niapour, "Modeling and control of a new three-input dc–dc boost converter for hybrid pv/fc/battery power system," *IEEE Transactions on Power Electronics*, vol. 27, no. 5, pp. 2309–2324, 2012.

[15] E. M. Natsheh, A. R. Natsheh, and A. Albarbar, "Intelligent controller for managing power flow within standalone hybrid power systems," *Science, Measurement & Technology, IET*, vol. 7, no. 4, pp. 191–200, 2013.

[16] M. Pahlevani, S. Eren, J. M. Guerrero, and P. Jain, "A hybrid estimator for active/reactive power control of single-phase distributed generation systems with energy storage," *IEEE Transactions on Power Electronics*, vol. 31, no. 4, pp. 2919–2936, 2016.

[17] A. M. Gee, F. V. Robinson, and R. W. Dunn, "Analysis of battery lifetime extension in a small-scale wind-energy system using supercapacitors," *IEEE Transactions on Energy Conversion*, vol. 28, no. 1, pp. 24–33, 2013.

[18] A. Barchowsky, J. P. Parvin, G. F. Reed, M. J. Korytowski, and B. M. Grainger, "A comparative study of mppt methods for distributed photovoltaic generation," in *2012 IEEE PES of Innovative Smart Grid Technologies (ISGT)*, pp. 1–7, IEEE, 2012.

[19] A. Sannino, G. Postiglione, and M. H. Bollen, "Feasibility of a dc network for commercial facilities," *IEEE Transactions on Industry Applications*, vol. 39, no. 5, pp. 1499–1507, 2003.

[20] D. Nilsson, *DC distribution systems.* PhD thesis, Chalmers tekniska högsk.2005. http://webfiles.portal.chalmers.se/et/Lic/NilssonDanielLic.pdf, Last Date Accessed: April 12, 2016.

[21] C. Xu and K. Cheng, "A survey of distributed power system—ac versus dc distributed power system," in *2011 4th International Conference on Power Electronics Systems and Applications (PESA)*, pp. 1–12, IEEE, 2011.

[22] B. Fahimi, A. Kwasinski, A. Davoudi, R. Balog, and M. Kiani, "Charge it!," *IEEE power and energy magazine*, vol. 4, no. 9, pp. 54–64, 2011.

[23] Y.-C. Chang, C.-L. Kuo, K.-H. Sun, and T.-C. Li, "Development and operational control of two-string maximum power point trackers in dc distribution systems," *IEEE Transactions on Power Electronics*, vol. 28, no. 4, pp. 1852–1861, 2013.

[24] P. A. Madduri, J. Rosa, S. R. Sanders, E. A. Brewer, and M. Podolsky, "Design and verification of smart and scalable dc microgrids for emerging regions," in *2013 IEEE Energy Conversion Congress and Exposition (ECCE)*, pp. 73–79, IEEE, 2013.

[25] S. M. Barakati, M. Kazerani, and J. D. Aplevich, "Maximum power tracking control for a wind turbine system including a matrix converter," *IEEE Transactions on Energy Conversion*, vol. 24, no. 3, pp. 705–713, 2009.

[26] R. Cárdenas and R. Pena, "Sensorless vector control of induction machines for variable-speed wind energy applications," *IEEE Transactions on Energy Conversion*, vol. 19, no. 1, pp. 196–205, 2004.

[27] A. G. Abo-Khalil and D.-C. Lee, "Mppt control of wind generation systems based on estimated wind speed using svr," *IEEE Transactions on Industrial Electronics*, vol. 55, no. 3, pp. 1489–1490, 2008.

[28] E. Koutroulis and K. Kalaitzakis, "Design of a maximum power tracking system for wind-energy-conversion applications," *IEEE transactions on industrial electronics*, vol. 53, no. 2, pp. 486–494, 2006.

[29] C. Yu and K. Chau, "Thermoelectric automotive waste heat energy recovery using maximum power point tracking," *Energy Conversion and Management*, vol. 50, no. 6, pp. 1506–1512, 2009.

[30] S. Korovin and V. Utkin, "Use of slip mode in problems of static optimization," *Automation and Remote Control*, vol. 33, no. 4, p. 570, 1972.

[31] S. Korovin and V. Utkin, "Using sliding modes in static optimization and nonlinear programming," *Automatica*, vol. 10, no. 5, pp. 525–532, 1974.

[32] T. Pan, Z. Ji, and Z. Jiang, "Maximum power point tracking of wind energy conversion systems based on sliding mode extremum seeking control," in *Energy 2030 Conference, 2008. ENERGY 2008. IEEE*, pp. 1–5, IEEE, 2008.

[33] K. B. Ariyur and M. Krstic, *Real-time optimization by extremum-seeking control*. John Wiley & Sons, 2003.

[34] J.-H. Chen, H.-T. Yau, and W. Hung, "Design and study on sliding mode extremum seeking control of the chaos embedded particle swarm optimization for maximum power point tracking in wind power systems," *Energies*, vol. 7, no. 3, pp. 1706–1720, 2014.

[35] H.-T. Yau, C.-J. Lin, and C.-H. Wu, "Sliding mode extremum seeking control scheme based on pso for maximum power point tracking in photovoltaic systems," *International Journal of Photoenergy*, vol. 2013, 2013.

[36] E. Bianconi, J. Calvente, R. Giral, E. Mamarelis, G. Petrone, C. A. Ramos-Paja, G. Spagnuolo, and M. Vitelli, "A fast current-based mppt technique employing sliding mode control," *IEEE Transactions on Industrial Electronics*, vol. 60, no. 3, pp. 1168–1178, 2013.

[37] P. E. Kakosimos, A. G. Kladas, and S. N. Manias, "Fast photovoltaic-system voltage-or current-oriented mppt employing a predictive digital current-controlled converter," *IEEE Transactions on Industrial Electronics*, vol. 60, no. 12, pp. 5673–5685, 2013.

[38] G.-C. Hsieh, H.-I. Hsieh, C.-Y. Tsai, and C.-H. Wang, "Photovoltaic power-increment-aided incremental-conductance mppt with two-phased tracking," *IEEE Transactions on Power Electronics*, vol. 28, no. 6, pp. 2895–2911, 2013.

[39] A. M. Bazzi and P. T. Krein, "Ripple correlation control: an extremum seeking control perspective for real-time optimization," *IEEE Transactions on Power Electronics*, vol. 29, no. 2, pp. 988–995, 2014.

[40] V. V. Scarpa, S. Buso, and G. Spiazzi, "Low-complexity mppt technique exploiting the pv module mpp locus characterization," *IEEE Transactions on Industrial Electronics*, vol. 56, no. 5, pp. 1531–1538, 2009.

[41] R. A. Badwawi, M. Abusara, and T. Mallick, "A review of hybrid solar pv and wind energy system," *Smart Science*, vol. 3, no. 3, pp. 127–138, 2015.

[42] M. R. Patel, *Wind and solar power systems: design, analysis, and operation*. CRC press, 2005.

[43] A. Mesemanolis, C. Mademlis, and I. Kioskeridis, "A fuzzy-logic based control strategy for maximum efficiency of a wind energy conversion system," in *2012 International Symposium on Power Electronics, Electrical Drives, Automation and Motion (SPEEDAM)*, pp. 7–12, IEEE, 2012.

[44] P. Baltas *et al.*, "The arizona university photovoltaic designer program [z]," *Department of electrical and computer engineering, Arizona state University,1996*, http://scholar.google.com/scholar?q=The+Arizona+University+Photovoltaic+Designer+Program+btnG=hl=enas-sdt=02C15, Last Date Accessed:April 12,2016.

[45] C. Onwuchekwa and A. Kwasinski, "Analysis of boundary control for boost and buck-boost converters in distributed power architectures with constant-power loads," in *2011 Twenty-Sixth Annual IEEE Applied Power Electronics Conference and Exposition (APEC)*, pp. 1816–1823, IEEE, 2011.

[46] X. Lu, K. Sun, J. M. Guerrero, J. C. Vasquez, L. Huang, and J. Wang, "Stability enhancement based on virtual impedance for dc microgrids with constant power loads," *IEEE Transactions on Smart Grid*, vol. 6, no. 6, pp. 2770–2783, 2015.

[47] M. Krstić and H.-H. Wang, "Stability of extremum seeking feedback for general nonlinear dynamic systems," *Automatica*, vol. 36, no. 4, pp. 595–601, 2000.

[48] A. Saghafinia, H. W. Ping, M. N. Uddin, and K. S. Gaeid, "Adaptive fuzzy sliding-mode control into chattering-free im drive," *IEEE Transactions on Industry Applications*, vol. 51, no. 1, pp. 692–701, 2015.

[49] C. Yin, Y. Chen, and S.-m. Zhong, "Fractional-order sliding mode based extremum seeking control of a class of nonlinear systems," *Automatica*, vol. 50, no. 12, pp. 3173–3181, 2014.

[50] C. Olalla, M. I. Arteaga, R. Leyva, and A. El Aroudi, "Analysis and comparison of extremum seeking control techniques," in *IEEE ISIE Conf*, pp. 72–6, 2007.

[51] R. D. Middlebrook, "Input filter considerations in design and application of switching regulators," *IAS Record, 1976*, 1976.

[52] S. Singer and R. W. Erickson, "Canonical modeling of power processing circuits based on the popi concept," *IEEE Transactions on Power Electronics*, vol. 7, no. 1, pp. 37–43, 1992.

[53] S. Singer, "Realization of loss-free resistive elements," *IEEE Transactions on Circuits and Systems*, vol. 37, no. 1, pp. 54–60, 1990.

[54] R. Haroun, A. El Aroudi, A. Cid-Pastor, G. Garica, C. Olalla, and L. Martinez-Salamero, "Impedance matching in photovoltaic systems using cascaded boost converters and sliding-mode control," *IEEE Transactions on Power Electronics*, vol. 30, no. 6, pp. 3185–3199, 2015.

[55] L. Martinez-Salamero, "Synthesis of canonical elements for power processing," in *2009. SSD'09. 6th International Multi-Conference on Systems, Signals and Devices*, pp. 1–6, IEEE, 2009.

[56] T. Noguchi, S. Togashi, and R. Nakamoto, "Short-current pulse-based maximum-power-point tracking method for multiple photovoltaic-and-converter module system," *IEEE Transactions on Industrial Electronics*, vol. 49, no. 1, pp. 217–223, 2002.

[57] N. Femia, G. Petrone, G. Spagnuolo, and M. Vitelli, "Optimization of perturb and observe maximum power point tracking method," *IEEE Transactions on Power Electronics*, vol. 20, no. 4, pp. 963–973, 2005.

[58] M. A. G. De Brito, L. Galotto Jr, L. P. Sampaio, G. de Azevedo e Melo, and C. A. Canesin, "Evaluation of the main mppt techniques for photovoltaic applications," *IEEE Transactions on Industrial Electronics*, vol. 60, no. 3, pp. 1156–1167, 2013.

[59] R. Leyva, C. Alonso, I. Queinnec, A. Cid-Pastor, D. Lagrange, and L. Martinez-Salamero, "Mppt of photovoltaic systems using extremum-seeking control," *IEEE Transactions on Aerospace and Electronic Systems*, vol. 42, no. 1, pp. 249–258, 2006.

[60] T. Dragicevic, J. M. Guerrero, J. C. Vasquez, and D. Skrlec, "Supervisory control of an adaptive-droop regulated dc microgrid with battery management capability," *IEEE Transactions on Power Electronics*, vol. 29, no. 2, pp. 695–706, 2014.

[61] W. Qi, J. Liu, X. Chen, and P. D. Christofides, "Supervisory predictive control of standalone wind/solar energy generation systems," *IEEE Transactions on Control Systems Technology*, vol. 19, no. 1, pp. 199–207, 2011.